Motion tracking for video-rate 4D imaging of ophthalmic surgical maneuvers

By

Eric Ming Tang

Dissertation

Submitted to the Faculty of the

Graduate School of Vanderbilt University

in partial fulfillment of the requirements

for the degree of

DOCTOR OF PHILOSOPHY

in

Biomedical Engineering

May 31, 2022

Nashville, Tennessee

Approved:

Yuankai K. Tao, Ph.D.

Brett C. Byram, Ph.D.

Michael I. Miga, Ph.D.

Ipek Oguz, Ph.D.

Shriji N. Patel, M.D.

ACKNOWLEDGMENTS

First and foremost, I would like to thank my parents and family members for their sacrifices and for providing me with the resources and opportunities to pursue my passion for research. I would also like to thank my undergraduate friends (DDMF) and all of the new friends that I have made here at Vanderbilt for always supporting me and providing advice as well as a necessary outlet for inevitable stress and frustration along the way. In addition, a special thank you to my present and former lab members, specifically Mohamed, Joe, Rachel, and Morgan for helping me along my journey. I am incredibly fortunate to have had the opportunity to work under Dr. Yuankai Tao these past 4 years, and I would like to thank Kenny for his continued mentorship and for providing me with training and guidance throughout my PhD. Additionally, I would like to thank my academic mentors and committee members, Dr. Michael Miga, Dr. Ipek Oguz, Dr. Brett Byram, and Dr. Shriji Patel. I would like to give a special thank you to Dr. Michael Miga for giving me the opportunity to be a part of the T32 training grant as well as Dr. Shriji Patel for enabling me to shadow ophthalmic surgical procedures and gain valuable insight into the current clinical challenges that has helped guide my research project. Finally, I would like to thank everyone at the Vanderbilt Biophotonics Center and VISE, specifically Michelle Bukowski, for their continuous feedback and support that has helped shape me as a student and researcher.

TABLE OF CONTENTS

Page

LIST OF TABLES

LIST OF FIGURES

CHAPTER 1

Ophthalmic Surgery

The following chapter contains content that is adapted from M. J. Ringel, E. M. Tang, and Y. K. Tao, "Advances in multimodal imaging in ophthalmology," Therapeutic Advances in Ophthalmology (2021) [1].

1.1 Ophthalmic disease management

Vision loss and blindness present significant social and economic burdens and are estimated to affect at least 2.2 billion people globally due to the prevalence of ophthalmic conditions such as presbyopia, age-related macular degeneration (AMD), diabetic retinopathy (DR), glaucoma, and cataracts [2], [3]. Direct health costs due to visual impairment were estimated to be 2.3 trillion USD globally in 2010 and are expected to rise due to an aging population, which has increased the proportion of people suffering from chronic eye diseases such as AMD, DR, and glaucoma [4]–[6]. Furthermore, it is estimated that at least 1 billion cases of visual impairment could have been prevented or are yet to be addressed. However, general population screening for diagnosis of early-stage ophthalmic diseases is often cost-ineffective, resulting in late-stage disease diagnoses when loss of visual acuity has already occurred. Management of ophthalmic diseases, thus, often requires surgical intervention to delay or prevent disease progression.

Ophthalmic microsurgery is the most frequently performed surgery in the United States, but requires extreme precision when manipulating submillimeter-thick, semi-transparent ocular tissues that results in a steep learning curve [7], [8]. Primary ophthalmic surgeries include 1) anterior segment procedures involving the cornea, iris, and lens, 2) posterior segment procedures involving the vitreous and retina, and 3) other intraocular procedures involving therapeutic delivery (Table 1.1) [9]. Despite the prevalence of ophthalmic surgery, limited visualization of fine ocular structures and

corresponding surgical maneuvers remains a critical barrier to improving clinical outcomes. Improvements in intraoperative ophthalmic surgical visualization are critical to successful operation by reducing risk of complications and providing enhanced feedback on instrument-tissue interactions that can be used for real-time guidance of surgical maneuvers.

Table 1.1. Incidence of primary ophthalmic procedures in the United States from 2012-2014. Adapted from [9] with permission from Elsevier.

Procedure	**Total Procedures, N**	**Inpatient Procedures, N (%)**	**Ambulatory Procedures, N (%)**
Corneal transplant	43,860	970 (0.7)	43,147 (1.1)
Glaucoma procedures	150,624	1,505 (1.1)	149,373 (3.9)
Lens and cataract	2,580,415	3,245 (2.3)	2,578,000 (66.5)
Repair of retinal tear, detachment	201,236	3,085 (2.2)	199,130 (5.1)
Other therapeutic procedures on eyelids, conjunctiva, cornea	339,132	86,325 (62.4)	318,615 (8.2)
Other intraocular therapeutic procedures	455,579	13,760 (9.9)	440,857 (11.4)

1.2 Anterior segment surgery

The anterior segment, or front of the eye, includes ocular structures such as the cornea, iris, lens, and ciliary body (Fig. 1.1). Common anterior segment surgeries include cataract surgery, glaucoma procedures, and corneal transplantation [9]:

Cataract surgeries are some of the most performed ophthalmic procedures worldwide and typically involve making a small corneal incision, followed by phacoemulsification and extraction, and finally replacement with an intraocular lens (IOL) [10]. Despite the speed and high success rate of cataract surgery, complications still occur in approximately 4% of cases due to several factors including dropped nuclei, postoperative endophthalmitis, and posterior capsular opacification [11], [12]. These complications can lead to more serious conditions including uveitis, increased intraocular pressure

resulting in iatrogenic glaucoma, and retinal detachment.

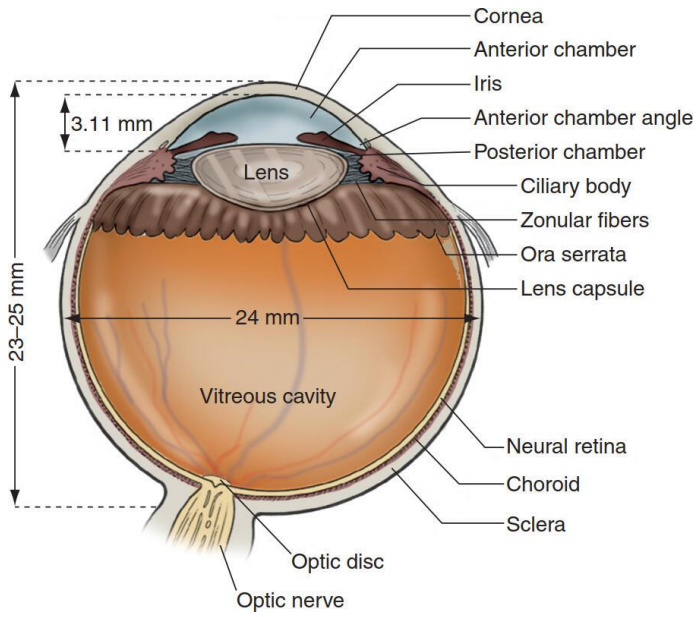

Figure 1.1: Anatomy of the eye. (American Academy of Ophthalmology).

Glaucoma procedures are performed to manage high intraocular pressures, which can ultimately result in optic nerve damage and vision loss. The most common glaucoma procedures are tube shunt surgeries or trabeculectomies, both of which function to open a pathway from the anterior chamber to the subconjunctiva for fluid to flow out of the eye, thus reducing intraocular pressure. Postoperative results from the Tube Versus Trabeculectomy (TVT) study comparing patient outcomes following tube shunt surgery or trabeculectomy showed high postoperative complication rates of over 34% independent of operation through a five-year follow-up [13]. Complications following glaucoma surgery include corneal edema, cystoid macular edema, suprachoroidal hemorrhage, retinal detachment, and persistent diplopia [14]–[16]. Furthermore, due to complications, reoperation occurred for 22% of patients who underwent tube shunt surgery and 18% of patients who underwent trabeculectomy in the TVT study.

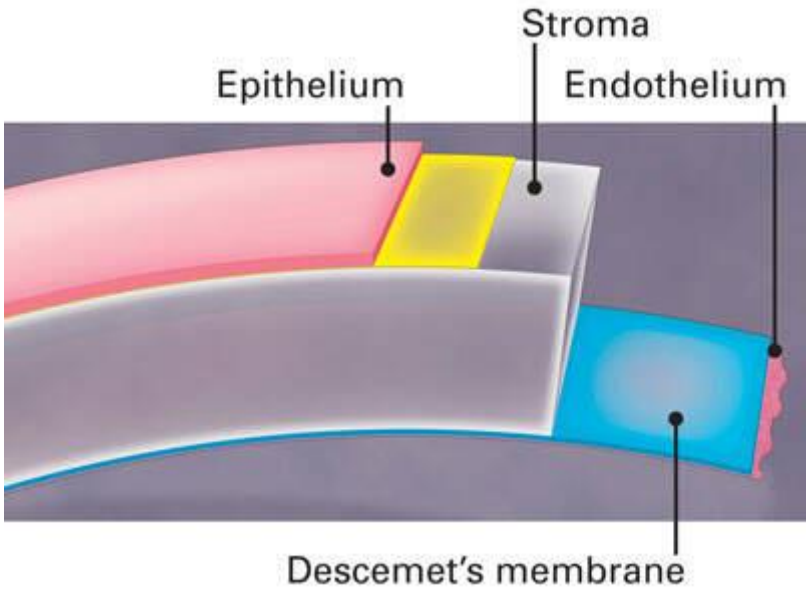

Figure 1.2: Cornea anatomy. (American Academy of Ophthalmology).

Keratoplasties, or operations involving the cornea, encompass a wide variety of surgical procedures including deep anterior lamellar keratoplasty (DALK), penetrating keratoplasty (PK), Descemet stripping automated endothelial keratoplasty (DSAEK), and Descemet membrane endothelial keratoplasty (DMEK). Donor corneal tissue is used for transplantation in each case but involves replacement of the full thickness of the cornea (PK) or partial thickness up to the Descemet's membrane and posterior endothelium (DALK) if the patient's posterior cornea is healthy (Fig. 1.2) [17]. Similarly, if the patient's anterior cornea is healthy, the Descemet's membrane and posterior endothelium can be removed and replaced along with donor corneal stroma (DSAEK) or without additional donor stroma (DMEK) [18]. These procedures are used to treat several conditions, including keratoconus, corneal scarring, and corneal dystrophies. However, complications associated with lamellar keratoplasties are well-documented and include donor graft rejection, graft detachment or failure, iatrogenic glaucoma, and microbial keratitis [19]–[22].

Postoperative complications and corresponding rates associated with anterior segment surgery are summarized in Table 1.2. Despite the prevalence of anterior segment operations in the United States

(Table 1.1), high rates of adverse postoperative outcomes often require reoperation and chronic management. Furthermore, the success rate following reoperation is significantly lower compared to initial operation, thus confounding these complicating factors. Improved intraoperative visualization of ophthalmic surgical procedures is essential to better understand the incidence of these intraoperative and postoperative complications for improved patient outcomes.

Table 1.2. Anterior segment procedure complications and associated rates.

Procedure	Complications	Complication Rate
Corneal transplant	Graft failure	3-20% (primary keratoplasty) [23], 12-54% (secondary) [23], 35-67% (tertiary) [23]
	Suture failure	10-12% [24]
	Descemet membrane perforation	0-50% [25]
	Iatrogenic glaucoma	9-31% (early postoperative) [26], [27] 14-47% (repeat keratoplasty) [28]
	Microbial keratitis	8% [20]
Glaucoma procedures	Persistent corneal edema	4.3-16% [13], [15]
	Cystoid macular edema	2.5-5% [13], [15]
	Suprachoroidal hemorrhage	0.5-8.3% [29], [30]
	Retinal detachment	1-5% [13], [15], [31]
	Persistent diplopia	6-12% [13], [15]
Lens and cataract	Iatrogenic glaucoma (due to retained lens fragments)	51.8-52% [32], [33]
	Corneal edema (due to retained lens fragments)	46-49.4% [32], [33]
	Uveitis (due to retained lens fragments)	56-67.1% [32], [33]
	Dropped nuclei	0.09-0.8% [11]
	Posterior capsular opacification	20.4% [34]
	Retinal detachment	4-8% [33]
	Endophthalmitis	0.35% [35]

1.3 Posterior segment surgery

Posterior segment surgery refers to operations involving ocular structures at the back of eye, including the vitreous humor, retina, optic nerve, and the choroid. Vitreoretinal surgeries represent the majority of posterior segment operations and include vitrectomy, membrane peeling, and laser photocoagulation for treatment of diseases such as DR and AMD as well as associated pathologies such as neovascularization, macular holes, and retinal detachments [36].

The most common vitreoretinal procedure is the pars plana vitrectomy (PPV), during which the gel-like vitreous humor is removed. PPV typically involves the insertion of three trocars through the sclera, allowing for surgical instruments, such as an infusion cannula, light pipe, and vitrector, to be inserted into the vitreous body [37]. PPV is often performed to relieve traction on the retina in the case of retinal detachments, which also aids in preventing future detachments. In addition, PPV is performed for cases of vitreous hemorrhage, intraocular foreign bodies, and for procedures requiring access to the subretinal space. Intraoperative complications associated with PPV are rare, but postoperative cataract formation has been described in 60-80% of patients, thus requiring follow-up or combined cataract surgery [38]–[40]. Less serious complications occur at a rate of 20% and include hypotony, retinal edema, retinal tears, and vitreous hemorrhage, while more serious complications, such as endophthalmitis and retinal detachment, occur at a rate of approximately 5% [41]–[43]. As a result, 30% of PPV cases require additional operation in order to resolve postoperative complications.

In addition to PPV, membrane peeling surgery is often required in response scar tissue formation due to aging and ophthalmic disease pathogenesis. Idiopathic epiretinal membrane (ERM) formation in healthy eyes can occur naturally due to aging and is caused by synchysis, or liquefaction of the vitreous humor [44]. Synchysis and syneresis, or contraction of the liquefied vitreous humor, results in traction between the posterior vitreous cortex and the inner/internal limiting membrane (ILM) of the retina, which leads to the proliferation of epiretinal cells and the formation of ERMs [45], [46]. Secondary ERM formation is less common and associated with several ocular conditions including inflammation following surgery, retinal detachment, macular hole, DR, AMD, and retinal vein

occlusion [47]. ERM formation and proliferation increases tension on the retina, resulting in distortion and progressive retinal thickening that can lead to irreversible loss of vision [48]. In these cases, surgical removal of the ERM/ILM is performed to restore vision and has been shown to significantly improve patient visual acuity [49]–[51]. However, postoperative complications associated with ERM/ILM peeling include cataract formation, retinal detachment, and cystoid macular edema in addition to confounding factors following PPV [52]–[54]. Additional challenges include ERM recurrence and subsequent reoperation, which is associated with worse success rates and worse visual outcomes [55].

Table 1.3. Posterior segment procedure complications and associated rates.

Procedure	Complications	Complication Rate
PPV	Cataract formation	60-80% [38]–[40]
	Hypotony	3.3-20% [41], [42], [56]
	Vitreous hemorrhage	1.5-4.8% [42], [43]
	Retinal edema	7.0-9.4% [43]
	Retinal tear	1.1-1.9% [41], [43]
	Retinal detachment	0.2-4.6% [41]–[43]
	Endophthalmitis	0.3-0.4% [43]
PPV + Membrane peeling	Cataract formation	52-76% [52]
	Cystoid macular edema	12-15.7% [52], [54]
	Retinal detachment	14% [52]

Common posterior segment complications and associated rates are summarized in Table 1.3. The most prevalent adverse event is cataract formation, which often necessitates combined PPV and phacoemulsification. Thus, these operations often confound multiple complicating factors due to both anterior and posterior segment procedure. In addition, reoperation for secondary PPV or secondary ERM removal is often necessary and is associated with worse outcomes. Similar to outcomes

described for anterior segment surgery (Section 1.2, Table 1.2), enhanced intraoperative visualization can potentially provide valuable insight into the incidence of postoperative complications. For example, volumetric and 4D visualization of instrument-tissue interactions can be used for real-time assessment of tissue deformation and tissue damage. Furthermore, these metrics can be directly associated with postoperative outcomes and patient visual acuity in longitudinal clinical studies to potentially provide enhanced intraoperative guidance of ophthalmic surgical maneuvers.

1.4 Drug delivery and therapy

Increasingly aging populations, especially in industrial countries, have contributed to the increased prevalence of chronic vitreoretinal disease, such as DR, AMD, and diabetic macular edema (DME) [57]. Treatment of chronic eye conditions of both the anterior and posterior segment has been significantly benefitted by the development of effective drug therapeutics, such as anti-vascular endothelial growth factor (VEGF) for the management of neovascular disease as well as topical eye drops for management of glaucoma and treatment of infectious diseases, such as endophthalmitis, keratitis, and conjunctivitis [58]. Topical drug delivery facilitates ophthalmic disease management without the need for direct surgical intervention and associated risks, but current noninvasive methods suffer from limited uptake by target ocular tissues. It is estimated that only 5-10% of topical drug dose is absorbed by the eye, with the remaining majority being absorbed into systemic circulation via blood vessels in the conjunctiva [59], [60]. Due to drug clearance by the anterior segment, topical drug administration is ineffective for and does not reach targets in the posterior segment of the eye [61]. Inefficient uptake is especially problematic for gene therapy and treatment of congenital ophthalmic diseases, including inherited retinal disorders such as retinitis pigmentosa (RP), Leber's congenital amaurosis (LCA), and Stargardt's disease [62]. As a result, more invasive drug delivery methods are typically observed in order to ensure effective drug administration and uptake by posterior segment tissues.

Alternative methods for drug delivery involve injection of drugs or implant placement directly into ocular tissue. Subconjunctival injections involve injection of fluid into the subconjunctival space,

which leads to the formation of a bleb and slow diffusion of drugs through the sclera, thereby bypassing uptake by conjunctival blood vessels. Despite low risk of complication due to direct visualization of the needle tip during the procedure, subconjunctival injection is impeded by diffusion of large macromolecules [63]. High scleral permeability ensures efficient drug delivery to the choroid, but the choroid and retinal pigment epithelium (RPE) present significant barriers to further diffusion into the retina due to low permeability of certain molecules by the blood-retinal barrier [64], [65].

Intravitreal injection is the most common technique for delivery of drugs directly to the posterior segment due to the direct uptake of drugs by the inner retina via the vitreoretinal interface, thereby bypassing the blood-retinal barrier. Intravitreal injection is typically used to administer anti-VEGF agents (e.g. bevacizumab, ranibizumab, aflibercept) or non-steroidal anti-inflammatory drugs (NSAIDs) to the posterior segment to deal with elevated VEGF levels and inflammation, respectively, that occur due to many ophthalmic diseases [66]. Due to the invasive nature of the injection, which is typically accomplished via a pars plana approach, a greater number of complications may occur compared to noninvasive or subconjunctival approaches. These complications include glaucoma, cataract formation, lens injury, endophthalmitis, and retinal tears or detachments [67]–[70]. However, due to the chronic nature of these ophthalmic diseases, multiple intravitreal injections are often performed, which can lead to higher risk and complication rates [71].

Another potential route for drug delivery is via subretinal injection where dosage volumes are administered directly between the photoreceptor layer and the RPE [72]. Subretinal delivery is the predominant approach for the treatment of inherited retinal disorders due to the fact that gene vectors come in direct contact with their two primary therapeutic targets, photoreceptor and RPE cells [73]. Targeting the neurosensory retina and RPE is more challenging using an intravitreal injection approach due to the transduction by epithelial cells in the ciliary body, neutralization in the vitreous via immune response, and the presence of the ILM, which acts as a barrier that separates the vitreous and outer retina [74]. Despite more efficient targeting, subretinal injections suffer from increased

rates of complication due to the inherent need to induce a retinal detachment via bleb formation [73]. Furthermore, transduction is typically limited to cells in a small vicinity near the retinal bleb and is therefore impractical for treating pan-retinal diseases [75].

CHAPTER 2

Intraoperative ophthalmic imaging

The following chapter contains content that is adapted from M. J. Ringel, E. M. Tang, and Y. K. Tao, "Advances in multimodal imaging in ophthalmology," Therapeutic Advances in Ophthalmology (2021).

2.1 Stereomicroscopy

Ophthalmic microsurgery is complex and requires the use of an operating microscope, which improves visualization of ocular microstructures and enables delicate manipulation of these features [76]. These surgical microscopes provide crucial illumination and magnification of both the anterior and posterior segments, which facilitates more precise surgical maneuvers [77]. In particular, ophthalmic microsurgery is conventionally performed under a white-light stereomicroscope, which provides an *en face* view of underlying ophthalmic structures. Stereomicroscopes differ from traditional 2D microscopes by providing stereopsis, which is the sense of depth perception that is achieved by binocular viewing of a scene [78]. As a result, stereomicroscopic views provide information that is similar to a human's binocular vision and thus improve interpretability. The development of modern stereomicroscopic systems dates back to the introduction of the Greenough stereomicroscope in 1892 [79]. These systems employ two identical tilted optical paths which relay light from an object into each eye for detection. More complex systems, such as common main objective (CMO) stereomicroscopes introduced in 1957, utilize a single shared objective that generates a flat focal plane compared to the Greenough configuration, which generates a slightly tilted image in each eyepiece. The use of a single objective lens also creates an infinity space between the objective and tube lens that enables more modularity for adjustable zoom range and magnification [80], [81].

Current generation stereomicroscopes for ophthalmic surgery typically employ CMO configurations, which benefit from improved versatility due to their modularity. In addition, systems such as the Leica Proveo 8 ophthalmic microscope take advantage of CMO infinity optics by modifying left and right eye channel components in a technique termed 'FusionOptics' [82]. The right eye channel is modified to include a larger numerical aperture binocular objective lens for high resolution imaging, while the left channel utilizes a lower numerical aperture lens to improve visual depth of focus at the cost of resolution. Viewing each channel simultaneously, the brain combines each image to generate a high-resolution, high depth-of-field image. Despite advancements in stereomicroscopic technology, microscopic systems suffer from changes in image appearance due to variable lighting conditions, nonuniform illumination, specular reflections, and noise [83], [84]. These variables reduce the quality of acquired digital images, which are often used for ophthalmic training, performance assessment, and motion analysis [85]. In addition, ophthalmic surgeon microscope views often provide higher resolution visualization compared to digitally captured images, thus limiting the utility of external monitors for surgical guidance [86]. As a result, there exists a need for improved visualization of complex ophthalmic tissue microstructures in order to provide real-time guidance of ophthalmic surgical maneuvers.

2.2 Optical coherence tomography

Optical coherence tomography (OCT) is a depth-resolved imaging modality based off of low coherence interferometry. Early time-domain OCT (TD-OCT) systems employed the use of a Michelson interferometer and translating reference mirror to extract depth information from tissue (Fig. 2.1). A broadband light source is split using a beam-splitter or power coupler between reference and sample arms that are path-length matched with each other. The reflected light from both paths is recombined by the coupler and detected, generating an interference fringe that can be used to extract sample reflectivity at a given depth. By moving the reference mirror, a depth-resolved sample reflectivity profile can be generated (A-scan). The incorporation of a scanning mirror in the sample path allows for multiple A-scans to be acquired at adjacent positions, thus generating a two-

dimensional (2D) image (B-scan). Finally, multiple B-scans can be acquired by raster scanning to generate three-dimensional (3D) volumes.

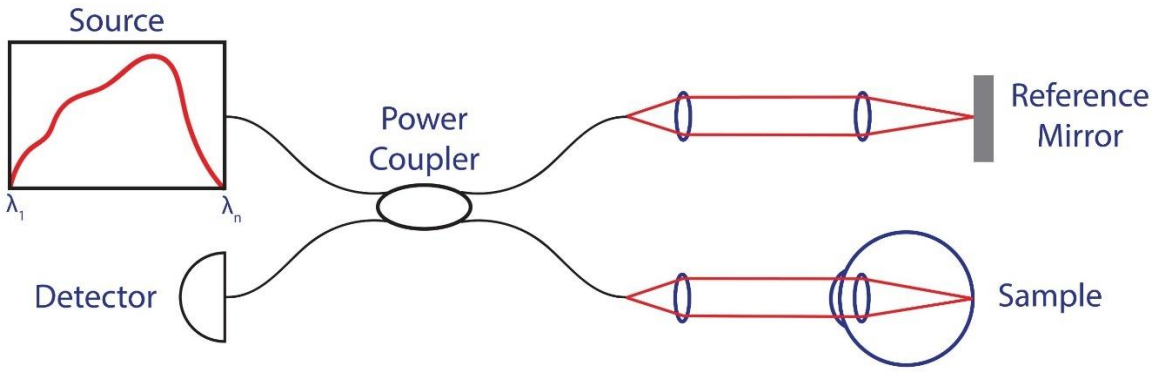

Figure 2.1. Simplified OCT imaging system setup utilizing a Michelson interferometer.

More recently, spectral-domain OCT (SD-OCT) and swept-source OCT (SS-OCT) systems have been developed. These systems have several advantages in terms of imaging speed as well as signal-to-noise ratio (SNR) compared to TD-OCT systems. SD-OCT and SS-OCT systems preclude the need to translate the reference mirror by acquiring the interference signal as a function of wavelength as opposed to time. In SD-OCT, this is accomplished by fixing the reference mirror position and spectrally dispersing the recombined light with a spectrometer and detecting it with a line detector such as a charge-coupled device (CCD). In SS-OCT, the laser is swept temporally through its optical range and thus only a single photodiode is necessary.

In addition, there exists a Fourier relationship between the source spectrum and axial point-spread-function (PSF). In particular, the coherence length of the system can be described as the full-width half-max of the axial PSF and therefore represents axial resolution. Since the coherence length is inversely related to the bandwidth of the source spectrum, broadband light sources are often used to achieve lower coherence lengths and higher axial resolution. Other metrics, such as signal-to-noise ratio (SNR), 6-dB falloff, and imaging range are also critical design criteria for clinical imaging and diagnostics (Table 2.1).

Table 2.2. Critical OCT design parameters for clinical ophthalmic imaging.

Signal-to-Noise Ratio (SNR)	$10 * \log\left(\frac{\rho P_s T}{e}\right)$	$\boldsymbol{\rho}$, detector sensitivity $\boldsymbol{P_s}$, sample power $\boldsymbol{T}$, A-scan rate $\boldsymbol{e}$, electron charge	(2.1)
Axial Resolution	$\frac{2\sqrt{\ln(2)}}{\Delta k} = \frac{2\ln(2)}{\pi}\frac{\lambda_0^2}{\Delta\lambda}$	$\boldsymbol{\lambda_0}$, source center wavelength $\boldsymbol{\Delta\lambda}$, source optical bandwidth $\boldsymbol{\Delta k}$, source bandwidth in wavenumber	(2.2)
6-dB Imaging Depth	$\frac{2\ln(2)}{\delta_r k} = \frac{\ln(2)}{\pi}\frac{\lambda_0^2}{\delta_r\lambda}$	$\boldsymbol{\delta_r}$, spectrometer resolution (SD-OCT) or instantaneous line-width (SS-OCT) in wavenumber and wavelength	(2.3)
Maximum Imaging Depth	$\frac{\pi}{2\delta_s k} = \frac{\lambda_0^2}{4\delta_s\lambda}$	$\boldsymbol{\delta_s}$, pixel size (SD-OCT) or sampling-clock frequency (SS-OCT) in wavenumber and wavelength	(2.4)

The introduction of OCT in 1991 has revolutionized the field of ophthalmology by providing depth-resolved 3D imaging of both the anterior and posterior segments of the eye [87]. Since its first demonstration, parallel advancements in laser sources, detectors, and data acquisition have greatly increased the speed, resolution, and the signal-to-noise ratio (SNR) of OCT imaging. Current high speed systems are capable of reaching megahertz (MHz) A-line rates for video-rate volumetric imaging [88]–[92] and ultrahigh resolution systems achieve axial and lateral resolutions between 1-10 μm [93]–[99]. The development of OCT has significantly improved the diagnosis and monitoring of ophthalmic diseases such as diabetic retinopathy (DR) [100]–[105], age-related macular degeneration (AMD) [106]–[110], and glaucoma [111]–[116] by enabling the high-resolution visualization of complex ophthalmic tissue microstructures and their changes over time.

Furthermore, the development of intraoperative OCT (iOCT) through the use of compact handheld OCT probes [117]–[127] and surgical microscope-integrated OCT (MI-OCT) [128]–[133] has addressed several limitations of clinical OCT by allowing for cross-sectional and volumetric imaging of supine patients during ophthalmic surgery (Figure 2.2). Depth-resolved imaging during surgery

enables visualization of instrument-tissue interactions for a wide variety of aforementioned anterior and posterior segment surgeries including tube-shunt/trabeculectomy, keratoplasties, ERM/ILM peels, and subretinal injections. In addition, the safety and efficacy of iOCT for ophthalmic surgery has been investigated in two landmark studies: (1) the Prospective Intraoperative and Perioperative Ophthalmic Imaging with Optical Coherence Tomography (PIONEER) study completed in 2017 evaluated the feasibility and safety of iOCT in 518 cases of ophthalmic surgery [134] and (2) the Determination of feasibility of Intraoperative Spectral domain microscope Combined/integrated OCT Visualization during En face Retinal and ophthalmic surgery (DISCOVER) study initiated in 2014 has assessed the viability of microscope-integrated iOCT imaging in a larger cohort of 820 cases and is currently ongoing [135].

2.2.1 Microscope-mounted OCT

The first demonstration of microscope-mounted OCT for intraoperative ophthalmic imaging utilized a system that integrated an operating microscope with a custom attachment for holding and stabilizing a handheld Leica Microsystems (formerly Bioptigen) probe [136]. Microscope-mounted OCT imaging enabled the generation of more repeatable images compared to previous handheld OCT studies [127]. In the study, iOCT utility was evaluated during macular hole repair surgery, which involved an ERM/ILM peel in 13 patients. Residual ERM and ILM could be easily visualized on iOCT without the use of exogenous contrast agents, such as indocyanine green (ICG) or triamcinolone acetonide dyes. In addition, conventional dye staining of the membranes enhanced their visualization on OCT, which facilitated identification of the edge of the membrane for peeling. iOCT also provided valuable quantitative information, such as macular hole height and thinnest width, that could potentially be correlated with surgical outcomes and used to help guide future patient management.

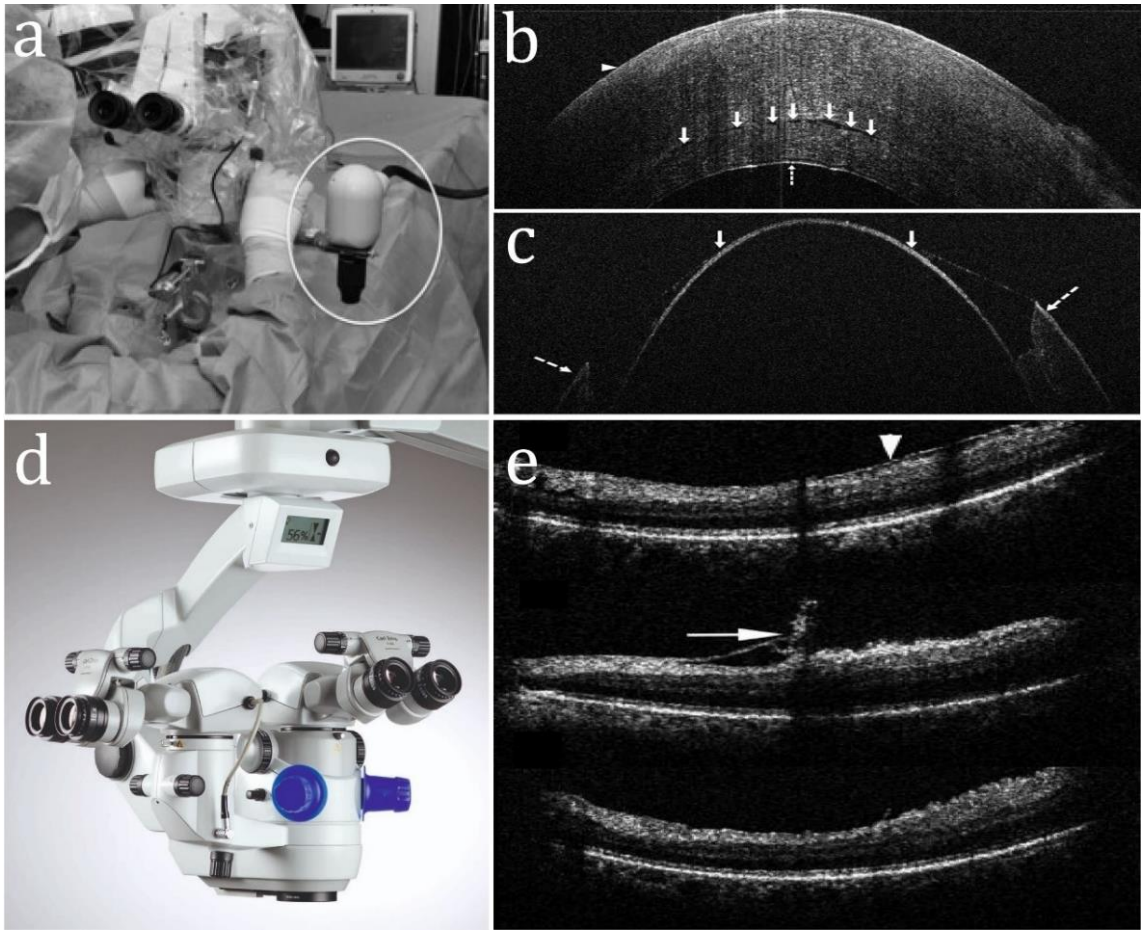

Figure 2.2: (a) Microscope-mounted handheld Bioptigen probe used for the PIONEER study [137]. (b) iOCT B-scan acquired following graft insertion during DSAEK surgery showing residual fluid at the graft/host interface and (c) iOCT B-scan acquired during DALK surgery showing trephination extent and the Descemet's membrane. Reprinted from [137] with permission from Elsevier. (d) Microscope-integrated ZEISS RESCAN 700 system used as one of three systems for the DISCOVER study [138]. (e) iOCT B-scans taken preoperatively (top), post initial ERM peel (middle), and post second ERM peel (bottom) showing complete membrane removal. Reprinted from [139] with permission from Elsevier.

The results of these initial clinical trials helped inform the possibility that a larger prospective study could provide valuable insight into the direct impact of iOCT imaging in surgical decision-making and long-term patient anatomical and functional outcomes [140]. Thus, the PIONEER clinical trial was initiated in 2011 to assess the utility of iOCT imaging in 275 anterior segment operations including DSAEK, DALK and cataract extraction, and 256 posterior segment procedures including vitrectomy and membrane-peeling [137]. The study utilized a microscope-mounted iOCT

probe (Figure 2.2(a)), which facilitated the visualization of crucial features, such as residual fluid in the cornea following DSAEK graft insertion and preservation of Descemet's membrane after stromal dissection during DALK (Figure 2.2(b),(c)) [141]. In particular, the presence of residual fluid at the graft/host corneal interface is associated with a higher incidence of postoperative interface opacity [142]. iOCT imaging allowed for monitoring of fluid removal during DSAEK, which enabled optimal graft apposition to the host corneal. iOCT feedback helped inform surgical decision-making despite surgeon belief that graft apposition was complete, which resulted in additional graft manipulation in 29% of DSAEK cases. iOCT also verified completion of surgical goals in 18% of DSAEK cases despite incomplete apposition assumed by the surgeon [137]. In vitrectomy cases for treatment of vitreomacular traction, iOCT enabled visualization of the vitreoretinal interface, which allowed for identification of traction release as well as subsequent macular hole formation. Overall, iOCT helped guide surgical decision-making in 48% of lamellar keratoplasty cases and 43% of membrane peeling cases, and no adverse events were attributed to the use of iOCT [137].

Despite the advantages of microscope-mounted OCT imaging during surgery, the use of a mounted handheld probe necessitated switching between the surgical microscope and the probe during the operation, leading to repeated pauses that increased operating time by up to 26.7 minutes (mean: 4.9 minutes) [137]. Pause time included image acquisition as well as alignment of the handheld probe to the patient, which can be particularly challenging when imaging the posterior segment and required a trained research technician to facilitate efficient imaging during the operation. Furthermore, the microscope-mounted platform precluded real-time visualization of surgical maneuvers, which could potentially be used to directly monitor instrument-tissue interactions and therefore tissue deformation or damage.

2.2.2 Microscope-integrated OCT

Technological advancements made in parallel to the conduction of the PIONEER trial enabled the development of MI-OCT systems, which provide simultaneous visualization of the surgical microscope field and OCT cross-sections. The first MI-OCT system was described in 2010 and

incorporated OCT optomechanical imaging components into a compact enclosure that could be suspended directly from a surgical microscope while also supporting an Oculus Binocular Indirect Ophthalmomicroscope (BIOM) for imaging of the posterior segment during vitreoretinal surgery [128]. Further developments enabled imaging of both the anterior and posterior segment on the same platform using an electrically tunable focus, which allowed for real-time compensation of the OCT focal plane with respect to that of the surgical microscope [131]. Heads-up display (HUD) integration of the surgical microscope oculars was also used to dynamically display OCT images across the entire ocular field-of-view (FOV), overlaid on the surgical field, or at the periphery of the field in accordance with user preference. MI-OCT addresses several limitations of previous microscope-mounted configurations by eliminating the need for repeated pauses during operation and allowing for real-time visualization of surgical maneuvers and instrument-tissue interactions. Alignment and stability of OCT imaging to the patient is also facilitated by direct integration with the surgical microscope FOV and automated focus control using a foot pedal.

Preclinical studies performed to evaluate the utility of MI-OCT demonstrated similar imaging performance to previous microscope-mounted handheld OCT systems and real-time visualization of both anterior and vitreoretinal surgical maneuvers [129], [130], [143]. Early studies have also shown that MI-OCT informs surgical decision-making by providing feedback that guided additional membrane peeling for removal of residual ERM/ILM [144]. MI-OCT enabled membrane peeling without the use of dyes in 40% of patients, and OCT images corresponded well with retinal dyes in 94.3% of patients for verifying complete membrane removal [145]. However, these initial studies suffered from relatively small sample sizes, which limited interpretability of the potential impact of MI-OCT in facilitating ophthalmic surgery.

As a result, the DISCOVER trial was initiated in 2014 to assess the feasibility of MI-OCT imaging in a larger cohort of patients (873 eyes) for both anterior segment and posterior segment surgery [139]. MI-OCT imaging was performed at multiple centers using three different systems: Zeiss RESCAN 700, Leica EnFocus, and a prototype developed at the Cole Eye Institute (Figure 2.2(d)).

The anterior segment arm of the study included 244 operations involving DSAEK, DALK, DMEK, PK, cataract extraction, and tube-shunt surgeries. MI-OCT was reported by surgeons to provide valuable feedback in 88.5% of anterior segment cases and was used to evaluate the extent of DSAEK/DMEK graft apposition as well as the presence of fluid at the graft interface. Furthermore, graft position feedback and persistent interface fluid on MI-OCT informed changes in surgical management in 43.4% of these cases. The posterior segment arm of the study included 593 operations involving PPV and membrane peeling. MI-OCT informed surgeons of residual membranes in 19.8% of patients undergoing ERM/ILM peeling and helped to verify completion of surgical goals in 40% of cases despite surgeon belief that there was residual membrane (Figure 2.2(e)). Surgeons reported that MI-OCT provided valuable feedback in 59.4% of posterior segment cases with changes in surgical management due to MI-OCT feedback occurring in 29.2% of cases.

2.3 Clinical challenges

Despite the reported benefits of MI-OCT for surgical guidance, several major limitations hinder the broad adoption of the technology. Although numerous clinical trials have demonstrated the feasibility and utility of iOCT for surgical guidance, more studies are needed to understand the impact of iOCT guidance on patient outcomes in terms of complication rate, reoperation rate, visual acuity, and quality of life. Furthermore, these studies have shown that there are still fundamental limitations of MI-OCT technology that impede its overall utility. A major finding of the DISCOVER study was surgeon preference of static OCT images for posterior segment operations due to several limitations of real-time MI-OCT feedback, including instrument shadowing and lack of instrument-tracking. In addition, the slow scan speeds of commercial MI-OCT systems, such as the Zeiss RESCAN 700 and Leica EnFocus, limit visualization to cross-sectional images and static FOVs that require manual alignment to the surgical region-of-interest (ROI). Broad adoption of iOCT technology requires a combination of rapid volumetric imaging and automated instrument-tracking for full 4D visualization of instrument-tissue interactions during surgery.

2.3.1 Video-rate 4D visualization

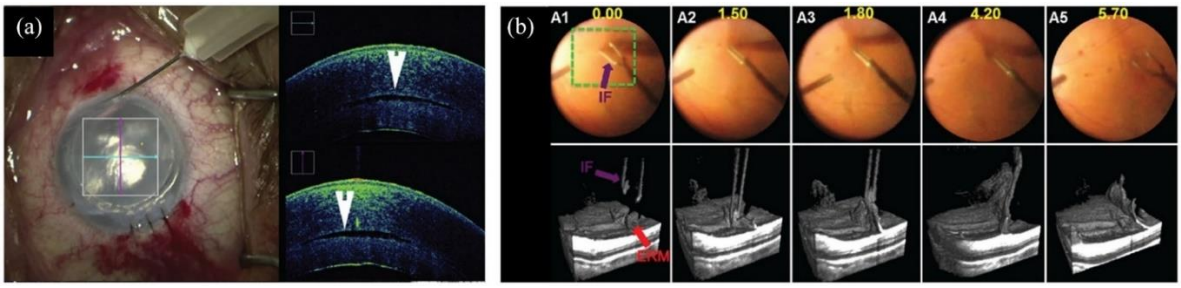

Figure 2.3: iOCT visualization during (a) anterior and (b) posterior segment surgery [139]. (a) iOCT showing graft placement during corneal transplant showing a persistent fluid interface (arrowhead). (b) 4D iOCT imaging of forces peeling epiretinal membrane [133].

Current-generation commercial MI-OCT systems are limited by static cross-sectional imaging of ROIs (Figure 2.3(a)), which inhibits visualization of bulk interactions between the surgical instrument and underlying tissue. In particular, the OCT systems used in the PIONEER and DISCOVER trials operate at line rates less than 40 kHz, which is an order of magnitude slower than current research-grade OCT systems [146]. As a result, it is difficult to perform real-time volumetric imaging that can potentially be used to improve visualization of instrument-tissue interactions during complex surgical maneuvers [131], [147]. The recent development of rapid swept-source lasers has facilitated the development of 4D OCT imaging systems. The first demonstration of 4D MI-OCT was able to achieve volumetric imaging rates up to 10 Hz using a 400 kHz source (Figure 2.3(b)) [133]. Beyond traditional swept-source lasers, Fourier Domain Mode Locked (FDML) lasers have also been developed for ultrafast OCT imaging at multi-MHz line rates [148], [149]. These systems have been shown to be able to achieve line rates of up to 20.8 MHz using a base 5.2 MHz FDML source and parallel scanning of four spots. Recent implementations of multi-MHz OCT have demonstrated video-rate volumetric imaging at over 20 Hz in the human finger as well as the posterior segment of the eye [150], [151].

Despite advances in laser speed, rapid volumetric imaging reduces detector integration time per beam position on the sample, which inherently degrades image SNR and requires increased sampling

density or decreased FOVs. As a result, optimal volumetric imaging rates are between 2 to 3.33 Hz for sufficient sampling of 4D MI-OCT volumes [133]. Furthermore, down-sampling via volumetric averaging is often necessary to achieve clinically relevant SNR levels above 95 dB when operating in the multi-MHz line rate regime [90]. In order to address these limitations, novel scan patterns have been proposed for improved volumetric OCT imaging. These scan patterns include Lissajous scanning [152], constant angular velocity spiral scanning [153], and constant linear velocity spiral scanning (CLV-SC) [154]. CLV-SC enables 4D OCT imaging at 10 Hz volume rate with isotropic transverse and axial resolution while simultaneously eliminating dead time between successive scans due to scanner return lines. However, these modified scan patterns necessitate remapping of acquired data back into Cartesian coordinates, which requires additional post-processing and computational overhead for visualization. Thus, there exists a fundamental trade-off between 4D imaging speed, sampling density, and FOV, which precludes real-time visualization of surgical maneuvers with high resolution.

2.3.2 Motion compensation

One major limitation of commercial OCT imaging is the presence of motion artifacts, which degrade image quality, distort anatomical features, and prevent quantitative analyses from being performed [155]. These systems are relatively slow, which makes them more susceptible to multiple sources of motion: patient motion including fixational eye motion (ocular tremor, drift, and microsaccades) [156] as well as bulk motion due to patient movement, breathing, and operator motion [157]. Despite the use of microscope-mounted and MI-OCT systems for increased stability, iOCT imaging is additionally confounded by complex surgical maneuvers, which often require patient adjustment to target ROIs.

Several hardware and computational methods have been proposed for motion tracking and compensation of OCT volumes. Hardware solutions include the use of research-grade systems employing rapid swept-source lasers. Multi-MHz sources enable real-time volumetric imaging, which significantly reduces the effects of motion artifacts due to faster data acquisition with respect

to the temporal dynamics of typical sources of motion [158]. However, these systems suffer from inherently low image SNR, which necessitates increasing sampling density or decreasing FOV. Multi-volumetric averaging of multi-MHz OCT volumes is an effective computational method to improve image SNR and simultaneously reduce speckle noise but is ultimately highly susceptible to intervolume motion and achieves effective line rates similar to current commercial systems. Alternative motion compensation methods include the use of novel scan patterns, such as Lissajous scanning and CLV-SC. These software-based methods can facilitate motion tracking and compensation for improved image quality and reduction of motion-artifacts [159]–[161]. However, the increased complexity of these scan patterns compared to conventional raster scanning prevents the real-time visualization of tissue that is crucial for intraoperative guidance. Another common method employing modified scan patterns is orthogonal volume acquisition which necessarily increases acquisition time and is therefore also infeasible for video-rate intraoperative visualization [162].

Clinical OCT systems, such as the Heidelberg Spectralis, Optos Silverstone, and Zeiss PLEX Elite, often implement external eye-tracking technology for effective motion correction despite slow scan speeds. The development of scanning laser ophthalmoscopy (SLO) in 1980 has enabled high-resolution *en face* ophthalmic imaging and has been leveraged by these systems to provide complementary *en face* and depth-resolved via combined OCT-SLO. Furthermore, the efficacy of tracking SLO for aiming and motion compensation of OCT volumes has been extensively demonstrated [163]–[166]. However, these early systems typically employed separate scanning systems for SLO and OCT and thus lack spatial co-registration that prevents motion correction on a frame-by-frame basis. Many current generation combined OCT-SLO systems use shared optics and scanners to relay light into the eye to reduce overall system complexity and provide pixel-level co-registration between corresponding OCT and SLO images [167]–[170]. SLO motion tracking precision is related to both spatial and temporal resolution, and development of line-scanning SLO (LSLO) has overcome frame-rate limitations of conventional point-scanning SLO systems at the

expense of full confocality, allowing imaging of fast dynamics up to several hundred frames per second [171]–[173]. In addition, novel extended source LSLO illumination and detection schemes, such as those using spectral encoding, have replaced complex free-space relays from source to detector with fiber optics, and handheld prototypes using these technologies have recently been used for motion corrected *in vivo* ophthalmic OCT and OCT angiography (OCTA) [122], [174], [175].

2.3.3 Automated instrument-tracking

The broad utility of MI-OCT is severely limited by static cross-sectional imaging and lack of robust instrument-tracking methods that necessitates manual alignment of OCT FOVs to surgical ROIs [139], [143], [145]. Although motion tracking methods have been widely implemented in clinical OCT systems, intraoperative motion tracking is confounded by variations in the surgical environment and instrument deformation inside the eye. These factors prevent the use of traditional tracking methods, which rely on instrument color, geometry, or edge detection extracted from surgical microscope or endoscope feeds [83], [84]. In particular, surgical microscope images tend to suffer from nonuniform illumination, specular reflections, and background noise. Current techniques for intraoperative motion tracking include manual alignment via custom software to offset OCT scan positions, which requires an additional trained technician to be to be able to accurately follow instrument positions intraoperatively [176]. Several tracking methods have also been proposed to track instrument position from segmented OCT B-scans and volumes but ultimately assume continuous localization of the instrument within the OCT FOV [177]–[180]. As a result, these methods are impractical for intraoperative 4D visualization where OCT FOVs are limited to small ROIs in order to maintain sufficient image sampling. Stereo-vision-based tracking methods have also been explored but assume a rigid relationship between the surgical instrument and physical space and do not account for changes in instrument shape and orientation as well as ocular distortions [181]–[184]. Furthermore, these methods are limited by the need for fiducial markers that limit application to the anterior segment. More recently, advancements in deep-learning-based tracking have been demonstrated, enabling tracking with high speed and accuracy [185]–[187]. These methods overcome limitations of current

instrument-tracking methods for ophthalmic surgery and ultimately enable rapid and robust detection of surgical instruments despite image variability.

CHAPTER 3

Optimization of a portable multimodal ophthalmic imaging system for real-time motion tracking

3.1 Introduction

Intraoperative tracking of surgical instruments for retinal microsurgery has been previously explored, but typically involves the use of complex algorithms [188], [189]. These methods increase post-processing computational burden and preclude real-time video-rate tracking of surgical maneuvers. In addition, the accuracy of these models is highly dependent on the quality of the surgical video feed, which is integrated with the surgical microscope and used for *en face* tracking of the instrument tip. These models oversimplify the tracking problem based on instrument color or geometry and typically perform more poorly in complex *in vivo* applications due to nonuniform illumination across the surgical field as well as aberrations caused by the eye and microscope lenses [189], [190]. Other methods for rapid instrument-tracking include the use of stereo-vision for accurate real-time tracking, but require modification of the surgical instrument through the use of LEDs and fiducial markers, which may lead ergonomic challenges as well as potential safety concerns due to lack of sterilization [184], [191], [192]. Furthermore, instrument-tracking for MI-OCT presents more challenges due to the lack of co-registration between the surgical FOV and OCT FOV. Due to the orthogonality between the microscope view and OCT priority acquisition dimension, surgeons must estimate the location of features in the surgical field with respect to their location in corresponding OCT images, which can impede operation.

An alternative solution to tracking via *en face* images provided by the surgical microscope feed is to use SLO-based tracking. Tracking SLO has several advantages in that the technology can be integrated with OCT imaging for co-registered *en face* imaging. Due to the fact that SLO also provides *en face* 2D images, it can also be used to co-register to the surgical microscope FOV while also ensuring co-registration between OCT and the surgical microscope. In addition, the frame rate

of tracking SLO is independent of the surgical microscope feed rate and can potentially be increased for higher speed tracking, which benefits video-rate applications. Although early SLO systems were confocal, point-scanning systems, recent developments have led to the introduction of line-scanning SLO systems with frame rates on the order of 100 Hz [170], [171]. For real-time tracking, we take advantage of a previously developed spectrally encoded coherence tomography and reflectometry (SECTR) system that combines *en face* spectrally encoded reflectometry (SER) line-scan imaging and cross-sectional OCT imaging [122], [173], [193]. Here, we construct a portable SECTR system for clinical imaging and validate its utility for *in vivo* motion tracking.

3.2 Spectrally encoded coherence tomography and reflectometry

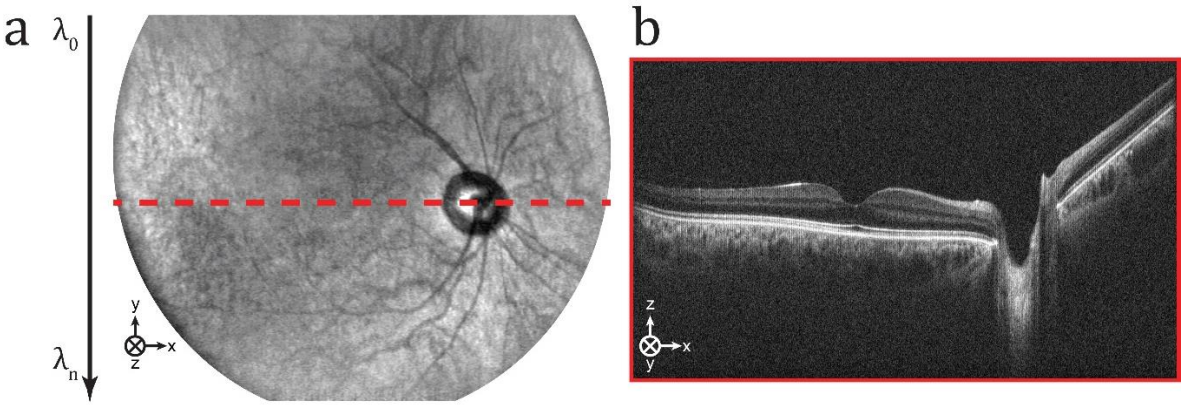

Figure 3.1. SECTR imaging is used to simultaneously acquire orthogonal (a) *en face* SER and (b) cross-sectional OCT images. SER laser power is spectrally dispersed as a function of wavelength (λ) along the OCT slow-axis (Y) for line scan imaging. Adapted with permission from [173].

In order to address the aforementioned limitations of slow commercial iOCT systems and lack of motion or instrument tracking, our group has developed a multimodal ophthalmic imaging system called SECTR that integrates *en face* SER and cross-sectional OCT imaging (Fig. 3.1) [173]. The system uses a high-speed 400 kHz swept-source laser that is split between SER and OCT using a custom-built engine. SER power is spectrally dispersed using a diffraction grating for *en face* line scan imaging and tracking at high frame rates. The OCT beam is combined colinearly with SER using shared optics and electronics. A shared fast-axis (X) galvanometer is then used to sweep SER line

and OCT beam simultaneously. High-speed SECTR imaging enables rapid volumetric over an order of magnitude faster than current commercial iOCT systems. Furthermore, orthogonality between tracking SER and cross-sectional OCT also facilitates real-time motion tracking.

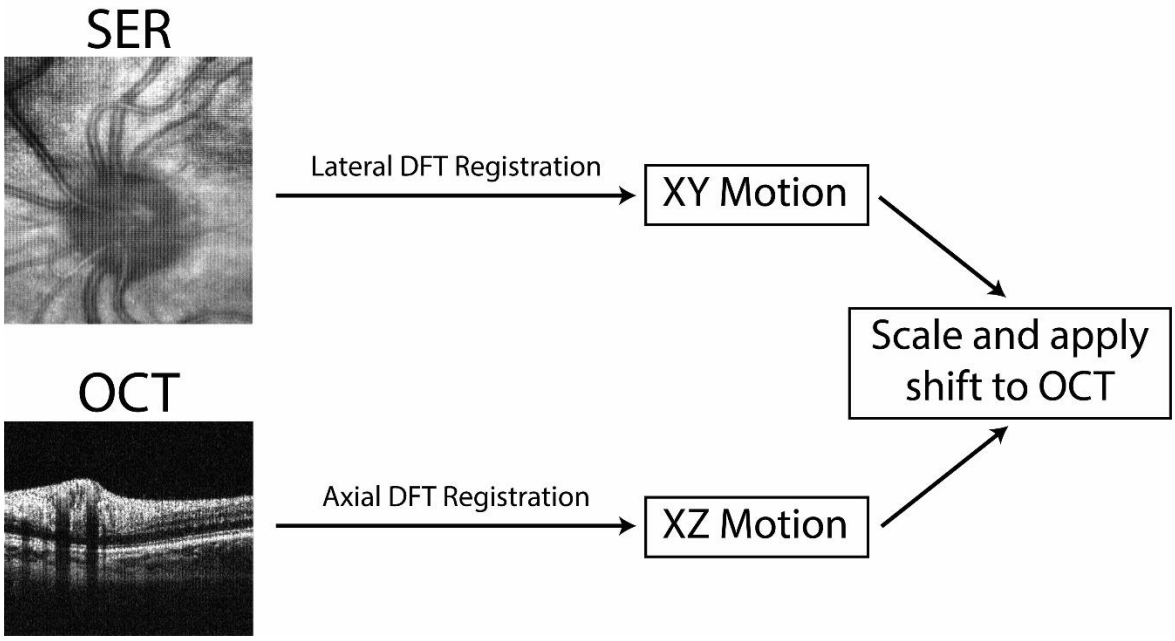

Figure 3.2. SECTR-based motion-tracking pipeline. Three-dimensional motion is extracted from simultaneously-acquired SER (XY) and OCT (XZ) images. The motion parameters are then scaled to account for pixel scale differences between each modality. Finally, lateral and axial motion parameters are applied to OCT B-scan for motion-corrected volumetric OCT.

Inherent spatio-temporal co-registration between these two imaging modalities enables 3D motion tracking and compensation of OCT volumes (Fig. 3.2). Discrete Fourier transform (DFT) registration [194] is used to extract XY motion from SER images and XZ motion from OCT images. These shifts are then scaled and applied to corresponding OCT cross-sections for motion correction on a frame-by-frame basis. Additionally, SER images enable rapid tracking of *en face* features, such as optic nerve head or instrument position, which can be directly correlated with OCT scan positions and OCT volume FOVs for real-time feature tracking. These tracking methods can also be leveraged for intraoperative tracking of macular holes or other pathological features or for automated instrument-tracking for 4D visualization of ophthalmic surgical maneuvers.

3.3 Portable SECTR design

We have previously developed a SECTR system that combines SER and OCT imaging [173]. In particular, the system is comprised of an engine and imaging relay. The engine contains optomechanical components to split laser power between SER and OCT imaging as well as detectors for each modality. The engine utilizes a 200 kHz swept-source laser (Axsun) centered at 1060 nm for optimal retinal imaging. In order to improve the speed of the system, the laser is optically buffered to double its duty cycle, resulting in a 400 kHz sweep rate. Due to the buffer, an external laser trigger and external k-clock are used for acquisition synchronization and linear sampling as a function of wavenumber. The engine interfaces with a high-speed digitizer (ATS-9373, AlazarTech) that is used to simultaneously sample SER and OCT channels at 2 GB/s, allowing for real-time visualization of both imaging modalities. For ophthalmic imaging, SER and OCT beams are relayed to the eye with an optical imaging relay either using a benchtop configuration or the use of a handheld imaging probe [122]. Colinear combination of SER and OCT beams is achieved using shared optics and a shared fast-axis scanning mirror, ensuring spatiotemporal co-registration between the two modalities. We believe a portable SECTR system will enable rapid motion tracking that can benefit intraoperative ophthalmic imaging and real-time visualization of surgical maneuvers.

3.3.1 Portable SECTR model and construction

Despite the demonstrated utility of the SECTR system, there are several limitations that prevent the translation of SECTR into the clinic or operating room. In particular, the SECTR engine is currently limited to the benchtop, which facilitates preliminary imaging and quick changes in system design but also precludes movement of the technology outside of the lab space for clinical use. In order to facilitate the translation of SECTR imaging, a portable system was designed and constructed. Individual components (Fig. 3.3(a)) were first modelled in SolidWorks before assembly and construction. The overall design was optimized to fit in a compact optical enclosure that could fit onto a mobile cart (Fig. 3.3(b)).

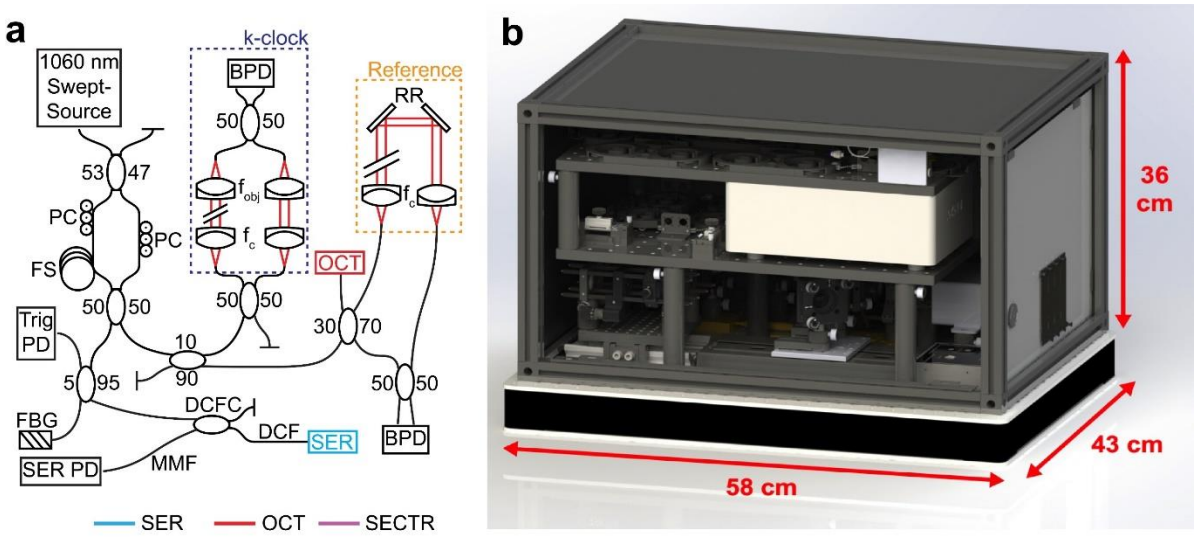

Figure 3.3. (a) SECTR engine [122] and (b) SolidWorks model and dimensions of the compact enclosure containing all of the components shown in (a).

3.3.2 Portable SECTR optimization

Another limitation of the benchtop SECTR engine was the inherent insertion loss between the power coupler connections. In order to address this problem, power coupler connectors were removed and the optical fibers were fusion-spliced together. A total of 7 connections were fusion spliced, resulting in a 64% increase in power at the pupil for OCT (1.4 mW vs. 2.3 mW) and a 27% increase in power at the pupil for SER imaging. In addition, the power of OCT and SER imaging after fusion-splicing was designed to conform to the American National Standards Institute (ANSI) safety limits for infrared exposure on the eye. By using more power at the pupil for imaging, it is possible to significantly increase imaging SNR. The theoretical formula for SNR in SD-OCT and SS-OCT is given by the expression (Eqn. 3.1):

Signal-to-Noise Ratio (SNR)	$10 * \log\left(\frac{\rho P_s T}{e}\right)$	$\boldsymbol{\rho}$, detector sensitivity $\boldsymbol{P_s}$, sample power $\boldsymbol{T}$, A-scan rate $\boldsymbol{e}$, electron charge	(3.1)

Thus, it can be expected that the OCT imaging SNR increases by 2.16 dB, which is crucial for improved clinical imaging, accurate diagnostics, and high-speed intraoperative imaging applications that inherently sacrifice SNR. An increase in SER power also benefits motion estimation and tracking due to increased *en face* image SNR and contrast.

3.4 *In vivo* motion tracking

Ophthalmic imaging is often confounded by motion artifacts that arise due to patient saccadic eye motion or bulk motion during image acquisition. Handheld ophthalmic imaging often confounds this problem due to the fact that operator motion occurs simultaneously to patient motion. This issue is especially evident in handheld OCTA, where the dense sampling requirements result in longer acquisitions that are more susceptible to motion artifacts [123]. In order to show the benefits of SER-based motion tracking, several OCTA volumes were acquired in a healthy adult volunteer. Small amounts of motion can severely degrade OCTA quality and prevent quantitative analyses from being performed [195]. Thus, OCTA image quality following motion registration and compensation enables objective evaluation of the utility of SER-based retinal tracking that can potentially be used for intraoperative instrument tracking. In order to demonstrate the utility of the portable SECTR system for retinal imaging and tracking, the engine was interfaced with a handheld ophthalmic imaging probe for *in vivo* imaging (Fig. 3.4). Ophthalmic imaging was performed with the mobile system under an Institutional Review Board (IRB) approved protocol in a mock surgical operating room.

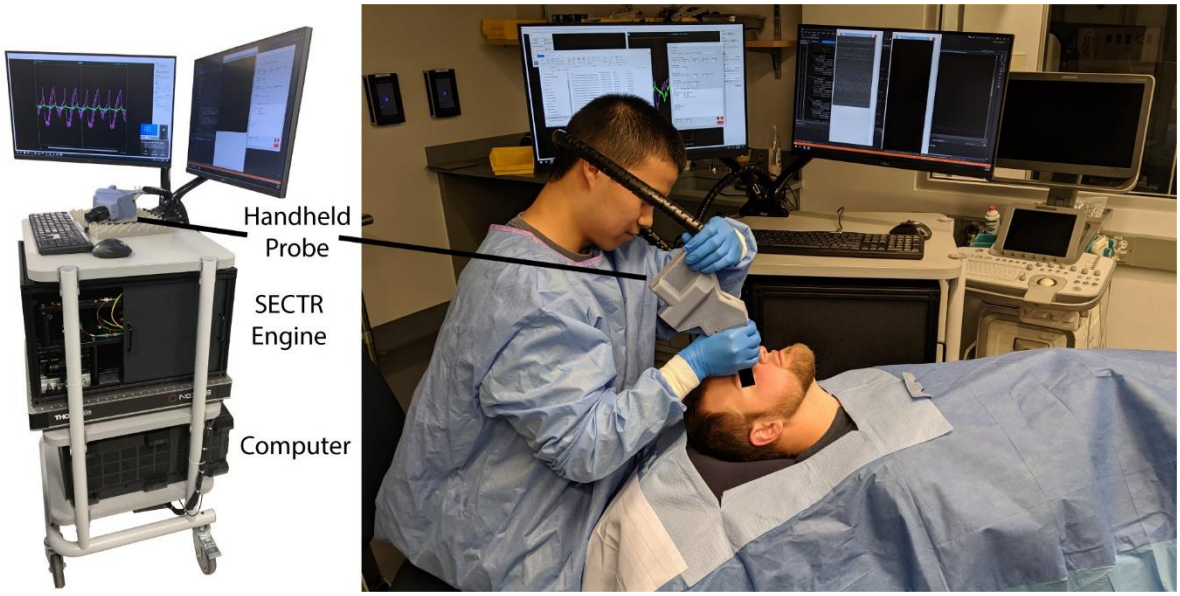

Figure 3.4. Portable SECTR system for *in vivo* handheld imaging of a supine patient.

3.4.1 SER-based motion tracking and registration

For demonstration, OCTA volumes were acquired at the fovea using 2560 pixels per line, 500 lines per frame, and 400 frames per volume with 4 repeated frames for a total volume acquisition time of 3.2 seconds (Fig. 3.5). Images before motion registration show significant degradation due to bulk motion, which appears as bright streaks across the image. In addition, motion results in vessel discontinuities which affect quantitative measurements and reduce anatomical accuracy (Fig. 3.5(a)). In order to perform motion compensation, DFT registration was used to estimate lateral shifts from SER images (X, Y) and axial shifts from OCT images (Z) on a frame-by-frame basis [194]. Following motion compensation and post-processing via self-fusion [196], image quality and anatomical accuracy significantly improve (Fig. 3.5(b)). The images show lateral frame shifts as well as gaps between frames, which are due to out-of-plane motion measured on SER and would not be measurable solely with OCT.

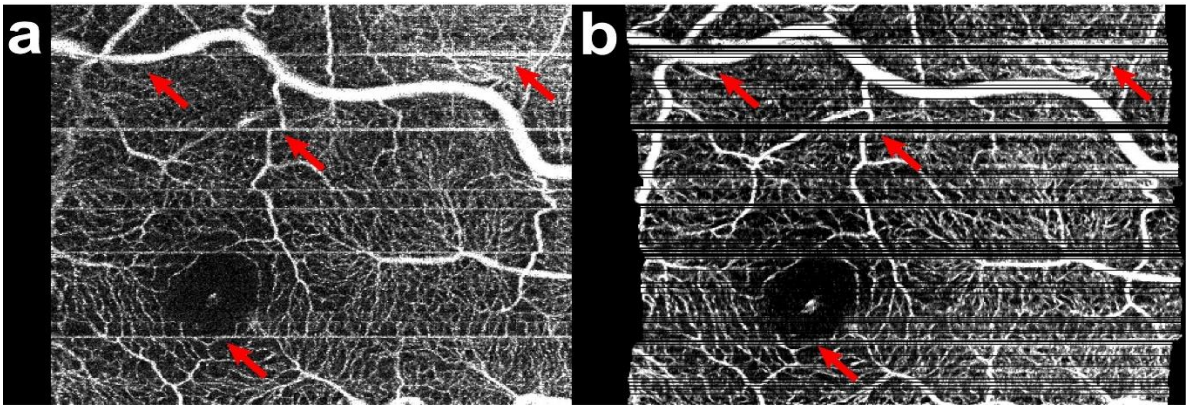

Figure 3.5. SER-based motion tracking and compensation of OCTA volumes. (a) Raw OCTA *en face* projection showing significant motion artifacts, including noise regions and vessel discontinuities (red arrows). (b) Motion-corrected and post-processed OCTA projection showing improved image quality and anatomical accuracy.

Regions of the eye that are typically affected by ophthalmic disease include the fovea, optic nerve head, and the periphery of the retina where diseases tend to originate. In order to show the viability of SER-based motion tracking, multiple OCTA volumes were acquired at each position and motion compensation was performed (Fig. 3.6(b)-(d)). In addition, multi-volumetric mosaicking can be performed via deformable registration on the volumes acquired at each position [197]. Mosaicking and self-fusion can be used to improve image quality as well as to fill in missing information between acquisitions, thus benefitting clinical diagnostics by maintaining more accurate anatomical features (Fig. 3.6(e)-(g)).

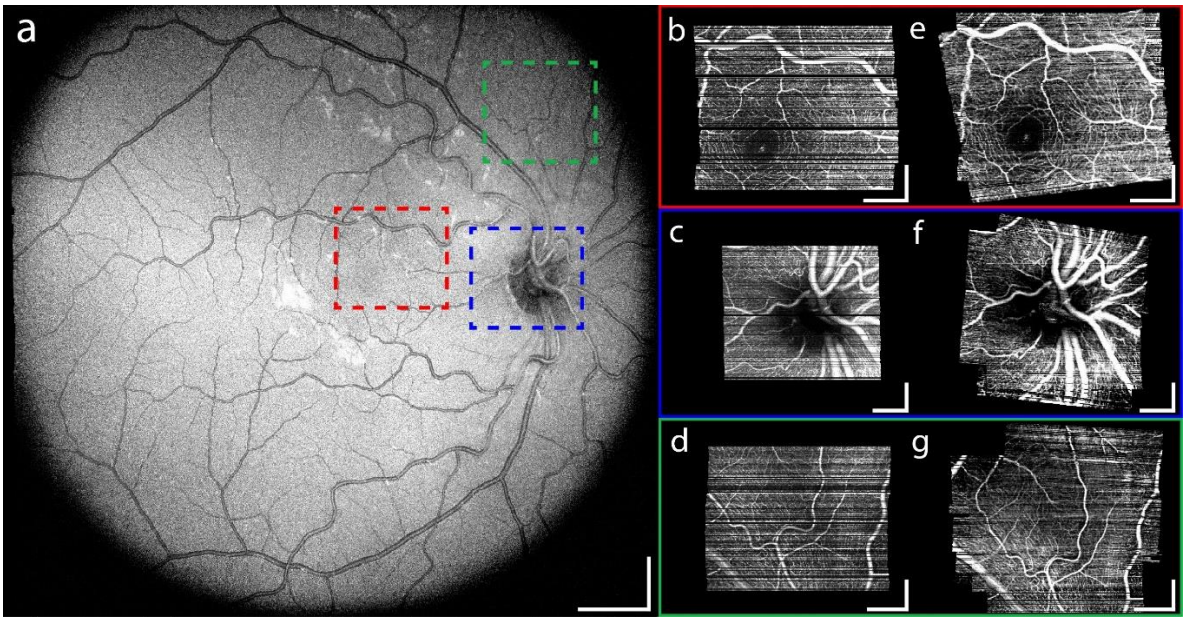

Figure 3.6. In vivo retinal imaging. (a) Widefield OCT with highlighted regions corresponding to the fovea (red), optic nerve head (blue), and peripheral retina (green). (b), (c), (d) Motion-corrected single OCTA projections at each position. (e), (f), (g) Three-volume OCTA mosaics showing improved vessel contrast. Scale bar: 250 μm

3.4.2 Variable-velocity scanning

Although it has been shown that SER can be used for motion tracking and compensation of OCT volumes, there are several limitations that degrade registration performance. SER is a line scan imaging modality and therefore lacks the confocality of conventional reflectance imaging modalities that is typically used to reject specular reflections and out-of-focus light. Thus, SER images are highly susceptible to image artifacts such as tear-film reflections from the cornea and specular reflections from the OCT beam especially when imaging the fovea, which is the region of on-axis central vision. A potential solution to this problem is to extend the FOV out to the optic nerve head, a region that is much less susceptible to these reflections. However, extending the FOV necessarily increases overall volume acquisition time, which can potentially limit video-rate volumetric imaging applications (Fig. 3.7(a)). A more viable solution is to use variable-velocity imaging to densely sample a ROI (e.g. the fovea or an instrument tip) and sparsely sample the periphery of the FOV (Fig. 3.7(b)). The sparse region of the FOV can then be resampled to extract the same SER fiducials as in the case of linear sampling with little loss of resolution (Fig. 3.7(c)).

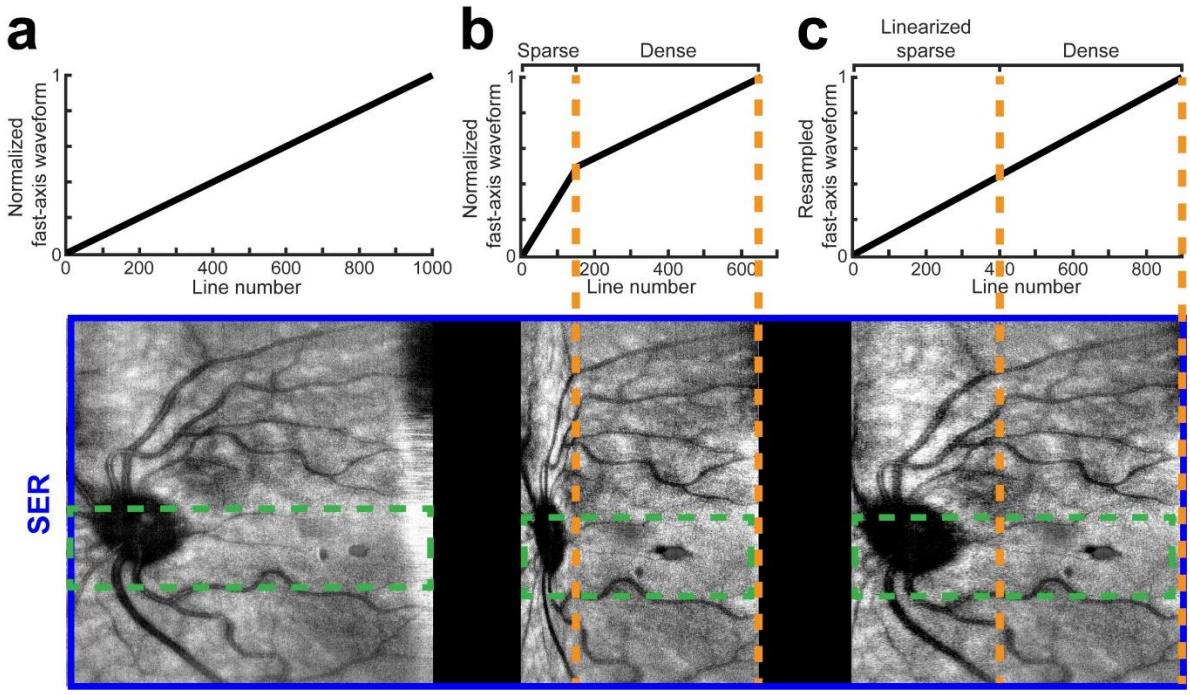

Figure 3.7. Variable-velocity scanning protocol. (a) Protocol for linear dense sampling of the fovea and optic nerve head. The SER image (bottom, blue) shows the FOV extended out to the optic nerve head, which provides additional artifact fiducials for motion-compensation of the OCT (dashed green). (b) Variable-velocity scan protocol for dense sampling of the ROI (fovea) and sparse sampling of the periphery (optic nerve head). (c) Resampled SER image from (b) showing similar fiducial features in the linearized sparse region that can be used for registration.

3.4.3 Discussion

Here we have successfully modelled and constructed a portable SECTR engine based off of a previously-designed benchtop system. The SECTR engine was designed to fit into a compact optical enclosure that was placed onto a mobile cart for portable ophthalmic imaging, thus potentially enabling *in vivo* clinical and intraoperative imaging. In addition, engine performance was optimized by fusion-splicing power coupler connections, which significantly reduced insertion loss and resulted in a 64% increase in OCT power and 27% increase in SER power at the pupil. These improvements will improve OCT and SER image SNR, which facilitates clinical diagnostics and high-speed intraoperative imaging as well as high-accuracy *en face* motion-tracking.

In addition, we have validated the performance of the portable SECTR system that was designed and optimized. In particular, we acquired high-resolution OCTA images of ROIs located at the fovea,

optic nerve head, and periphery of the retina. We have shown that simultaneous acquisition of *en face* SER images allows for retinal tracking and motion-compensation of OCTA volumes, which facilitates the correction of out-of-plane motion and therefore significantly reduces the presence of motion artifacts. As a result, we are able to improve image quality and preserve anatomical accuracy in *en face* OCTA projections, which can improve clinical diagnostics and quantification of vascular parameters. We have also demonstrated a modified scanning protocol, variable-velocity scanning, that can be used to improve motion-tracking and registration by subsampling an extended FOV for additional artifact-free SER fiducials without sacrificing sampling density in a ROI. By doing so, we can increase imaging speed by 27% over conventional linear-sampling across the same FOV, thereby benefitting high-speed iOCT imaging applications.

CHAPTER 4

Modeling and optimization of galvanometric point-scanning temporal dynamics

The following chapter contains content that is adapted from E. M. Tang, and Y. K. Tao, "Modeling and optimization of galvanometric point-scanning temporal dynamics," Biomedical Optics Express 12, 6701-6716 (2021) [198].

4.1 Introduction

Scanning technologies are integral to a broad range of optics applications including microscopy [199]–[202], ophthalmoscopy [203]–[206], optical coherence tomography (OCT) [87], optical ranging (LIDAR) [207], and prototyping and manufacturing [208]–[211]. The most commonly used scanning technologies can be divided into four categories: resonant scanners, polygon scanners, acousto-optic deflectors (AODs), and galvanometer scanners. The temporal response of these devices is bandlimited and the corresponding finite settling time of the scanner fundamentally limits performance parameters such as scanning speed, linearity, trajectory, field-of-view (FOV), and/or resolution.

4.1.1 Resonant Scanners

Resonant scanners have high scanning speeds (> 10 kHz line rate) and low power consumption, making them ideal for microscopy [212]–[214], OCT [215], light-sheet imaging [216], and adaptive optics [204], [217]–[219]. Compact form-factor microelectromechanical system (MEMS) resonant scanners are also often used in displays and laser scanning systems [220], [221]. However, resonant scanners are limited in their ability to randomly target regions-of-interest (ROIs) because they must be driven with sinusoidal waveforms close to their resonant frequency. While the amplitude of the resonant scan waveform can be modulated, sampling along the sinusoidal scan trajectory is necessarily nonlinear and requires additional calibration, nonlinear analog-to-digital converter (ADC)

sampling, or post-processing to relinearize the acquired images [222]–[224]. Nonlinear scanning also results in nonuniform illumination/optical power deposition across samples, which contribute to increased tissue damage and photobleaching at the edges of the FOV where dwell time is increased in fluorescence applications. Acousto-optic and electro-optic modulators can be used to modulate laser intensity across the field, but these methods significantly increase system cost and complexity [225].

4.1.2 Polygon Scanners

Polygon scanners combine a high-speed motor with multiple mirror facets to achieve > 100 kHz line rates [226]–[231]. The lack of oscillatory elements enables constant linear velocity scanning over large FOVs. However, the facet size and rotation speed of polygon mirrors are fixed and, thus, also fix the FOV and minimum ADC sampling requirements. In addition, all detection electronics are generally required to be synchronized off of the polygon clock. Manufacturing and assembly of polygon mirror facets can also introduce defects that result in facet-to-facet angle variance, facet radii variance, surface nonuniformity, and surface reflectance differences [232]. Polygon mirror scan angles are directly proportional to the number of facets, thus, requiring custom-designed scan optics to match specific mirror geometries. The size of polygon mirrors is also proportional to the aperture size and number of facets, which generally precludes applications in space constrained devices, such as compact handheld devices. Applications that require descanning or two-dimensional scanning will also require complex system geometries and additional scanning/translational elements.

4.1.3 Acousto-optic Deflectors

Acousto-optic deflectors (AODs) are primarily used in applications requiring extremely high-speed scanning (> 1 MHz line rate) or randomly addressable scan trajectories because they do not require mechanical elements [233]–[235]. However, the diffraction angle of AODs is wavelength-dependent and induces chromatic dispersion that is coupled with group velocity dispersion induced by the AOD. AODs also suffer from significantly lower power throughput compared to reflective scanners (60% vs. >90% optical efficiency) due to both material dispersion and loss to multiple

diffraction orders [236]. Spatial and temporal broadening requires precompensation using prism pairs or diffraction gratings, which increase system cost, complexity, and optical loss [237]. Furthermore, the small aperture of these devices limits the maximum deflection angle and number of resolvable spots, thereby reducing the FOV and spatial resolution of the system. The wavelength-dependent deflection of AODs also prevents its use in systems that require descanning, such as in fluorescence imaging.

4.1.4 Galvanometer Scanners

Galvanometers are the most commonly used scanners for biomedical imaging [238]–[241] due to their moderate speed (> 1 kHz), low step response times (~100 μs for 3 mm apertures), and high positional accuracy [242]. Additionally, closed-loop controller feedback of mirror position can be used to optimize galvanometer inputs to improve linearity and minimize positional errors. Compared to resonant scanners, closed-loop galvanometers enable imaging of a large FOV with high linearity and adjustable speed. Galvanometers also do not suffer from facet-to-facet variability as compared to polygon mirrors or high loss and dispersive effects as compared to AODs. In addition, galvanometer pairs can be used to randomly address scan trajectories to target ROIs.

Despite the aforementioned advantages of galvanometers, their performance is directly related to response time optimizations specific to mirror size, material stiffness, weight, and alignment [242]. Previously demonstrated methods for scanner optimization include iterative learning control [243], [244], Landweber-based deconvolution [245], and optimization of input scan waveform shape, frequency, and amplitude [246]–[248]. However, these methods are dependent on a specific input scan waveform and are not robustly suitable for imaging applications that require changing the FOV, speed, or sampling density of the scan. Here, we take advantage of the closed-loop feedback of proportional-integral-derivative (PID) controllers to optimize the response of galvanometer scanners to arbitrary input waveforms. By modifying fundamental PID parameters (e.g., error proportional gain and low and high frequency damping gains), it is possible to significantly improve galvanometer controller frequency response and reduce settling time [249]–[251]. We show that we can halve

galvanometer response time to enable high speed imaging of dynamics and increased scanning FOV, which can have broad-ranging benefits in object detection, ranging, and tracking as well as other scanning applications. As a proof-of-concept, we perform functional ophthalmic imaging using optical coherence tomographic angiography (OCTA) [252], and propose several software optimization methods that leverage optimized galvanometer response times to further improve imaging performance.

4.2 Methods

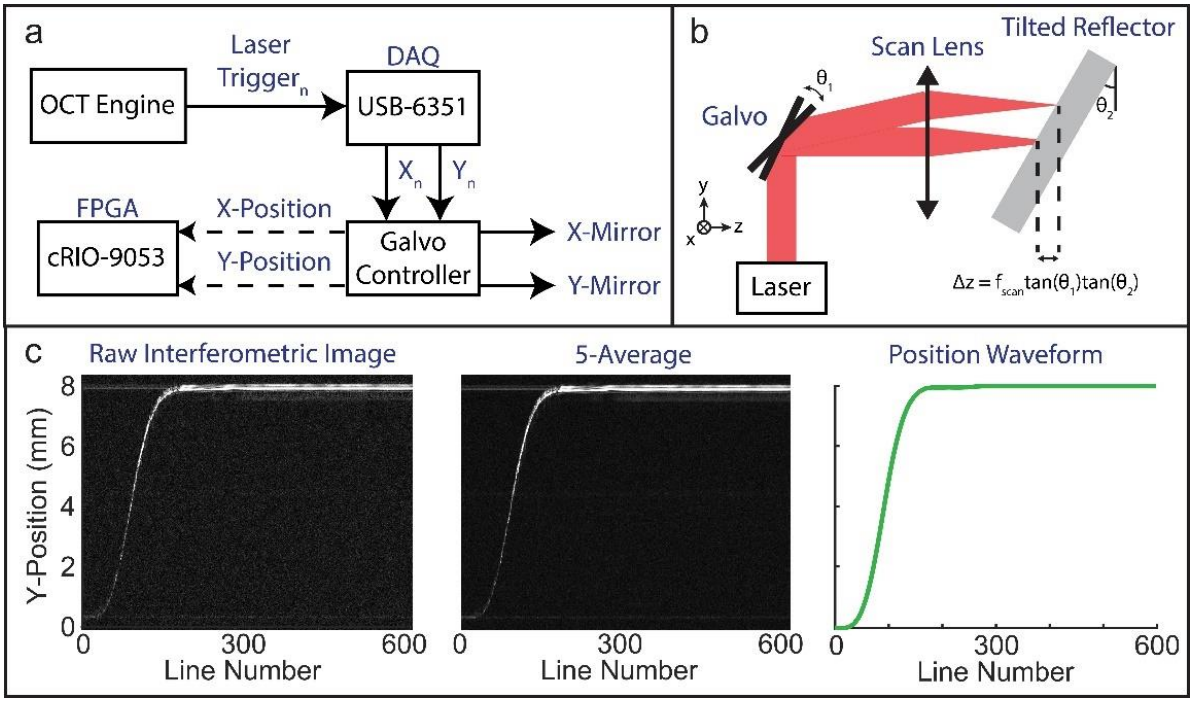

Figure 4.2. Measurements of galvanometer step response. (a) Experimental setup. A DAQ device generates X- and Y-mirror position outputs for each laser line trigger. The galvanometer controller processes the input signals and outputs them to the mirrors. A FPGA simultaneously measures the mirror positions directly from the controller. (b) Simplified diagram depicting imaging of the tilted reflector, which enables sampling of galvanometer position as a function of depth. (c) Processing and extraction of position waveforms from optical measurements.

4.2.1 Experimental Setup

Small (X) and large (Y) galvanometer mirrors with 5 mm pupil diameters (Saturn 5B, ScannerMax – Supplementary Fig. 1) were interfaced with a custom 400 kHz swept-source OCT engine [122],

[173]. Image acquisition and galvanometer scanning were synchronized using an external laser line trigger and data acquisition device (USB-6351, National Instruments). A field-programmable gated array (cRIO-9053, National Instruments) was used to stream X and Y-mirror positions from the analog output channels of the galvanometer PID controller (MachDSP, ScannerMax) (Fig. 4.1(a)).

4.2.2 Optimization Criteria

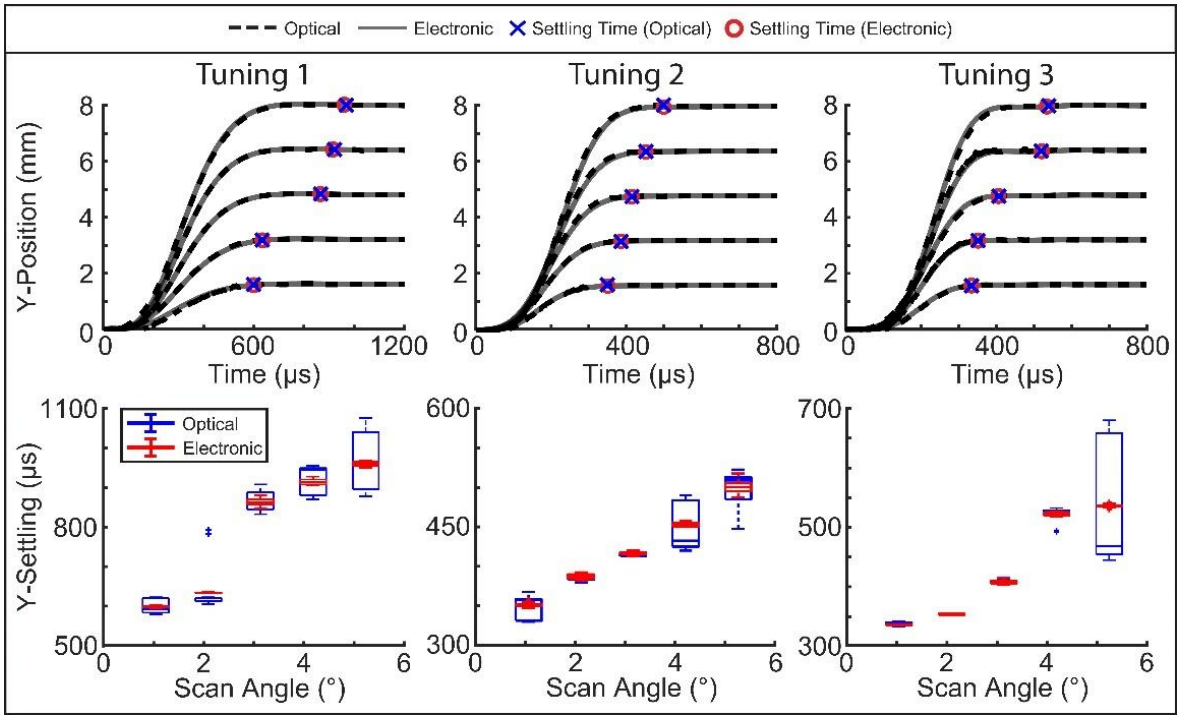

Figure 4.3. Comparison of electronically and optically measured galvanometer step response. Top row: Optically (dashed) and electronically (solid) measured Y-mirror step response and settling times (crosses and circles) for three manufacturer provided tunings at input step function amplitudes 1.6 mm, 3.2 mm, 4.8 mm, 6.4 mm, and 8 mm. Bottom row: Settling times for each tuning at different step amplitudes

Closed-loop feedback of the galvanometer controller facilitated hardware optimization by providing access to basic tuning parameters (error proportional servo gain, low and high frequency damping gain, position error integral gain, and position proportional gain) and several intermediate tuning parameters. For optimization, a settling time criterion was chosen as it provides a quantitative metric describing the performance of the PID controller for different tuning parameter values and is a direct reflection of the frequency response of the system [253]. Here, the time that the mirror took

to settle to its final position within an error band after a step response was denoted as the total settling time. In this imaging demonstration, this error band was set to the lateral resolution limit of the imaging system (11.1 μm) since oscillations below the resolution limit cannot be resolved.

Galvanometer step responses and corresponding settling times were measured electronically using mirror positional outputs from the galvanometer PID controller (Fig. 4.2(a)). PID positional outputs were validated against optical interferometry measurements made by imaging a tilted reflector with a flat scattering surface (Fig. 4.1(b) and (c)). Interferometric measurements allowed remapping of lateral galvanometer scan positions to axial displacements scaled by the tangent of the tilt angle, which effectively enables measurement of galvanometer angular position with arbitrary accuracy up to the image signal-to-noise (SNR) limit (Fig. 4.1(b)). This allowed for significantly higher spatial resolution than would otherwise be possible using standard test-chart measurements, which are sampling-limited by the convolution of imaging spot size and test-chart feature size.

The Y-mirror settling time for different input step function amplitudes and manufacturer provided PID tuning parameters were measured both electronically and optically (Fig. 4.2). Manufacturer PID tunings were designed to have high position accuracy (Tuning 1), high position accuracy and bandwidth for stable scanning at high speeds (Tuning 2), and high bandwidth (Tuning 3). A total of 100 electronic and optical measurements were acquired for each tuning and step amplitude combination. Tilted reflector depth profiles were 5-averaged to reduce noise and measurement variability, and position waveforms were referenced to the axial intensity peak. Electronic and optical measurements of settling times and positions were equivalent (Fig. 4.2, top row) and statistical analysis showed no significant difference ($p > 0.05$) between the methods (Fig. 4.2, bottom row). Large standard deviations in the optical measurements are from underdamped responses caused by ringing of the mirror during settling that was likely filtered by the PID controller onboard electronics and not present in the corresponding electronic measurements. This was not a limitation of the electronic measurements, because the mean settling time in underdamped cases were consistently higher than critical damping cases and subsequently removed from the galvanometer optimization

search space. Given this validation data, all subsequent measurements were made electronically, which obviated the need for image post-processing, showed significantly decreased measurement variability related to spatial differences in scattering across the tilted reflector, and may be directly implemented without specialized test equipment.

4.2.3 Gaussian Process Regression

Galvanometer optimization was performed by iteratively modifying PID tuning parameters using manufacturer-provided controller software to minimize step response settling time. First, a sparse sweep of the 5 basic parameters (error proportional servo gain, low and high frequency damping gains, position error integral gain, position proportional gain) was performed. Each parameter was incremented by a step size of 100 over a full range of 0-1000. Figure 3 shows an example of a single optimization iteration for 2 parameters. For each set of parameters, a position waveform was measured, and the corresponding settling time was calculated as the time from the step start to when the position waveform settled to within a lateral full-width at half-maximum (FWHM) spot size (11.1 μm) of the final steady-state position (Fig. 4.3(a)). Parameter values that caused the scanner to be unresponsive were excluded, resulting in a total of 10,602 unique basic parameter configurations (N_1).

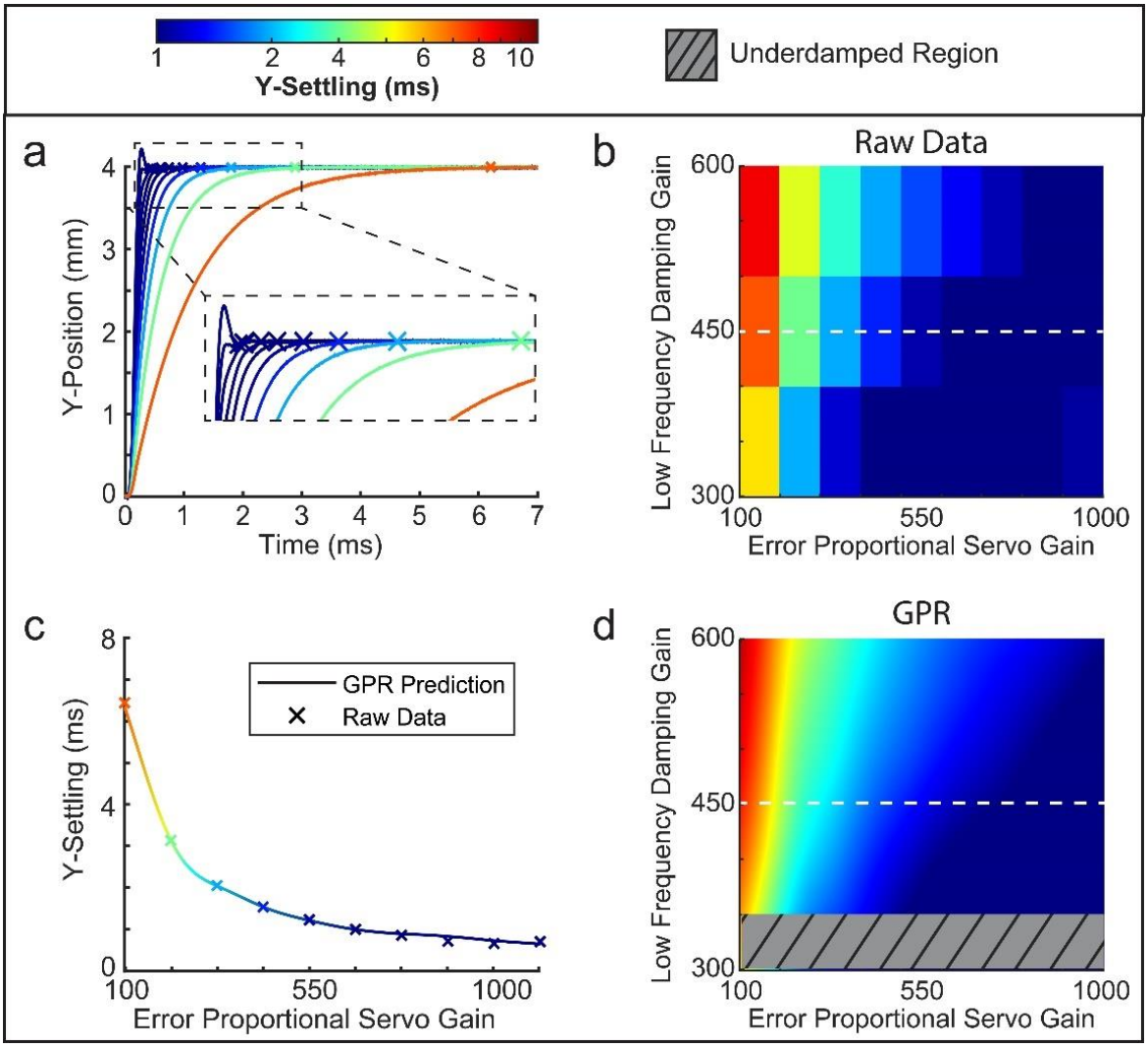

Figure 4.4. Y-mirror settling time measurement and modeling example. (a) Raw position waveforms and corresponding settling times (cross) for increasing error proportional servo gain (right to left lines). (b) Heat-map aids visualization of settling time trends as a function of tuning parameters (dashed line corresponds to settling times in (a)). (c) Raw settling time data (cross) was used to generate a (d) 5-dimensional Gaussian process regression model used to predict global optimum tuning parameters.

A Gaussian process regression (GPR) model of settling time values was created (MATLAB, MathWorks) to narrow down the range of optimal basic parameter values over the complex nonlinear parameter space. GPR is a nonparametric, Bayesian regression method with significant performance advantages over conventional linear regression models [254], [255]. In general, a Gaussian process is defined as a multivariate Gaussian distribution where each observation acts as a random variable.

Thus, for N given data points or observations, the corresponding Gaussian process would be N-dimensional. As a result, each data point has an associated mean and covariance describing the probability distribution of values for that specific input. GPR modeling begins with an assumed prior distribution that will be updated given a set of observations:

$$S_0 \sim \mathcal{N}\left(\mu_0, K(X_0, X_0)\right) \tag{4.1}$$

Here, the prior settling time distribution, S_0, is defined as a joint Gaussian distribution with a mean of $\mu_0 = 0$ and a covariance matrix $K(\mathrm{X}_0, X_0)$, where:

$$K(X_0, X_0) = \begin{bmatrix} k(x_0^1, x_0^1) & \cdots & k(x_0^1, x_0^N) \\ \vdots & \ddots & \vdots \\ k(x_0^N, x_0^1) & \cdots & k(x_0^N, x_0^N) \end{bmatrix} \tag{4.2}$$

The covariance matrix, K, is created by evaluating a covariance kernel function k for each combination of inputs X_0 that span the parameter tuning space. The most common class of covariance kernel functions used is the Matérn class [256], which describes the similarity between two inputs and therefore between model outputs as well. One case of the Matérn class of functions is the squared exponential or Gaussian function:

$$k(x, x') = \sigma^2 \exp\left(-\frac{\left||x - x'|\right|^2}{2l^2}\right) \tag{4.3}$$

In this case, σ^2 and l^2 are hyperparameters corresponding to the signal variance and length-scale, respectively. Gaussian processes with small signal variance produce values that stay close to the mean while those with large signal variance tend to deviate from the mean. Furthermore, Gaussian

processes with a small length-scale tend to change rapidly while those with a large length-scale vary more slowly and are therefore smoother. By optimizing hyperparameter values, it is possible to generate a more robust prior distribution that better fits the signal trends of observed data, thus improving model accuracy.

The goal of GPR is to calculate a posterior probability distribution for predicting optimal settling time parameter values based on the initial prior settling time distribution and training observations. Given a set of settling time observations, $[x_t, S_t]$, the posterior probability distribution, $S' = P(S_0|S_t)$, can be calculated:

$$S' \sim \mathcal{N}\left(\overbrace{K(X_0, X_t)[K(X_t, X_t)]^{-1} S_t,}^{\text{Posterior Mean}} \underbrace{K(X_0, X_0) - K(X_0, X_t)[K(X_t, X_t)]^{-1} K(X_t, X_0)}_{\text{Posterior Covariance}}\right) \tag{4.4}$$

The posterior mean formula suggests that the prior settling time mean ($\mu_0 = 0$) is shifted to match the observed settling time values. Thus, inputs to the model that are closer to the observed parameter inputs will produce mean values closer to the observed settling time values. Similarly, the posterior covariance suggests that input parameters closer to the observed settling time inputs will have a lower variance.

GPR model training and optimization of the kernel function and corresponding hyperparameter values via 5-fold cross-validation was performed in MATLAB. Comparisons between optimal GPR performance and that of conventional regression methods, such as linear regression, decision tree regression, and support vector machine regression were also computed.

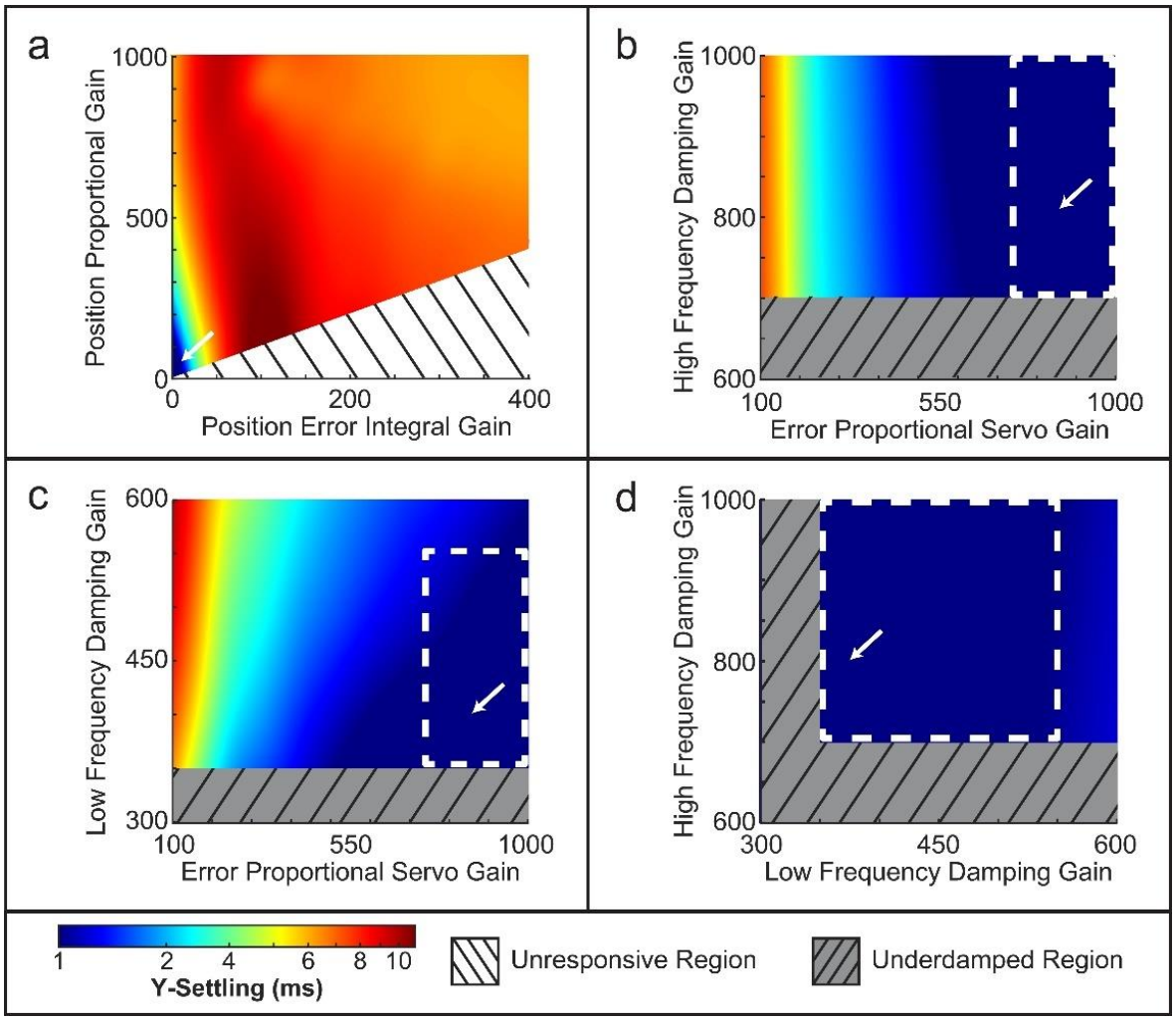

Figure 4.4. Gaussian process regression predictions for the Y-mirror. (a) GPR model heat map of settling time as a function of position error integral gain and position proportional gain. Arrow shows minimum predicted settling time and optimal galvanometer step response when both parameters are 0. (b)-(d) Settling time heat maps for three remaining basic PID tuning parameters and position error integral gain and position proportional gain set equal to 0. Dashed white boxes show the predicted optimal range of values used to narrow the parameter search space in each dimension (arrow, minimum settling time).

Galvanometer positional waveforms with underdamped step responses were excluded from the training data in order to improve the accuracy of the model for identifying optimal basic tuning parameters (Fig. 4.3(d)). GPR model predictions following the initial sweep showed optimal values of 0 for position error integral gain and position proportional gain (Fig. 4.4(a)), allowing for a reduction in dimensionality. A second parameter sweep was performed for the 3 remaining basic parameters (error proportional servo gain and low and high frequency damping gains) over a GPR

predicted optimal range for each parameter with a step size of 50 (Fig 4(b)-(d)). In addition, intermediate PID tuning parameters (low and high frequency damping filter cutoffs) were incremented from 5000-9000 Hz with a step size of 500 Hz for a total of 7,056 unique tuning configurations (N_2). Iterative parameter sweep and GPR model training was repeated until global optimum basic and intermediate PID tuning parameters were identified.

4.3 Results

Galvanometer tuning optimization significantly reduced Y-mirror settling time as compared to default tunings for all measured input step amplitudes (Fig. 4.5, p << 1E-10). Specifically, the measured step responses show that settling time improves by 31-61% over manufacturer provided tunings for small input step amplitudes. For large step amplitudes, the optimized PID tuning improves settling time by 11-54%. Similarly, the optimized X-mirror tuning resulted in a 35-59% reduction in settling time as compared to the default tunings for a 4.5 mm (2.61 degree) step amplitude.

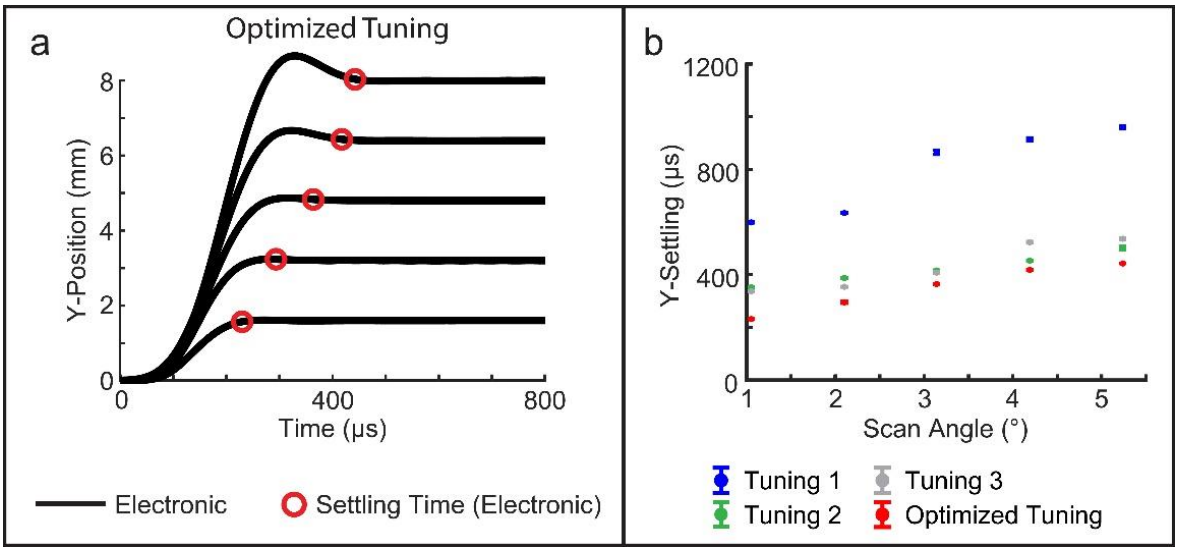

Figure 4.5. Optimized tuning performance comparison. (a) Optimized tuning step responses and settling times for varying input step amplitudes. (b) Comparison between the settling times as a function of step angle measured for each PID tuning.

Motion during imaging integration time degrades lateral resolution by smearing the focal spot. Galvanometer response time plays a prominent role in this loss of resolution at FOV edges where

scanning mirrors transition to and from high-speed return waveforms. Using measured galvanometer positions during these transitions, we computed the lateral motion between serial samples and effective lateral resolution normalized by the spot size compared against the Nyquist criterion conventionally used in point-scanning applications (Fig. 4.6). Expectedly, the optimized galvanometer had the highest resolution loss (>4 x FWHM), but also settles below the Nyquist sampling criterion 20-51% faster than those with default tunings. These results reiterate the advantage of optimized settling times and highlight the importance of quantitating galvanometer dynamics for point-scanning systems. Smeared and subsampled regions are routinely cropped and discarded, but galvanometer response dictates the amount of discarded data and, importantly, whether spatial resolution across the imaging FOV is uniform.

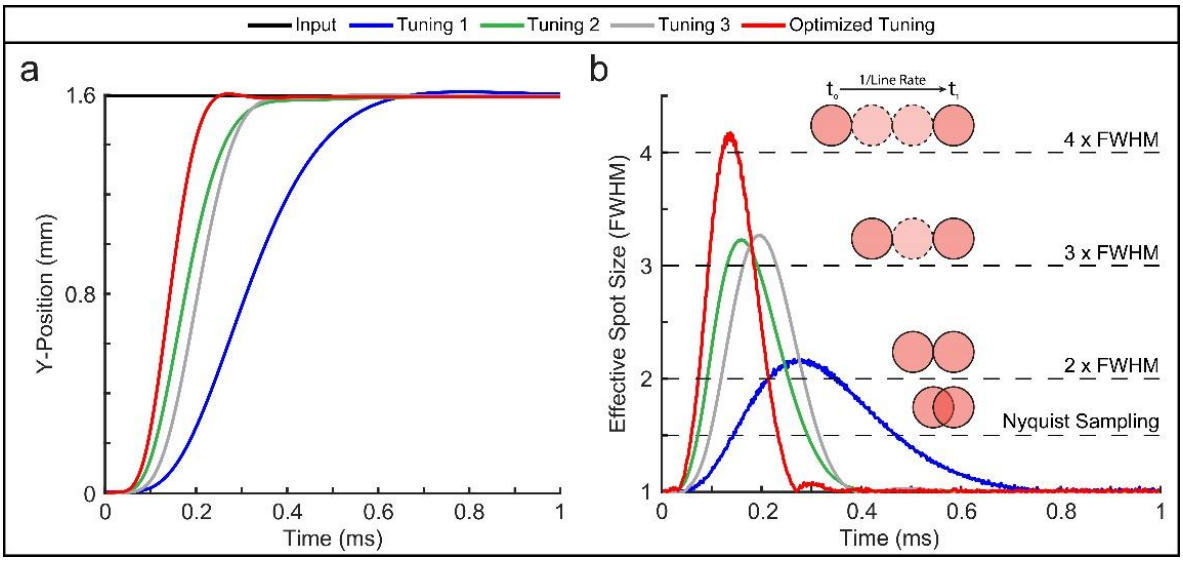

Figure 4.6. Degradation of lateral resolution from galvanometer motion. (a) Galvanometer position waveform during a high-speed galvanometer positional reset. (b) Corresponding effective lateral resolution normalized by spot size FWHM.

The effect of optimized galvanometer response on point-scanning based imaging was validated using a fine distortion target (R1LS3P, ThorLabs) with a grid size of 10 µm and 50 µm spacing. In addition, we demonstrated the benefits for functional OCTA imaging, 4D imaging of dynamic motion, and bi-directional scanning.

OCTA volumes were acquired in a healthy adult volunteer under an IRB-approved protocol using a handheld ophthalmic imaging probe. Sampling parameters were chosen to densely sample a small ROI below the central fovea of the retina (Table 4.1). Raster-scanning OCTA was performed using sampling protocol 1, which included a linear scan waveform (300 lines) and sinusoidal return waveform (500 lines) that set a fixed interscan delay of 2 ms between frames to visualize capillary flow. Linear scanning regions were identified as galvanometer positions with error deviations less than a spot size measured using corresponding PID controller positional readouts and the corresponding OCTA images for each tuning (Fig. 4.7(b)) show that the optimized tuning has a 6-49% increase in linear FOV over the manufacturer provided tunings. In addition to FOV differences, the nonlinear scanning regions (Fig. 4.7(b), (d), (f), red) show feature deformations and degraded lateral resolution.

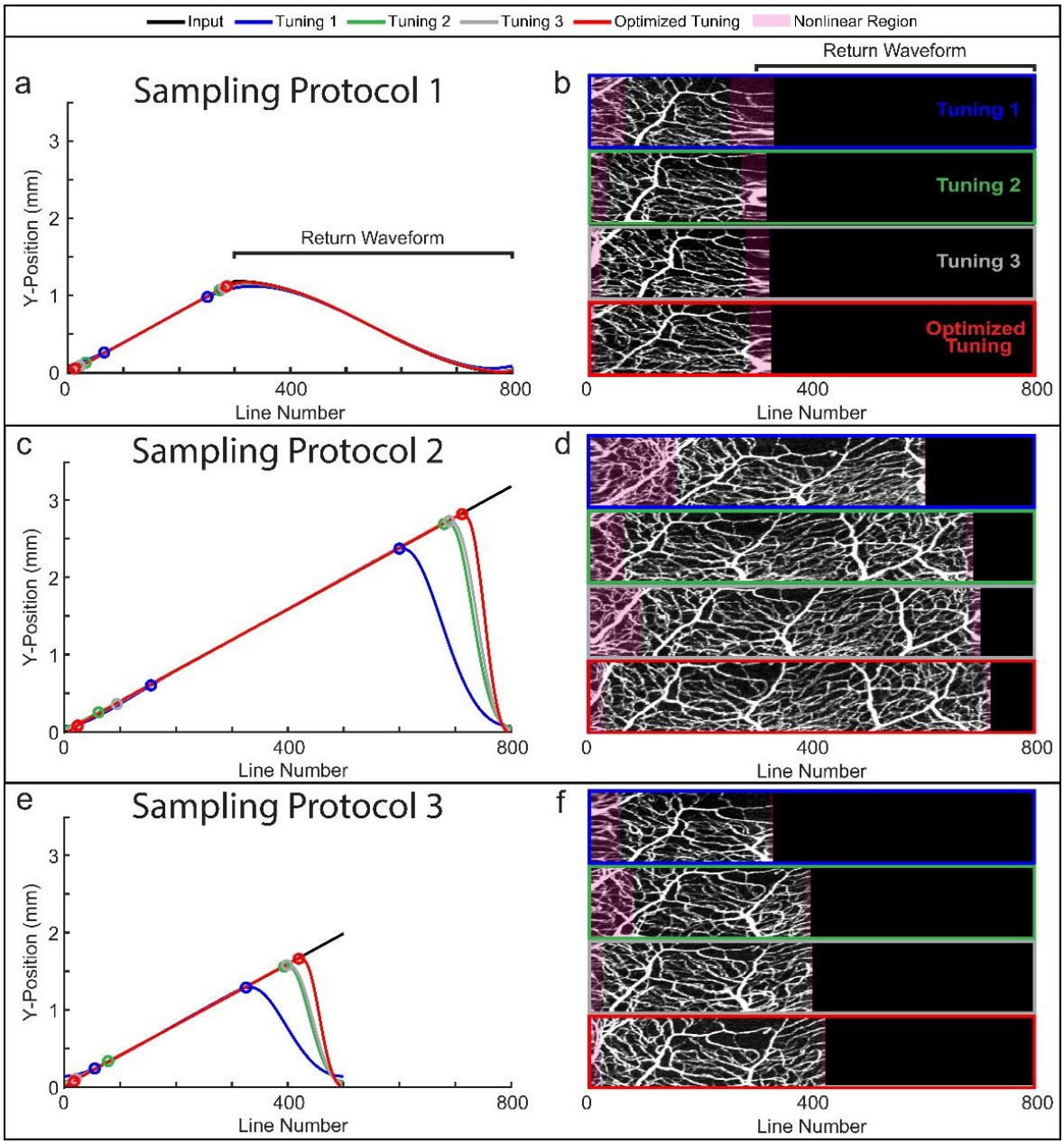

Figure 4.7. OCTA acquisition protocol comparison. (a) Sampling Protocol 1 – Conventional OCTA scan waveform, measured position, and (b) corresponding *en face* OCTA projection for dense sampling of a small ROI. Regions of linear sampling are denoted by the colored circles. Nonlinear scan regions are highlighted in red on OCTA projections. (c) Sampling Protocol 2 – Modified scan waveform and (d) corresponding OCTA showing increased linear FOV by eliminating return lines between frames. (e) Sampling Protocol 3 – Modified scan waveform and (f) corresponding OCTA showing increase in linear FOV and decreased interscan delay.

Table 4.3. Sampling protocols for OCTA imaging.

Sampling Protocol	Linear Scan Waveform (lines)	Return Waveform (lines)	Frames per Volume	Repeated Frames	Interscan Delay	Volume Acquisition Time
1	300	500	200	5	2 ms	2 s
2	800	0	200	5	2 ms	2 s
3	500	0	200	8	1.25 ms	2 s

We also evaluated the robustness of our galvanometer optimization to modified scan waveforms that benefit functional imaging by either increasing the linear FOV (Fig. 4.7(c) and (d)) or image SNR and contrast-to-noise (CNR) ratio (Fig. 4.7(e) and (f)). The following formulas were used to calculate CNR and SNR:

$$CNR = 20 * \log_{10}\left(\frac{\mu_{ROI}}{\sigma_{noise}}\right) \tag{4.5}$$

$$SNR = 20 * \log_{10}\left(\frac{I_{peak}}{\sigma_{noise}}\right) \tag{4.6}$$

Sampling protocol 2 increases the linear FOV by extending the linear scan waveform and removing the return waveform (Fig. 4.7(c)). The number of lines per frame and, thus, the interscan delay remain constant to maintain vascular flow velocity sensitivity. Sampling protocol 2 increases the linear FOV by 134-159% over sampling protocol 1 (Fig. 4.7(b) and (d)). Sampling protocol 2 effectively uses a sawtooth waveform, and since no return waveforms are explicitly sent to the PID controller, the length of the nonlinear galvanometer positional reset period is ultimately determined by its frequency response. Here, our optimized PID tuning increased the linear FOV by 12-55% over manufacturer provided tunings. As expected, by maintaining interscan delay, no significant differences in average image CNR or SNR were observed (Fig. 4.8(b) and (c)).

Optimized galvanometer response and modified scan waveforms can similarly be leveraged to improve image CNR and SNR. Sampling protocol 3 both extends the linear scan waveform and

removes the return waveform from sampling protocol 1 to increase the linear FOV while reducing the interscan delay. Sampling protocol 3 increases the effective imaging frame rate such that the total number of repeated frames can be increased while maintaining total volume acquisition time (Fig. 4.7(e)). Again, there is a significant increase in linear FOV (30-49%, Fig. 4.7(b) and (f)) and mean SNR and CNR as a result of frame-averaging (8.8% and 6.7%, respectively, Fig. 4.8(b) and (c)) as compared to sampling protocol 1.

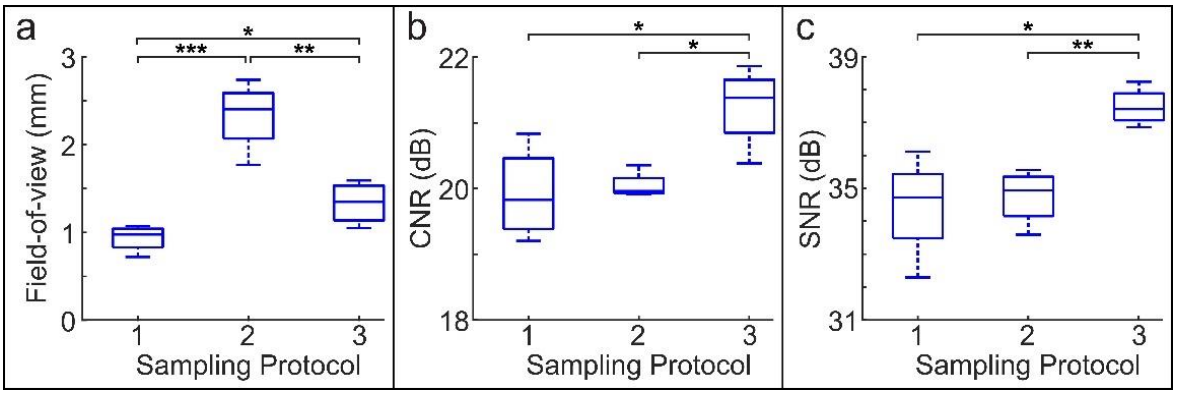

Figure 4.8. Comparison between (a) linear FOV, (b) CNR, and (c) SNR between sampling protocols (* $p < 0.05$, ** $p < 0.01$, *** $p < 0.001$).

We demonstrate the benefits of optimized galvanometer response for 4D volumetric imaging of dynamic motion by comparing conventional (300 lines, 300 return lines, 100 frames) and optimized (370 lines, 0 return lines, 100 frames) sampling protocols over a 4 x 4 mm FOV (Fig. 4.9). Similar to OCTA protocols, return lines refer to a dedicated sinusoidal return waveform in the conventional protocol whereas the optimized protocol uses a sawtooth scan waveform without a dedicated return waveform and galvanometer positional reset occurs in the additional 70 lines of the scan (Fig. 4.7(c) and (e)). These return and reset regions were cropped, yielding identically sized and sampled volumes with 2560 x 300 x 100 pix. (depth x lines x frames). Optimized sampling improves volumetric imaging speed by 62% over conventional sampling, enabling visualization of dynamic motion with fewer motion artifacts and distortions (Fig. 4.9(c) and (d); Visualizations 1 and 2).

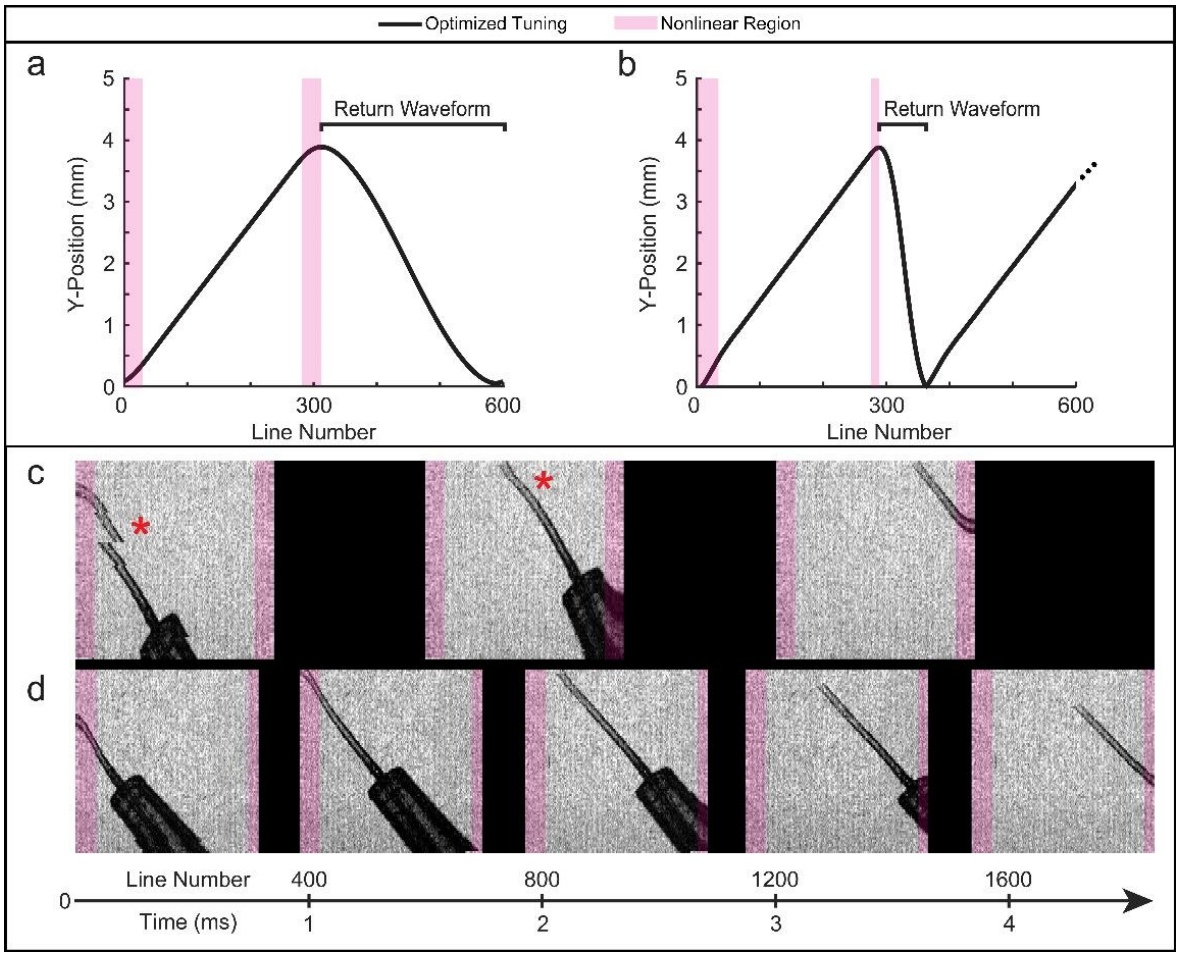

Figure 4.9. 4D imaging of cannula dynamic motion using (a) conventional and (b) optimized sampling parameters. The series of acquired *en face* volume projections show (c) conventional sampling at lower volume rates (6.67 Hz) compared to (d) optimized sampling (10.81 Hz). Slower volume-rates result in discontinuities and distortion of the cannula tip (asterisk). Nonlinear scan regions are highlighted in red and show image distortions and degraded lateral resolution effects observed in Figures 4.6 and 4.7.

Finally, we evaluated the benefits of optimized galvanometer response for bi-directional scanning, which can be used to effectively double scan speeds. Bi-directional galvanometer scanning can be limited by ringing at the sharp transition points, especially at higher scan speeds [247]. Here, the positional residual error with respect to the input waveform (Fig. 4.10) shows that our galvanometer optimization increases the linear FOV by 3-126% as compared to manufacturer provided PID tunings.

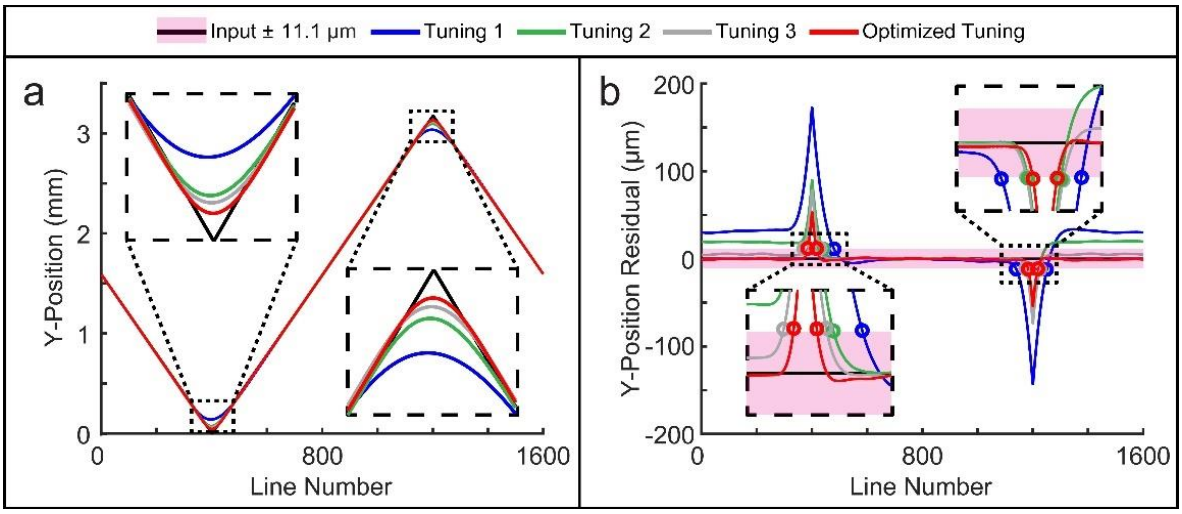

Figure 4.10. Tuning comparison for bi-directional scanning. (a) Measured Y-mirror position waveforms from the galvanometer controller for an input bi-directional scan waveform and insets showing differences between tunings. (b) Position residuals used to calculate linear regions for each tuning within the lateral resolution error band. Start and stop positions for linear regions are shown by the corresponding colored circles.

4.4 Discussion and Summary

Scanning technologies require robust high-speed performance. Galvanometer scanners are not constrained by fixed frequency, fixed FOV, or highly lossy/dispersive operation that limits resonant, polygon, and acousto-optic scanners. However, the performance of galvanometers is fundamentally limited by frequency response, which impacts settling time, sampling linearity, lateral resolution, and speed. By taking advantage of the closed-loop feedback unique to galvanometer controllers, it is possible to reduce the step response settling time by over 50% as compared to manufactured defaults. This reduction benefits applications requiring rapid scanning, such as 4D volumetric imaging, bi-directional scanning, and real-time tracking of ROIs.

The proposed hardware optimization also has significant advantages over previously reported methods, which are restricted to specific input waveforms. Here, we present methods of optimizing PID tuning parameters and the corresponding frequency response of the galvanometer controller, making the optimized tuning input-independent. As a result, it is possible to combine both hardware and software optimizations to further improve scanner performance and tailor scan waveforms

specific to broad applications. Importantly, the method presented may be directly implemented without the use of specialized test equipment because we demonstrated that positional feedback from the galvanometer PID controller is sufficient for evaluating mirror response. As a proof-of-concept, we demonstrated hardware and software optimizations to increase linear FOV and image SNR/CNR in OCTA as well as to increase speed for rapid volumetric imaging. However, similar advantages can be broadly achieved in point-scanning applications in imaging, display, ranging, manufacturing, and therapeutic technologies.

CHAPTER 5

Automated instrument-tracking for 4D video-rate imaging of ophthalmic surgical maneuvers

The following chapter contains content that is adapted from E. M. Tang, M. T. El-Haddad, S. N. Patel, and Y. K. Tao, "Automated instrument-tracking for 4D video-rate imaging of ophthalmic surgical maneuvers," Biomedical Optics Express 13, 1471-1484 (2022) [257].

5.1 Introduction

Rapid development of imaging technologies has facilitated the use of intraoperative image-guidance in a broad range of medical fields including neurology [258]–[261], ophthalmology [262]–[264], hepatology [265]–[267], and oncology [268]. Image-guided surgery provides enhanced visualization of instrument-tissue interactions and is especially useful when haptic feedback is limited such as in ophthalmic microsurgery, minimally-invasive surgery, and robotic surgery [269]. In these cases, endoscopic or microscopic video feeds are used to relay information regarding instrument position back to the surgeon. However, intraoperative imaging tends to suffer from nonuniform illumination, noise, specular reflections, and variations in the surgical environment that ultimately limit the accuracy of instrument pose estimation and instrument-tracking [83], [84]. Instrument fiducials can be used to facilitate registration and tracking, but these methods assume a rigid relationship between the instrument tip and physical space [191]. These factors are also often confounded by surgical dynamics, which result in changes in instrument shape and orientation as well as movement of the instrument out-of-focus during surgery.

5.1.1 Ophthalmic Surgery

Image-guided ophthalmic microsurgery has been demonstrated using intraoperative optical coherence tomography (iOCT) and provides significant benefits compared to conventional microscopic surgery, which offers limited contrast and feedback for submillimeter-thick tissues and

precludes visualization of subsurface features [270]. The development of iOCT technology through the use of microscope-mounted handheld probes [127], [136] and microscope-integrated OCT systems [128], [131] addresses these limitations by enabling high-resolution volumetric imaging of supine patients during surgery. Recent studies have shown that iOCT helps to visualize structural changes during surgery that ultimately guide intraoperative decision-making, result in modification of surgical management, and enable verification of surgical goals [132], [134], [135], [139]. Furthermore, preliminary results show that patients undergoing iOCT-assisted macular hole surgery have a higher single-operation success rate and significantly improved visual acuity post-operation [271]. Despite the aforementioned benefits, the broad adoption of iOCT technology is hindered by slow imaging speeds and a lack of automated instrument-tracking, which prevents video-rate 4D visualization and requires manual adjustment of the OCT field-of-view (FOV) [272].

5.1.2 4D Video-Rate iOCT

The safety, utility, and efficacy of commercial iOCT systems such as the Rescan 700 (Carl Zeiss Meditec) and the Enfocus (Leica Microsystems) have been well-established for ophthalmic surgery [273], [274]. However, these systems operate at line-rates between 10 – 32 kHz, which limits current visualization to static cross-sectional images and prevents 4D imaging of surgical dynamics [275]. Recent developments in high-speed swept-source laser technology have enabled 4D video-rate OCT imaging. These research-grade systems are over an order of magnitude faster than current commercial iOCT systems and are capable of imaging at line-rates between 100 kHz – 1.67 MHz and at volume rates over 10 Hz [276]–[279]. 4D imaging of surgical maneuvers provides enhanced feedback of instrument-tissue interactions, which can be used to monitor tissue deformation and prevent damage to underlying ocular tissues. However, these systems suffer from an inherent trade-off between speed, sampling density, and FOV. Imaging at higher speeds reduces detector integration time per scan position, thus limiting system sensitivity [90]. On the other hand, it is possible to maintain high sensitivity by increasing sampling density at the cost of speed or FOV.

5.1.3 Automated Instrument-Tracking

Currently, iOCT imaging is performed over a static FOV, thus necessitating custom scan software to offset iOCT scan positions to regions-of-interest (ROIs) and requiring a trained technician to be able to accurately follow instrument positions intraoperatively [176]. Manual adjustment of the OCT FOV during surgery disrupts surgical workflow and has been shown to increase operating times by up to 25 minutes despite the presence of a trained technician [280]. Several automated instrument-tracking methods have been previously developed to segment axial position and estimate instrument pose from OCT B-scans and volumes [177]–[180]. However, these methods assume that the instrument is continuously localized within the OCT FOV and are thus unable to track lateral movements of the instrument across the surgical field. This issue is confounded by the fact that iOCT imaging is often limited to small ROIs in order to achieve 4D visualization. Our group has previously demonstrated a stereo-vision tracking system that decouples lateral instrument-tracking from axial OCT imaging, enabling tracking with high speed and accuracy across a larger FOV [281]. However, stereo-vision-based tracking methods [181]–[183] require fiducial markers to be placed on the back of instruments and therefore do not account for field distortion and instrument deformation inside the eye, which result in a nonlinear relationship between fiducials and tracked features. Furthermore, movement of the patient and of the eye dynamically changes the frame of reference during operation.

Conventional instrument-tracking methods for surgery involve the use of color features, instrument geometry, or gradient-based edge detection [282]–[286]. These methods perform well in controlled lab environments, but tend to suffer *in vivo* due to changes in appearance and lighting conditions, motion blur, and specular reflections. Recently, deep-learning algorithms have been shown to be more robust to variations in the surgical environment while also maintaining a high tracking accuracy on the order of several pixels of error and a high tracking speed of over 30 Hz [185]–[187].

Here, we present an automated instrument-tracking method for ophthalmic microsurgery that leverages multimodal imaging and recent advances in deep-learning-based object detection. We use

a high-speed spectrally encoded coherence tomography and reflectometry (SECTR) system that combines *en face* spectrally encoded reflectometry (SER) and cross-sectional OCT imaging for automated instrument-tracking and video-rate 4D imaging [122], [173]. A convolutional neural network (CNN) is trained to detect 25-gauge internal limiting membrane (25G ILM) forceps from SER images, and OCT scanning is automatically updated based on instrument position. We also present an updated method for adaptive-sampling by optimizing input scan waveforms to densely sample instrument-tissue interactions without sacrificing speed or FOV [287]. We show that we are able to achieve resolution-limited detection accuracy across the OCT imaging range, and as proof-of-concept, we demonstrate 4D tracking of surgical maneuvers in a phantom at 16 Hz volume rate.

5.2 Methods

5.2.1 Automated Instrument-Tracking Framework

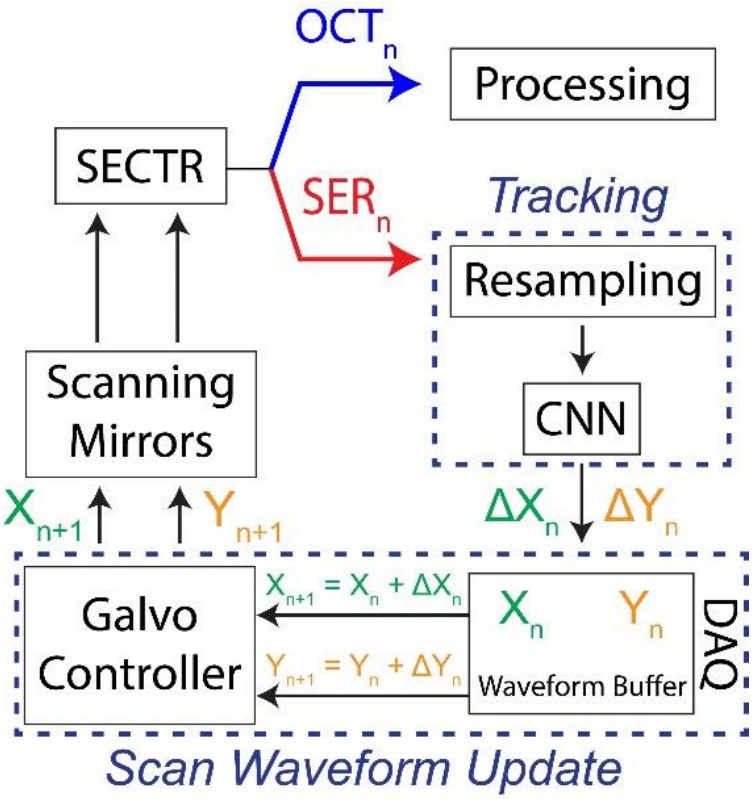

Fig. 5.5. Automated instrument-tracking framework.

The framework for our proposed automated-instrument tracking method (Fig. 5.1) can be divided into three main processes: simultaneous acquisition of OCT and SER images, detection of instrument position from SER images, and scan waveform modification based on instrument position outputs to re-center the OCT FOV. Despite the fact that these processes occur in series, the overall workflow must be highly parallelized in order to minimize latency between steps. In particular, automated instrument-tracking requires dynamic modification of SECTR scan signals at high speeds necessary for video-rate 4D imaging.

5.2.1.1 SECTR Acquisition

A custom-built SECTR engine was used to simultaneously generate *en face* SER and cross-sectional OCT images. OCT imaging is performed by raster scanning a galvanometer pair (X-Y) separated by a unity-magnification 4f optical relay to maintain telecentricity. SER uses a transmissive grating to spectrally-disperse broadband illumination, which is then optically relayed using a 4f relay across the OCT fast-axis scanning galvanometer (X). SER illumination on the sample consists of a focused line extended source in the spectrally-encoded axis that is aligned to the OCT slow-axis (Y). SER and OCT beam paths use a shared swept-source laser and optics to ensure collinearity and spatiotemporal co-registration, allowing for the acquisition of a single *en face* SER image (X-Y) and a single OCT B-scan (X-Z) for each sweep of the fast-axis (X) galvanometer mirror. As a result, we are able to use SECTR imaging to track *en face* features, such as surgical instrument position, from SER images and directly correlate those features with respect to the position of the OCT scan FOV.

Here, we modified our previous benchtop design [288] by moving engine components into a compact optical enclosure placed on a portable cart for clinical application. An optical buffer was used to double the laser sweep rate in order to achieve a 400 kHz line rate for rapid volumetric imaging. In addition, fiber connections were fusion-spliced with each other to minimize insertion loss and optimize the throughput of the system. A high-speed digitizer (ATS-9373, AlazarTech) was used to simultaneously acquire SER and OCT data at 2 gigasamples/second for real-time processing and

display. Custom C++ software was used to synchronize scan waveform generation via a DAQ (USB-6351, National Instruments) with data acquisition.

5.2.1.2 CNN Detection

Similar to intraoperative imaging variability, SER images acquired using SECTR tend to suffer from image artifacts that preclude the use of traditional instrument-tracking and segmentation methods.

Here, we leverage deep-learning-based instrument-tracking techniques by using a GPU-accelerated CNN [289] for detection of surgical instruments from SER images. In particular, the network implementation utilizes the OpenCV Deep Neural Network library and the NVIDIA GPU Computing Toolkit (CUDA) for rapid training and detection. The open-source network was trained using 4730 manually-labelled SER images of 25G ILM forceps. SER images were acquired in paper phantoms (N = 4290), retinal phantoms (N = 254) and *ex vivo* bovine eyes (N = 186). In addition, data augmentation was performed by utilizing a horizontal flip and 90º clockwise rotation for each image. The augmented data was then split between training (80%) and validation (20%) sets. CNN training was performed on a computer with an Intel i9-10900X CPU, an NVIDIA GeForce RTX 2080 Ti GPU and 64 GB RAM. Training was run for 400,000 epochs over the course of 24 hours, resulting in a mean average precision value of > 99% based on a complete intersection over union (CIoU) loss function [290].

CNN model and weights were integrated directly with the SECTR C++ acquisition software for real-time detection of SER images. Multithreaded programming was used to decouple SECTR acquisition from CNN detection by copying acquired SER images to a buffer. A parallel thread then passed the stored SER image through the trained network for high-speed detection at over 120 Hz.

5.2.1.3 Scan Waveform Modification

Finally, scan waveforms must be updated on a volume-by-volume basis for smooth 4D visualization, which corresponds to update rates of at least 16-20 Hz. Typical DAQ devices used to generate scan waveform signals operate in regeneration mode, where scan waveforms are

preallocated to an onboard waveform buffer (Fig. 5.2, red). As a result, scanning must be paused and restarted in order to update scan waveforms. Here, we take advantage of a nonregenerative operating regime that allows us to dynamically modify waveform values per scan volume. An additional thread is used to continuously monitor the size of the waveform buffer and automatically modify and write new values immediately when the buffer is empty (Fig. 5.2, blue).

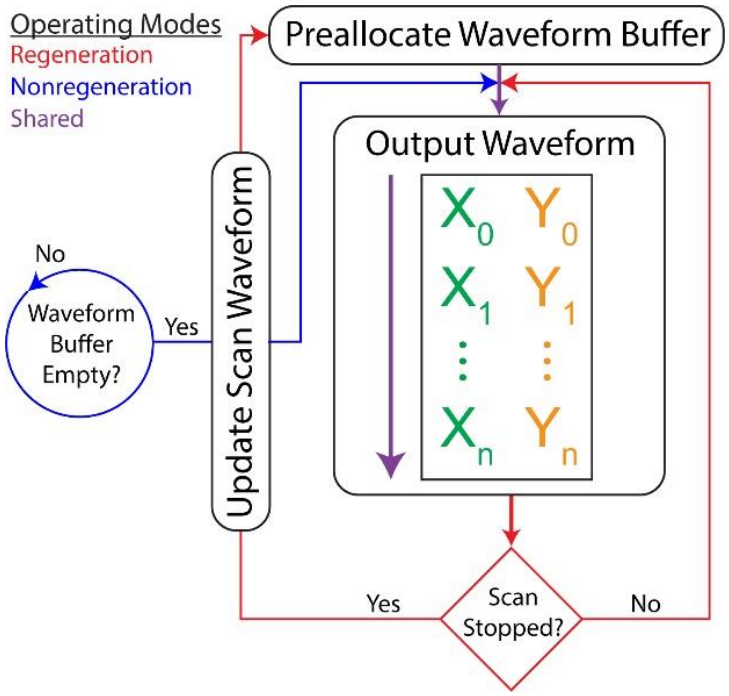

Fig. 5.6. DAQ operating modes. Regeneration mode allows continuous output from the scan waveform buffer. Nonregeneration requires new values to be written to the buffer, but enables dynamic scan waveform updates.

The CNN outputs bounding box coordinates (x, y, width, height) corresponding to the top left coordinate (x, y) of the detected surgical instrument for right-handed cases or the top right coordinate (x + width, y) for left-handed cases (Visualization 1). These values were sent directly to the waveform generation thread and used to update scanning outputs. CNN position to galvanometer scan waveform voltage offset calibration was accomplished by fitting measured offsets used to center the OCT FOV around the instrument from different initial positions (Fig. 5.3(a)). Due to adaptive-sampling of the

fast-axis (see Section 5.2.2), a higher order fit was required to calibrate the nonlinear offset-to-position curve. On the other hand, the slow-axis was linearly-sampled and therefore required only a linear fit. The design of the SECTR system enabled independent calibration of the fast- and slow-axes since each scan mirror is conjugate to the other through a 4f imaging relay. Furthermore, in order to optimize imaging performance, galvanometer scanners (Saturn 5B, ScannerMax) were tuned using a previously-reported method to maximize scan speed and linear FOV for 4D imaging [198].

5.2.2 Adaptive-Sampling

Additionally, input scan waveforms were modified by using an adaptive-sampling protocol (Fig. 5.3(b)-(d)), which allowed us to dynamically re-center the densely-sampled region of each OCT volume with the automatically-tracked instrument position to enhance visualization of instrument-tissue interactions. The original linear scan waveform prior to adaptive-sampling can be described mathematically as:

$$Linear(x) = \frac{FOV_x V_x}{N_{lines}} * x \tag{5.1}$$

Here, the linear X-axis waveform input is defined as a line with slope equal to the FOV (mm) scaled bsy a voltage scale factor V (V/mm) divided by the number of lines. On the other hand, the slow Y-axis scan waveform is constant per frame to generate a raster scan pattern. For adaptive-sampling, the slope of the linear X-axis waveform (Eqn. 5.1) is scaled by $v_{dense} = 0.25$ to densely-sample the center of the FOV between X_{start} and X_{end} by a factor of 4. In addition, the slope of the scan waveform is scaled by $v_{sparse} = 1.50$ (calculated based off of v_{dense}) to sparsely-sample the periphery of the frame. Scale factors were chosen to maximize sampling density at the center of the frame while maintaining a wide FOV for tracking as well as a high frame rate for 4D volumetric imaging.

Adaptive-Sampling

$$Dense\ (x) = Linear(x) * v_{dense}, \qquad X_{start} \le x \le X_{end} \tag{5.2}$$

$$Sparse(x) = Linear(x) * v_{sparse}, \qquad x < X_{start}, x > X_{end} \tag{5.3}$$

$$v_{sparse} = \frac{N_{lines} - (X_{end} - X_{start}) * v_{dense}}{N_{lines} - (X_{end} - X_{start})} \tag{5.4}$$

For visualization and CNN detection, acquired SER images were resampled (Fig. 5.3(c)) based on the fast-axis galvanometer position output measured via the galvanometer controller (MachDSP, ScannerMax).

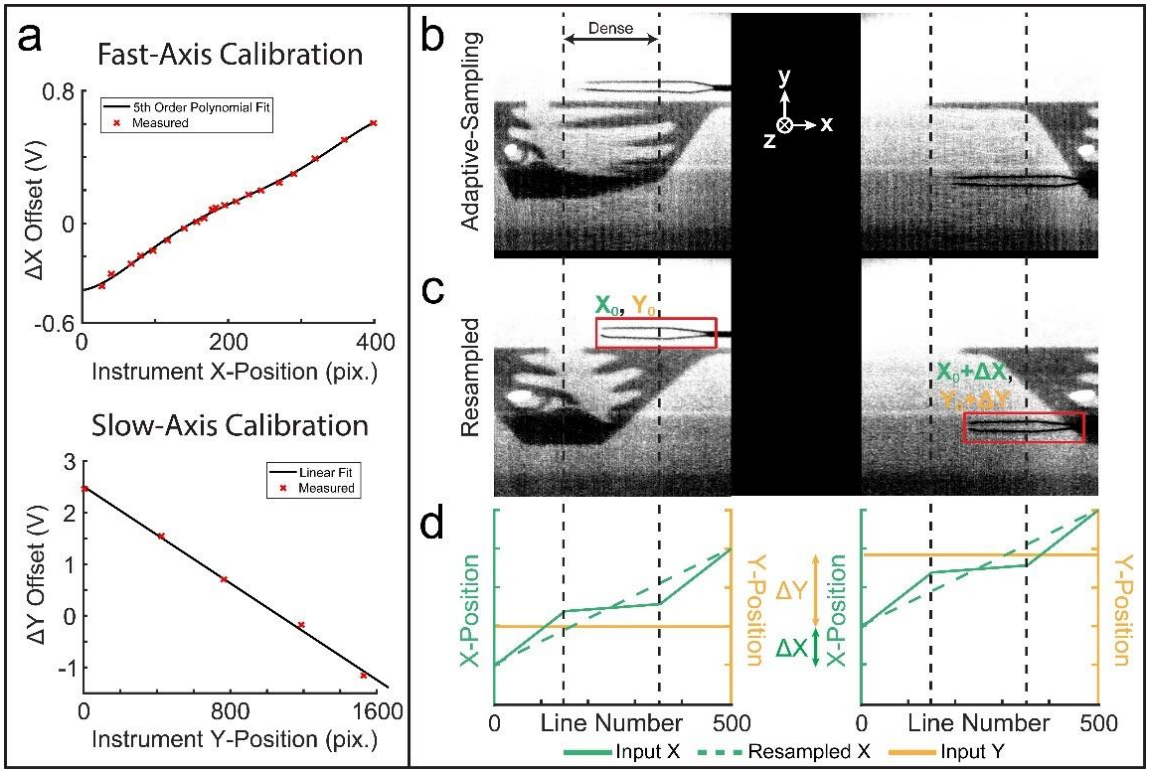

Fig. 5.7. Scan waveform modification calibration. (a) Fast (X) and slow (Y) axis offset calibration. (b) Adaptively-sampled SER images showing dense-sampling of the instrument tip and (c) resampled/linearized images. (d) Input and resampled scan waveforms for images in (b), (c) showing X- and Y-offsets used to center the OCT FOV on the instrument (red) following out-of-plane motion (left images vs. right images).

5.2.3 Experimental Setup

Table 5.4. CNN accuracy experimental parameters

Experiment Number	Depth (Z)	Orientation	Translation Speed (X)
1	0, 3, 6, 9, 12, 15, 18, 21 mm	0°	5 mm/s
2	0, 3, 6, 9 mm	0°	0.25, 1, 2, 4, 6, 8, 10 mm/s
3	0 mm	0, 45, 90, 135, 180°	0.25, 1, 2, 4, 6, 8, 10 mm/s

The SECTR engine was interfaced with an ophthalmic imaging probe placed in a microscope configuration with axial (Z) translation freedom. A pair of 25G ILM forceps were clamped and mounted to a two-axis (XY) motorized translation stage (MLS203, ThorLabs) with 0.1 µm position resolution for precise control of instrument position and speed.

In order to quantify the accuracy of the CNN for basic surgical maneuvers, a series of 3 experiments were performed by varying probe axial/depth (Z) position, instrument orientation, and instrument translation speed (Table 5.1). Instrument speeds were chosen to cover and extend beyond the range of typical ophthalmic surgical maneuver speeds between 0.1 – 0.5 mm/s [291]–[293]. For each set of experimental parameters, SER images of the forceps placed over a paper sample were acquired. For Experiment 1, the imaging probe was translated between 0 mm (in-focus) to 21 mm at increments of 3 mm, which corresponds to the measured Rayleigh range of the system, in order to simulate motion of the instrument out-of-focus (Fig. 5.4(a)). For Experiment 2, both instrument depth and translation speed were varied in order to simulate out-of-plane motion and motion blur. Lastly for Experiment 3, instrument orientation and speed were varied to imitate dynamic movement of the instrument during operation (Fig. 5.4(b)). For each set of parameters, manual annotation of instrument position from tracked SER images (N = 200) were compared to corresponding CNN outputs to determine pixel error and tracking accuracy.

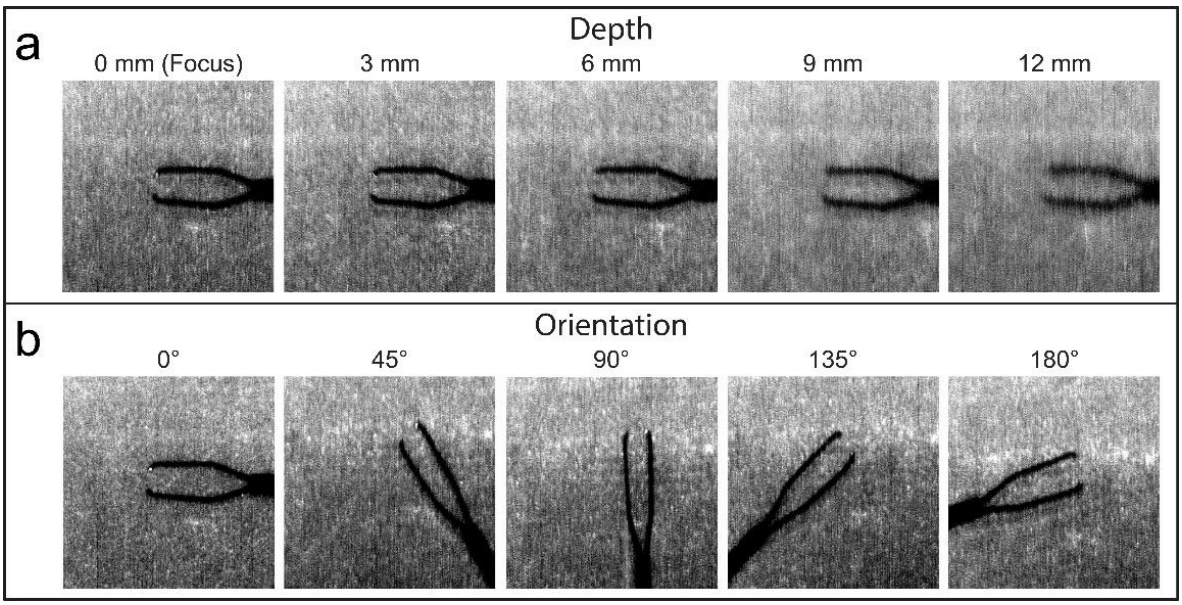

Fig. 5.8. SER images as a function of varying (a) probe depth and (b) instrument orientation.

5.3 Results

SER image resolution was measured using a 1951 United States Air Force test chart to be 44.2 μm with a sampling resolution of 15 μm/pixel. Thus, the minimum expected pixel position error corresponding to the resolution limit can be calculated to be 44.2/15 = 2.95 pixels. For each combination of experimental parameters, position error was calculated by taking the difference between neural network position outputs and manual labels of position (N = 200). A one-sample t-test was used to compare each distribution of calculated errors to the resolution limit of the system. Comparing manual annotations of instrument position to CNN outputs at various axial positions, we are able to achieve resolution-limited tracking accuracy ($p << 1E-7$) between 0 mm – 9 mm, which is beyond the ~7 mm full axial range of our OCT imaging (Fig. 5.5, top). Comparing tracking accuracy in this depth range with varying instrument translation speed, we maintain resolution-limited performance up to velocities of 10 mm/s (Fig. 5.5, middle). Similar performance can also be achieved when varying instrument orientation and speed (Fig. 5.5, bottom). Despite the presence of error extrema and outliers, distribution means were statistically significantly lower than the resolution limit. These results suggest that the CNN is particularly robust to intraoperative variability, including

movement of the instrument in and out-of-focus, high speed maneuvers, and dynamic maneuvers involving rotation and translation of the surgical instrument.

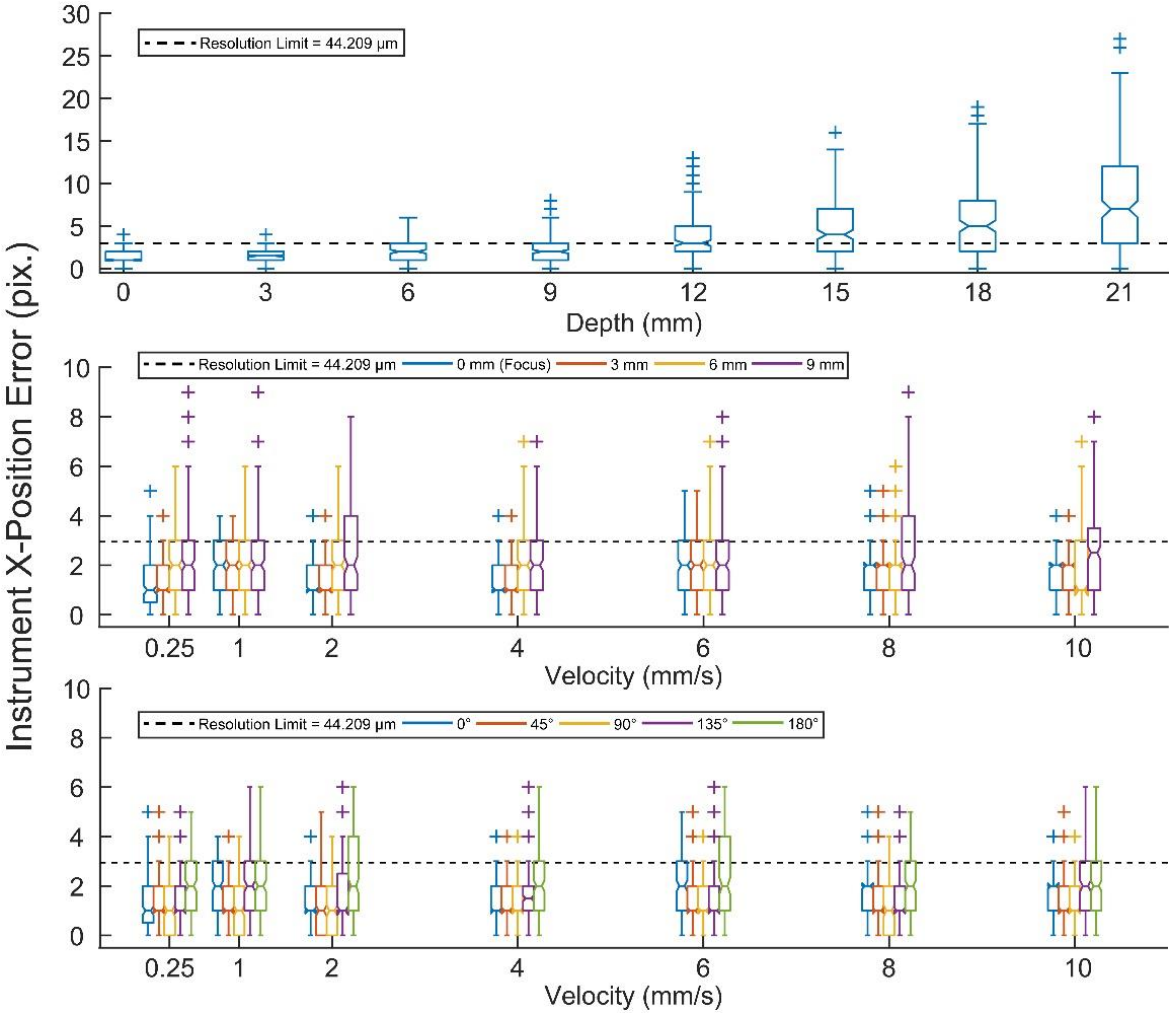

Fig. 5.9. Quantification of CNN accuracy as a function of depth for a fixed orientation and speed (top), depth and speed (middle), and orientation and speed (bottom). Pixel error between CNN and manual outputs are compared to the resolution limit of the system (~2.95 pix.). Box plots span the 25th and 75th percentiles and box waists correspond to distribution means. Box plot whiskers extend to data extrema and outliers are denoted by '+'.

Beyond tracking accuracy, it is also important to continuously center the instrument within the imaging FOV in order to provide 4D visualization of instrument-tissue interactions. For each combination of experimental parameters, the standard deviation of CNN outputs was calculated to determine how precisely the instrument was re-centered despite changes in focus, speed, and

orientation. Comparing CNN instrument position outputs, we are able to localize the instrument at the center of the image within the resolution limit for typical ophthalmic maneuver speeds below 1 mm/s regardless of instrument orientation or depth position (Fig. 5.6). However, a linear trend in deviation from the center of the frame is observable at higher speeds due to update rate limits. Here, we chose to update scan position waveforms per volume (16 Hz) instead of at the CNN output rate (120 Hz) in order to prevent discontinuities in volumetric rendering as well as to maintain anatomical accuracy within each volume. Nevertheless, a minimal deviation of ~15 pix. can be seen even at translation speeds of 10 mm/s, which is beyond the speed of conventional ophthalmic surgical maneuvers.

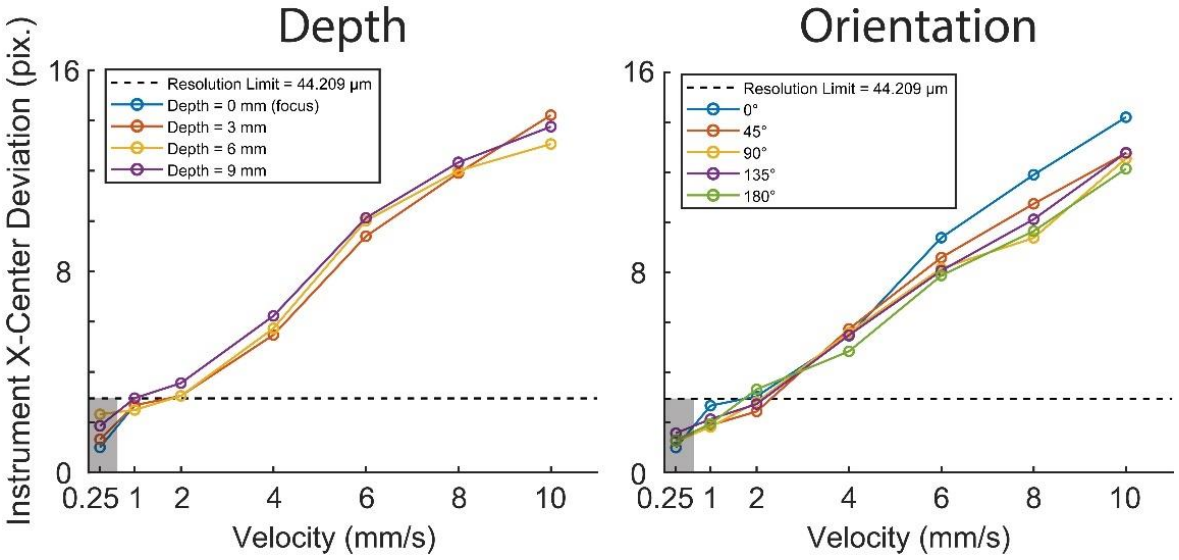

Fig. 5.10. Instrument deviation from center for tracked SER frames using CNN position outputs for changes in depth and speed (left) and orientation and speed (right). Resolution-limited localization of the forceps at the center of the frame is shown for typical ophthalmic surgical maneuver speeds (shaded box).

Finally, we validated our CNN-based tracking method by performing automated instrument-tracking and 4D video-rate imaging of a mock surgical task. Free-hand maneuvers of 25G ILM forceps by an untrained volunteer were used to evaluate CNN tracking performance in the presence of physiological tremors. In particular, a metallic ring was moved between 4 phantom quadrants of

varying height (0 mm, 1 mm, 2 mm, 3 mm). Additional features, such as holes and a scale bar (3 mm increment), were included in order to better visualize lateral and axial changes as the instrument moves. Volumetric imaging was performed using 2560 (Z) x 500 (X) x 50 (Y) pix. (pixels per line x lines per frame x frames per volume) for a frame rate of 800 Hz for *en face* SER and cross-sectional OCT B-scans and volume rate of 16 Hz for 3D OCT. CNN detection of forceps from SER images was performed simultaneously at a rate of 120 Hz. SER images were acquired over a 25 mm (Y) x 7 mm (X) FOV and tracking was performed over a maximum FOV of 25 mm x 25 mm. Following the acquisition, standard OCT post-processing methods were used to generate images from spectral data and a 4D rendering of OCT data was produced using 3D Slicer [294]. Despite lateral movement across the entire sample, changes in depth/focus, opening and closing of the forceps tip, as well as presence of specular reflections from the metallic ring, the forceps remain localized in the OCT FOV (Fig. 5.7, Visualization 2).

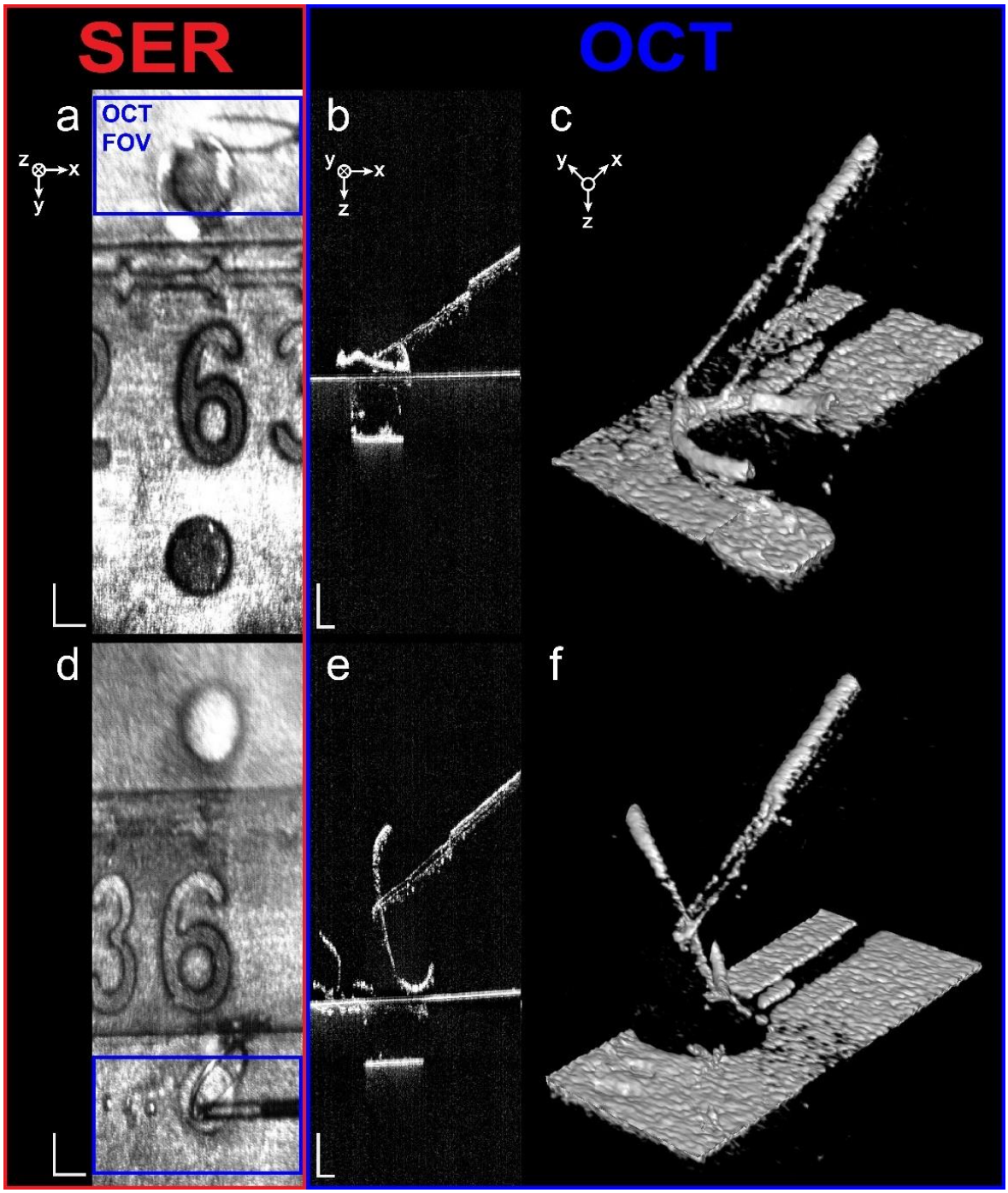

Fig. 5.11. Automated instrument-tracking in a 4-quadrant phantom. (a) SER image of 25G ILM forceps manipulating a metallic ring and (b) corresponding OCT volume B-scan maximum intensity projection and (c) 4D rendering. (d) SER image following out-of-plane motion and translation of the instrument. (e),(f) Localization of the instrument in the OCT FOV despite lateral movement and axial position change. Scale bar = 1 mm (a),(d) and 0.5 mm (b),(e). See Visualization 2.

5.4 Discussion and Summary

Ophthalmic microsurgery is conventionally performed under a surgical microscope, which precludes visualization of subsurface features and underlying instrument-tissue interactions. iOCT is an emerging technology that provides depth-resolved visualization of surgical maneuvers but is currently limited by slow scans speeds and lack of automated instrument-tracking that necessitates manual adjustment of the static imaging FOV. Here, we propose an automated instrument-tracking method that takes advantage of a high-speed SECTR system to simultaneously acquire *en face* SER and cross-sectional OCT images. Co-registration between the two imaging modalities allows for dynamic updates of OCT scan position based on instrument position detected from SER images. Using a GPU-accelerated CNN, we are able detect surgical instrument positions at over 120 Hz with resolution-limited accuracy despite changes in focus, orientation, and speed. In addition, the proposed method has significant advantages over previously-reported OCT-based, color-based, and gradient-based detection methods by providing widefield lateral tracking in the presence of instrument deformation, soft-tissue movement, mechanical manipulation of the eye, and artifacts such as specular reflections. Furthermore, our method enables tracking for both anterior and posterior segment operations due to the network's insensitivity to distortions and aberrations induced by the optical system and the optics of the eye. We demonstrated the efficacy of our method by performing automated instrument-tracking and 4D video-rate imaging of a mock surgical task in a phantom.

Currently, the main limitation of our method is the update rate, which occurs once per volume in order to prevent intravolume updates that would degrade 4D visualization. As a result, we have a linear increase in instrument position deviation from the center of each image with increasing instrument velocities. However, ophthalmic microsurgery requires delicate manipulation of tissue, and instrument maneuver speeds are typically between 0.1 – 0.5 mm/s. Within this speed range, our method achieves high tracking accuracy and localization of the instrument. In addition, we show that our method is robust to extreme changes in speed (0.25 – 10 mm/s) and defocus (0 mm – 9 mm) that are beyond traditional use cases. We also account for changes in instrument orientation which may

occur during manipulation of tissue as well as from differences in surgeon preference (left-handed vs. right-handed). At higher speeds beyond ophthalmic surgical use cases, it is also possible to use extrapolation methods, such as Kalman filtering, to achieve better localization of the surgical instrument despite limited update rates.

Furthermore, we believe the proposed method can be extended for the identification and tracking of multiple instruments which are often present simultaneously in the surgical field. The implemented CNN is capable of predicting instrument positions across multiple classes at once and can be trained to detect a variety of ophthalmic surgical tools including forceps, picks, loops, membrane scrapers, and light pipes. In addition, the existing 25G ILM forceps model can potentially be extended to facilitate training through transfer learning to generate a robust model for multiple instruments [295], [296]. By using an open-source network, we also eliminate the need for extensive hyperparameter tuning and optimization that is typical for many CNN implementations and, thus, broaden the applicability of our automated instrument-tracking framework. Similarly, we can extend our adaptive-sampling protocol to be able to target individual surgical instruments as specified by the surgeon as well as to switch between multiple instruments by leveraging multi-class detection outputs.

In addition, our technology can be directly integrated into the surgical microscope and potentially used for 4D *in vivo* imaging and automated instrument-tracking [297], [298]. We believe our method ultimately enables intraoperative guidance for ophthalmic microsurgery and will facilitate the adoption of iOCT technology. Furthermore, our method can benefit iOCT-guided surgery by lowering the learning curve for surgeons and allowing them to perform an operation normally in comparison to the use of commercial iOCT systems, which require manual tracking and alignment of the static OCT FOV to ROIs. SECTR-based tracking can also be extended beyond ophthalmic applications for use in fields such as dermatology, where imaging power and speed can be significantly increased for enhanced 4D tracking and visualization [299], [300].

CHAPTER 6

Automated instrument-tracking and 4D video-rate visualization of ophthalmic surgical maneuvers in *ex vivo* porcine eyes

The following chapter contains content that is adapted from E. M. Tang, M. T. El-Haddad, S. N. Patel, and Y. K. Tao, "Automated instrument-tracking for 4D video-rate imaging of ophthalmic surgical maneuvers," Biomedical Optics Express 13, 1471-1484 (2022) [257].

The following chapter contains content from E. M. Tang, M. T. El-Haddad, S. N. Patel, and Y. K. Tao, "Automated instrument-tracking and 4D video-rate visualization of ophthalmic surgical maneuvers in *ex vivo* porcine eyes," that is currently in preparation.

6.1 Introduction

The development of automated instrument-tracking techniques is crucial for successful and efficient image-guided surgery and has potential benefits for enhancing feedback in a number of fields, including ophthalmic microsurgery and minimally-invasive surgery [301]–[303]. In particular, these operations present several challenges, including limited haptic feedback and reliance on surgical microscope or endoscope feeds for visualization of complex surgical maneuvers [269]. These feeds often suffer from illumination variability and specular artifacts that prevent the use of traditional instrument-tracking methods, which include color and geometry-based techniques [304]. Furthermore, real-time 4D visualization of ophthalmic surgical maneuvers requires robust and high-speed tracking that cannot be achieved by conventional image-processing-based algorithms [185]. Alternate solutions include the use of fiducial markers, which require modification of the surgical instrument and thus raise concerns in terms of cost, biocompatibility, sterility, and ergonomics. Additionally, optical tracking and stereo-vision-based tracking methods suffer from tracking errors that vary as a function of fiducial marker distance from the instrument tip as well as changes in

instrument orientation [305]. These factors are often confounded by optical aberrations due to radial or barrel distortion of lenses used in camera-based systems as well as ocular distortion due to aberrations and motion in ophthalmic imaging applications [306]–[308].

In addition, ophthalmic microsurgery involves complex maneuvers that involve the use of a variety of surgical instruments designed for precise manipulation of both anterior and posterior ocular tissues [309]. Conventional instrument-tracking methods relying on instrument color, geometry, or gradient-based edge detection are often specifically designed to track a single surgical instrument from endoscopic or microscopic video feeds and tend to suffer for *in vivo* applications and for multi-instrument tracking [310]. Thus, these methods are impractical for use in ophthalmic surgery, which involves a range of surgical tools of different shape, size, and visual properties that also varies with respect to use for anterior or posterior segment operations. To date, a limited number of approaches have been explored for tracking multiple surgical instruments. Multi-instrument tracking methods relying on visual feedback are capable of detecting multiple instruments in a field simultaneously and can provide valuable collision feedback for safety [311]. However, these methods suffer from video feed artifacts, such as nonuniform illumination, specular reflections, and occlusions. In addition, these methods lack specificity for identifying and tracking specific instruments within the surgical field.

In order to address these limitations, our group has developed a multimodal ophthalmic imaging system for simultaneous *en face* reflectance and cross-sectional OCT imaging [122], [173]. Automated-instrument tracking is accomplished using deep-learning-based detection of instrument position from *en face* spectrally encoded reflectometry (SER) images. Inherent spatio-temporal co-registration between SER and OCT images enables dynamic 3D tracking of surgical instruments and automatic localization for 4D video-rate visualization of ophthalmic surgical maneuvers. We have previously validated the performance of our automated instrument-tracking method in a paper sample and phantom and have demonstrated resolution-limited detection accuracy for different instrument speeds, orientations, and depths [257]. Here, we extend our CNN-based tracking method to detect multiple surgical instruments for video-rate 4D visualization of ophthalmic maneuvers in the anterior

segment of *ex vivo* porcine eyes. Compared to conventional tracking methods, deep-learning-based approaches have demonstrated a higher degree of specificity that allows for classification of multiple surgical instruments [312], [313]. We demonstrate robust localization of three surgical instruments despite the presence of nonuniform illumination, reflection artifacts, tissue deformation, and changes in instrument orientation in *ex vivo* SER images. We believe our proposed method can be extended for any number of surgical instruments and can be used for automated instrument-tracking and 4D visualization of both anterior and posterior segment ophthalmic procedures.

6.2 Methods

6.2.1 *Ex vivo* SECTR Imaging

Ex vivo ophthalmic imaging was performed using a custom-built spectrally encoded coherence tomography and reflectometry (SECTR) engine [173]. The system utilizes a buffered 400 kHz swept-source laser centered at 1060 nm with a bandwidth of 100 nm. Source laser power was split between SER and OCT imaging. A custom ophthalmic imaging probe was interfaced with the SECTR engine and used to colinearly combine and relay SER and OCT illumination beams to the sample (Fig. 6.1) [122]. A high-speed digitizer (ATS9373, AlazarTech) was used to simultaneously digitize detected SER and OCT signals at 2 GS/s and stream acquired data to a disk. Although *ex vivo* porcine eyes (Sierra for Medical Science) were acquired and imaged for demonstration, SER and OCT power were optimized to fall within ANSI Z80.36 safety limits for *in vivo* human ophthalmic imaging. OCT and SER powers at the pupil were measured to be 1.3 mW and 4.2 mW, respectively, for a total power of 5.5 mW at the sample. In addition, a dichroic window in the SECTR probe was used to capture white-light images of the sample to simulate surgical microscope visualization. A light pipe (Alcon) provided external illumination and a CMOS camera (Blackfly BFLY-PGE-50S5C, Point Grey Research) was used to capture frames at 16 Hz (2448 x 2048 pix.).

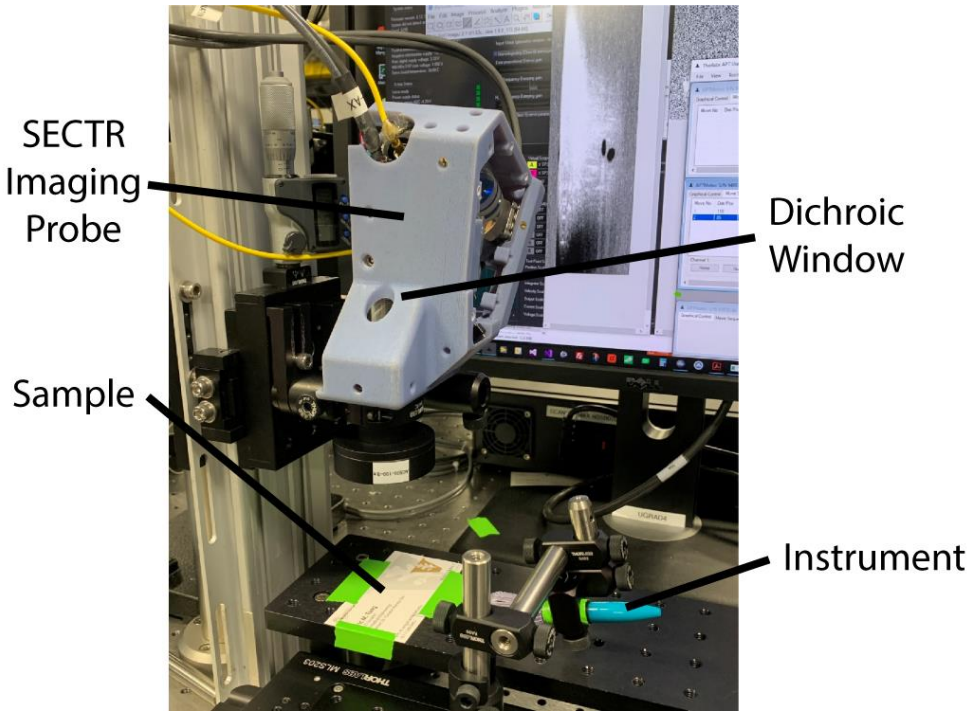

Fig. 6.1. Experimental setup. The SECTR imaging probe was placed in a microscope configuration for visualization of ophthalmic surgical maneuvers in an *ex vivo* porcine eye sample.

6.2.2 Surgical Microscope Objective Integration

In our previous tracking accuracy validation study, SECTR imaging was performed at the intermediate image plane of a handheld probe mounted in a microscope configuration (Fig. 6.1). However, one limitation to the translation of SECTR and other iOCT imaging systems is integration with the optics of a surgical microscope. OCT imaging is often performed in the near infrared regime at wavelengths between 800-1300 nm, while surgical microscopes operate using white-light illumination. The design of stereomicroscopes, therefore, is often optimized and corrected for visible wavelengths of light and ultimately degrade OCT image quality due to wavelength-dependent optical aberrations when imaging through the microscope objective lens [128]. Furthermore, commercial objective lenses are often provided as 'black-box' models that inhibit robust optical design and aberration compensation. Our lab has developed a non-contact lens characterization method to characterize the physical and optical properties of a commercial Zeiss VISU 200 surgical microscope objective lens [314]. Lens characterization has enabled optimization of microscope integrated

intraoperative SECTR and evaluation of its performance through the objective lens of a surgical microscope, which is critical for future *in vivo* application [298]. Here, we similarly adjust our initial experimental setup by modifying handheld probe scan and relay lenses for the inclusion of a Zeiss VISU 200 objective lens (Fig. 6.2). As a result, tracking performance can be assessed in a more practical scenario where SECTR optics are integrated with those of a commercial surgical microscope. *Ex vivo* porcine eye imaging and automated-instrument tracking was performed at the focus of the surgical microscope objective lens, which allowed for direct comparison of tracking accuracy to that of our previous study conducted in paper phantoms.

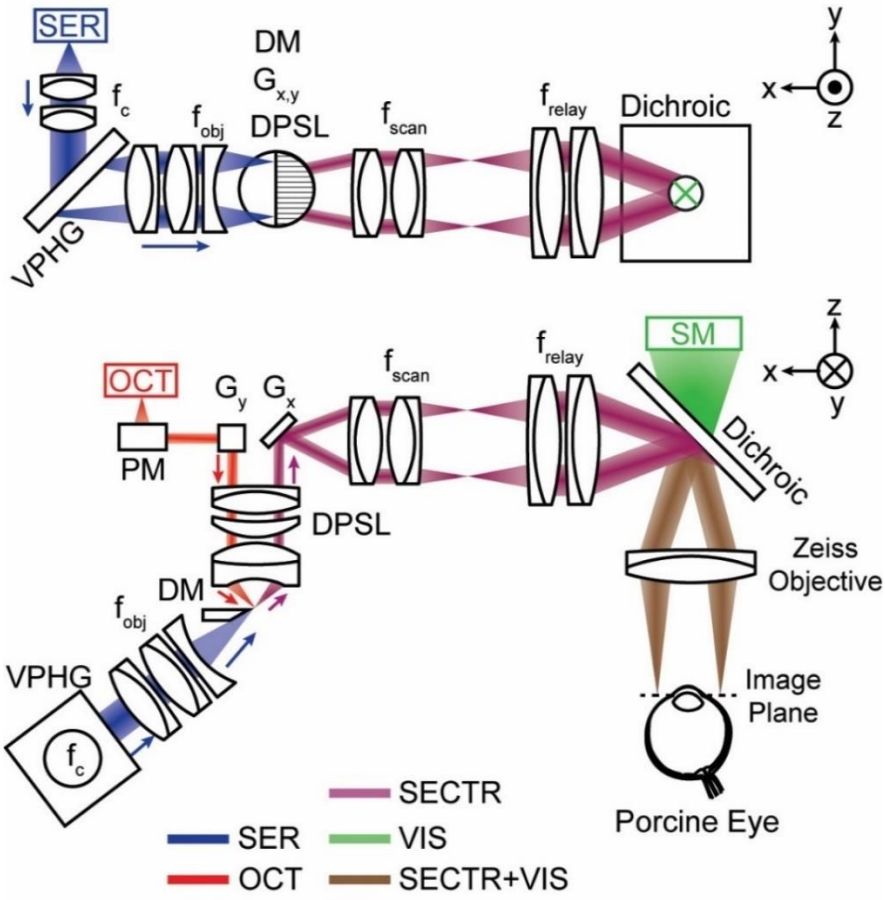

Fig. 6.2. Modified SECTR optical configuration for imaging of the anterior segment of *ex vivo* porcine eyes. Handheld probe scan (f_{scan}) and relay (f_{relay}) lenses were modified and optimized for the incorporation of a Zeiss VISU 200 surgical microscope objective lens. Figure adapted with permission from [298].

6.2.3 Multi-Instrument Tracking

Rapid developments in deep neural networks have accelerated the generation of network architectures capable of multi-class detection and classification. These networks have been applied for a wide variety of applications ranging from computer vision to disease diagnosis [315]. Here, we leverage the versatility of current-generation object detectors by extending our previously described open-source neural network (YOLOv4) for multi-class detection and multi-instrument tracking [289]. Recent studies have evaluated the performance of YOLOv4 and have demonstrated accurate tracking of multiple surgical instruments typically used in minimally invasive surgery [316]. In addition, YOLOv4 has shown superior performance compared to other similar models for more complex applications, such as automated detection of artifacts in endoscopic images and combinatorial sorting of cells in microdroplets [317], [318].

Our previous implementation of YOLOv4 focused on single-class detection of 25G internal limiting membrane forceps for determination of tracking accuracy and initial automated instrument-tracking validation. In order to achieve broader utility for ophthalmic surgical instrument detection and tracking, we have modified our network configuration for the detection of three unique classes of instruments: microsurgical knives (V-lance), forceps, and cannulas/needles. These instruments are commonly used for anterior segment operation in order to create incisions in the cornea, to peel or grasp ocular tissues, and to inject air or contrast agents into the anterior chamber, respectively. Initial demonstration of *ex vivo* instrument-tracking is performed for detection of these three instrument classes, but the network can easily be extended to any number of instrument classes for more complex surgical procedures as well as to account for smaller gauge instruments used in posterior segment surgery.

6.2.4 Multi-Channel Training

We have previously demonstrated automated instrument-tracking with resolution-limited tracking accuracy in a paper sample. However, similar to surgical microscope feeds, SER imaging performance tends to suffer in *ex vivo* and *in vivo* applications due to the presence of image artifacts,

such as specular reflections and shadowing (Fig. 6.3). These artifacts arise from detector or bit-depth saturation, background subtraction, and ocular structures such as the cornea tear film. In addition, the appearance of these artifacts changes dynamically throughout imaging due to beam-scanning, varying field positions resulting from tracking offsets, and bulk motion of the eye by both the operator and patient. These factors are confounded by changes in instrument orientation both in and out-of-plane, which result in varying reflectivity profiles and contrast. Although deep-learning-based instrument-detection is more robust to these variables than conventional tracking methods, optimization of network inputs can potentially improve training and detection performance for *ex vivo* application.

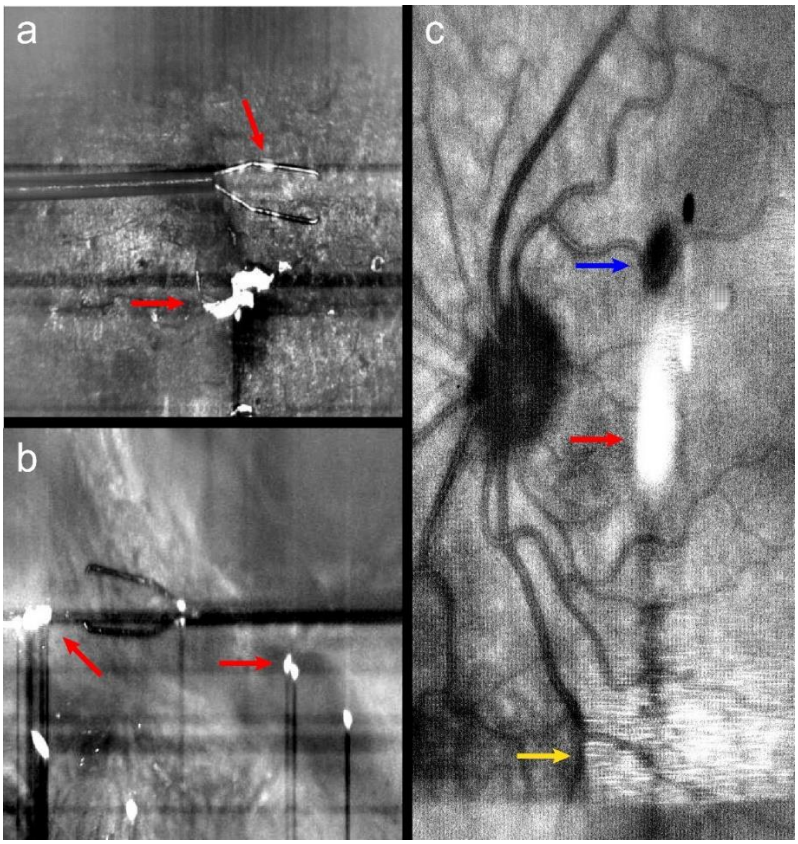

Fig. 6.3. SER images acquired in a (a) paper sample (b) *ex vivo* bovine eye and (c) *in vivo* human eye showing imaging artifacts such as specular reflections and shadowing due to saturation (red), DC artifacts (blue), and cornea tear film reflections (yellow).

Data augmentation is widely used for improving CNN performance and robustness by altering and inflating training data sets while preserving labels [319], [320]. Common augmentation methods

include geometric transformations (flipping, rotating, translating, cropping) and photometric (color) transformations. We have previously explored geometric augmentation of instrument data by flipping and rotating each image, which has improved network performance for varying instrument orientations. However, SER images used for training were grayscale (single channel), whereas CNN-based object detectors are often designed to take RGB (three channel: red, green, blue) or BGR input images for detection. Color images can then be decomposed into their individual color channels for multi-channel estimation of object position. Comparing the performance of CNNs with varying number of channel inputs, studies have demonstrated a classification improvement of 3% using color images over grayscale images on large-scale image databases [321], [322]. For ophthalmic applications, CNN-based diagnosis has benefitted from the use of color fundus images due to channel encoding of various wavelength-dependent morphological and functional features, such as the inner retina (blue), blood vessels (green), and outer retina/choroid (red) [323]. Furthermore, studies have shown that color channels can be used to encode independent information via concatenation of multiple complementary images. For example, the fusion of spatial, temporal, and thermal information in a single BGR image has been demonstrated and can be used to improve both object detection accuracy and computational efficiency [324].

Here, we leverage photometric augmentation techniques in order to encode SER spatio-temporal information in a single BGR image for CNN training and detection (Fig. 6.4). Individual images are concatenated in order to encode raw SER images (blue), 5-average SER images (green), and 5-variance SER images (red). Averaging of SER images reduces background speckle noise and also encodes both spatial information of the instrument and temporal information of instrument position across multiple volumes. Similarly, SER image variance across multiple volumes encodes instrument motion (high variance) relative to stationary background tissue (low variance). Data fusion was accomplished by modifying the instrument-tracking thread in the SECTR acquisition software. Raw SER images were copied and continuously stored in a first-in-first-out (FIFO) 5-frame buffer. A running 5-frame average and 5-frame variance were calculated upon acquisition of a new raw SER

frame. The most recently acquired frame in the buffer was used as the blue channel raw SER image input and was concatenated with the corresponding average and variance of frames in the buffer to generate a single BGR image. The BGR image height was then downsampled by a factor of 4 via spectral averaging to match the network height before being used as an input for training or detection (Fig. 6.4(b)).

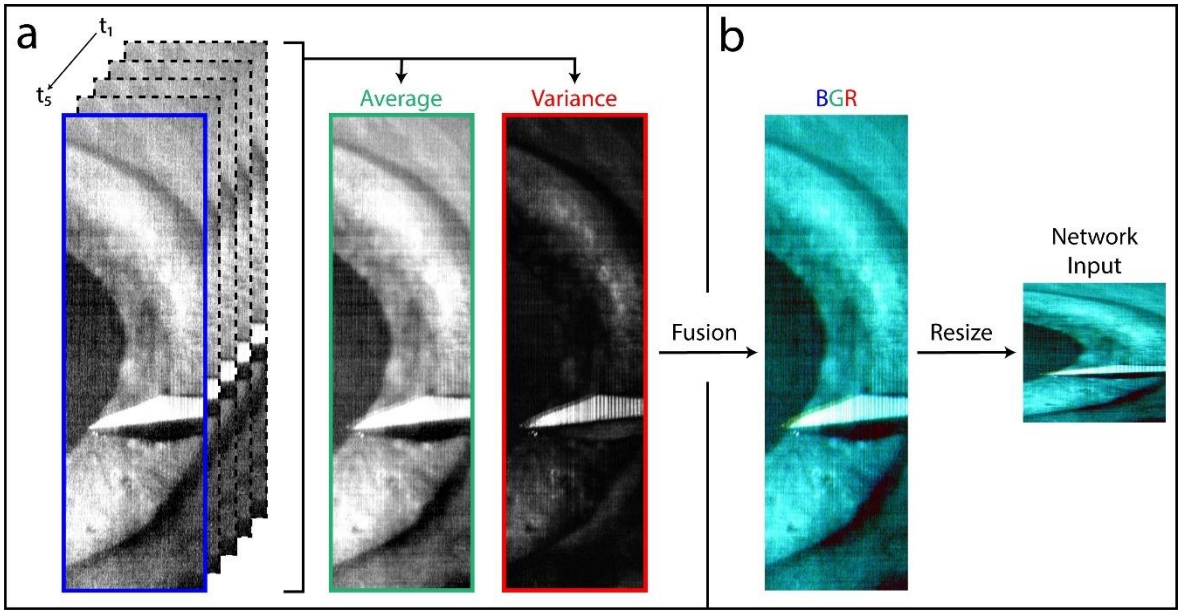

Fig. 6.4. Multi-channel SER fusion. (a) A series of 5 SER images is stored and used to encode information into a single BGR image: Blue = last raw SER image in the stored time series; Green = average of 5 SER images in the series; Red = variance of 5 SER images in the series. (b) Concatenation of data shown in (a) creates a single BGR image. The image is resized (1664 x 500 → 416 x 500, spectral x lateral pix.) via spectral averaging before being input into the CNN.

SECTR imaging was performed in *ex vivo* porcine eyes and corresponding instruments were manipulated to simulate mock anterior segment surgical maneuvers (e.g. corneal incision, corneal scraping, and anterior chamber injection). GPU-accelerated CNN [289] training was accomplished using 4031 BGR SER images for classification of V-lances (N = 2166), anterior segment forceps (N = 1380), and blunt cannulas and 30G hypodermic needles (N = 485). For simplicity, manual-labelling was accomplished by annotating the blue channel of each image corresponding to the raw SER image channel. In addition, data augmentation was performed by flipping each image horizontally to increase robustness depending on operator handedness. The augmented data was then split between

training (80%) and validation (20%) sets. Training was performed on a computer with an Intel i9-10900X CPU, an NVIDIA GeForce RTX 2080 Ti GPU and 64GB RAM. Overall, CNN training was run for 200,000 epochs over the course of 12 hours.

6.3 Results

6.3.1 CNN Training Performance

$$\textbf{Intersection over union (IoU)} = \frac{area\ of\ overlap}{area\ of\ union} \tag{6.1}$$

$$\textbf{Precision} = \frac{true\ positive}{true\ positive + false\ positive} \tag{6.2}$$

$$\textbf{Recall} = \frac{true\ positive}{true\ positive + false\ negative} \tag{6.3}$$

$$\textbf{F1-score} = \frac{2 * Recall * Precision}{Recall + Precision} \tag{6.4}$$

In order to determine the efficacy and feasibility of multi-instrument, multi-channel CNN training, we evaluated our trained model using several conventional metrics for quantifying CNN performance. For object detection, there exists a predicted bounding box by the CNN as well as a ground truth bounding box that is determined by manual labelling of the SER images. An intersection over union (IoU) can then be calculated by finding the area of overlap between the prediction and ground truth and dividing that value by the area of the union of both (Eqn 6.1, Fig 6.5). Based on an IoU threshold (e.g. IoU > 50%), a precision metric (or positive predictive value) can be calculated for a specific class by finding the number of images that correctly classify the instrument (true positive) and dividing that value by the total number of images identified to contain that instrument (total positive). Similarly, recall (or sensitivity) can be calculated by finding the number of images that correctly identify the instrument (true positive) and dividing that value by the total number of images that have the specific instrument (both correctly identified and falsely rejected). For a given IoU threshold, a precision-recall curve can be generated similar to a receiver operating characteristic curve. Average precision (AP) can then be calculated by taking the area under the precision-recall

curve and mean average precision (mAP) can be quantified by averaging AP values at a specific IoU threshold across all classes.

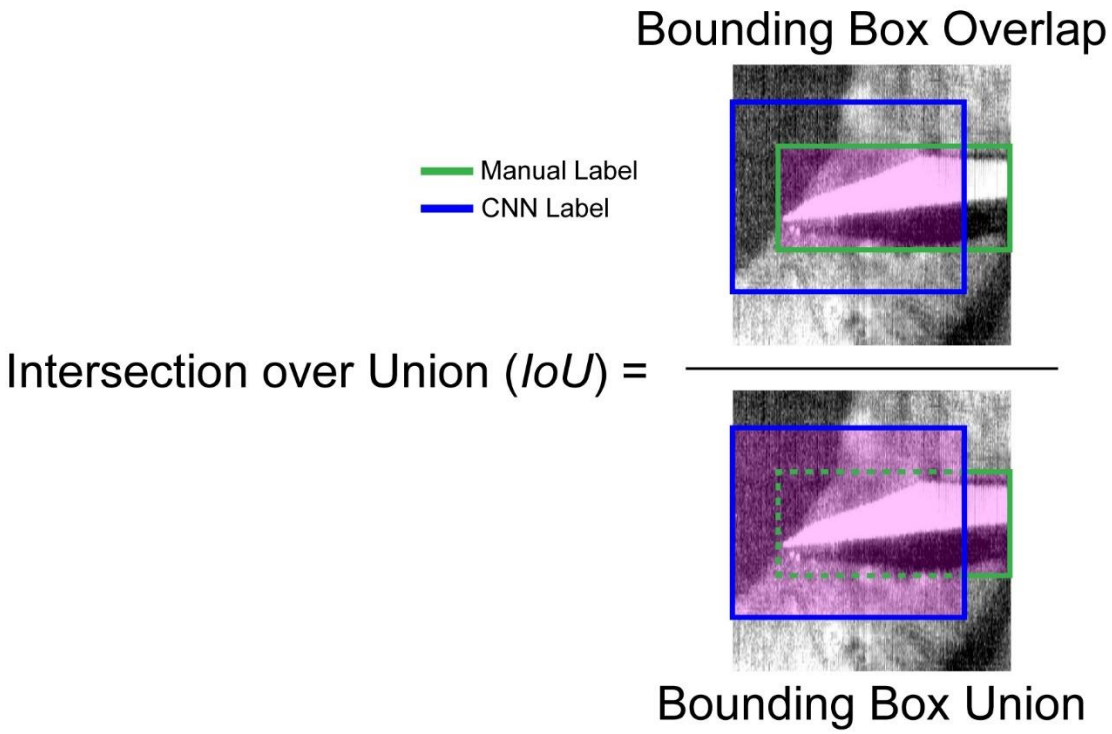

Fig. 6.5. Intersection over union (IoU) is calculated by taking the area of bounding box overlap between manual (green) and CNN labels (blue) and dividing that value by the union of the two.

Thus, these metrics were used to quantify the performance of the CNN in correctly identifying three classes of ophthalmic surgical instruments (V-lance, forceps, and cannula/needle). After data augmentation, 1612 images were included for validation during training. Of the validation set, 1602 images contained unique truth counts corresponding to a single surgical instrument class, while the remaining 10 images did not contain an instrument (e.g. sample background). Post hoc validation of model performance shows high AP > 99.9% using an IoU threshold of 0.50 (Table 6.1). Across all classes, a mAP value of 99.98% was achieved. Across all validation images, 1547 true positive classifications (95.97%), 10 false negative classifications (0.62%), and 45 false positive classifications (2.80%) were made. Therefore, we demonstrate that we are able to achieve high instrument classification accuracy with 97% precision (Eqn. 6.2) and 99% recall or sensitivity (Eqn

6.3), corresponding to an F1-score of 98% (Eqn 6.4).

Table 6.1. CNN training performance quantified post hoc using the validation set (N = 1612).

Class	True Positive	False Positive	Average Precision (AP)
V-lance	817	26	99.99%
Forceps	536	7	99.99%
Cannula/Needle	194	12	99.95%
Total	1547	45	**mAP** = 99.98%

6.3.2 CNN Detection Latency

Our previous implementation of automated-instrument tracking enabled high speed tracking at over 120 Hz. However, in order to improve model robustness for *ex vivo* tracking, we have implemented multi-channel image detection by fusing raw SER images with average and variance images (Fig. 6.6). Initial image processing follows the prior implementation and includes resampling of raw adaptively-sampled images as well as background subtraction. Previously, raw SER images were then spectrally downsampled by a factor of 2 without averaging to reduce image size and reduce inference time when being subsequently passed through the CNN (Fig. 6.6, dashed arrows). Here, we take advantage of the high detection speed to spectrally average raw SER images by a factor of 4 and therefore potentially reduce noise and improve image quality along this dimension. The resized image is then passed to the 5-frame FIFO buffer and replaces the oldest image before an average and variance image are calculated. Raw, average, and variance images are then fused to create a three-channel BGR image before being passed to the CNN for detection. Spectral averaging and calculation of average and variance images presents additional computational overhead compared to the previous implementation, where raw SER images were fed directly to the network following resizing.

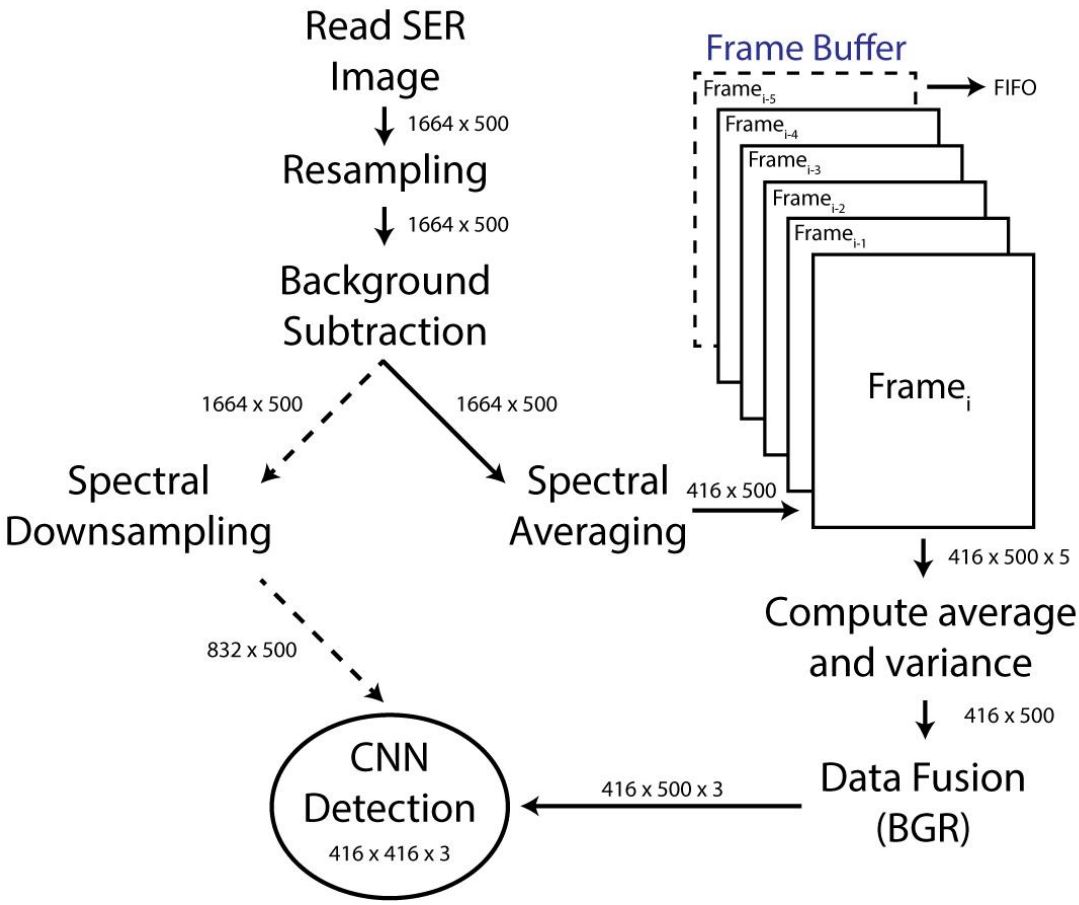

Fig. 6.6. Instrument-tracking thread framework comparing current (solid arrow) and previous (dashed arrow) software implementations. Image dimensions in pixels after each processing step are indicated (spectral x lateral x number of channels) over corresponding arrows.

The total latency for the current instrument-tracking thread pipeline (including pre-processing time and CNN detection) was measured to be approximately 43.7 ms (23 Hz) compared to 8.25 ms (120 Hz) with the previous implementation. Despite the increase in latency and reduction in tracking speed, automated instrument-tracking is ultimately fundamentally limited by volumetric imaging rates. As we have previously discussed, scan waveform update rates for tracking are synced with volumetric imaging rates in order to prevent intravolume updates that would lead to discontinuities and thus affect anatomical accuracy of 4D rendering. Therefore, automated instrument-tracking with detection at 23 Hz is sufficient for smooth 4D visualization of volumetric OCT data, which requires updates rates of 16-20 Hz. Furthermore, our modified implementation takes advantage of multi-

channel detection to potentially improve network performance and tracking accuracy without sacrificing update speeds.

6.3.3 Video-rate 4D *Ex vivo* Tracking

Finally, we validated our modified automated instrument-tracking method for 4D video-rate imaging of mock surgical maneuvers in the anterior segment of *ex vivo* porcine eyes. Free-hand maneuvers of three ophthalmic instruments (V-lance, forceps, and 30G hypodermic needle) were performed by an untrained volunteer in order to assess CNN tracking performance in the presence of several confounding factors, including physiological tremor and artifacts arising from *ex vivo* imaging. Specific tasks were performed to simulate typical ophthalmic surgical maneuvers: 1) the V-lance was moved across the cornea in order to demonstrate initial widefield tracking, 2) the V-lance was used to scrape the apex of the cornea to simulate collection of cells or removal of debris from the corneal surface, 3) the V-lance was used to make an incision in the cornea to simulate anterior segment operation requiring access to the anterior chamber, 4) the V-lance was removed and forceps were introduced in order to pull on corneal tissue and further open the previous incision, 5) the forceps were removed and a needle was introduced and inserted into the incision to simulate injection of air or contrast agents into the anterior chamber.

Visualization of these maneuvers was accomplished using both white-light and SECTR imaging. White-light imaging was achieved simultaneously through a dichroic window of our SECTR imaging probe using a Point Grey CMOS camera operating at a 16 Hz frame rate and a light pipe was used to provide external illumination. SECTR imaging was performed using a modified imaging probe integrated with a Zeiss VISU 200 objective lens for anterior segment imaging. Image acquisition was performed at a frame rate of 800 Hz and volume rate of 16 Hz. *En face* SER and cross-sectional OCT images were simultaneously acquired and sampled at 1664 x 500 pix. (spectral x lateral) and 1664 x 500 x 50 pix. (pixels per line x lines per frame x frames per volume), respectively. Real-time 2D display of SER and OCT images was used for additional guidance of surgical maneuvers. Raw binary SER and OCT data were streamed to a disk and conventional post-processing methods were used to

generate SER (bit conversion, normalization) and OCT (spectral reshaping, dispersion compensation, Fourier transform, bit conversion, normalization) images. 3D/4D visualization of processed OCT data was then accomplished using 3D Slicer [294]. Corresponding white-light, SER, and 4D OCT renderings show localization of the V-lance, anterior segment forceps, and 30G hypodermic needle in a single continuous acquisition despite out-of-plane motion, interactions with underlying corneal tissue, and the presence of field-varying reflection artifacts on SER.

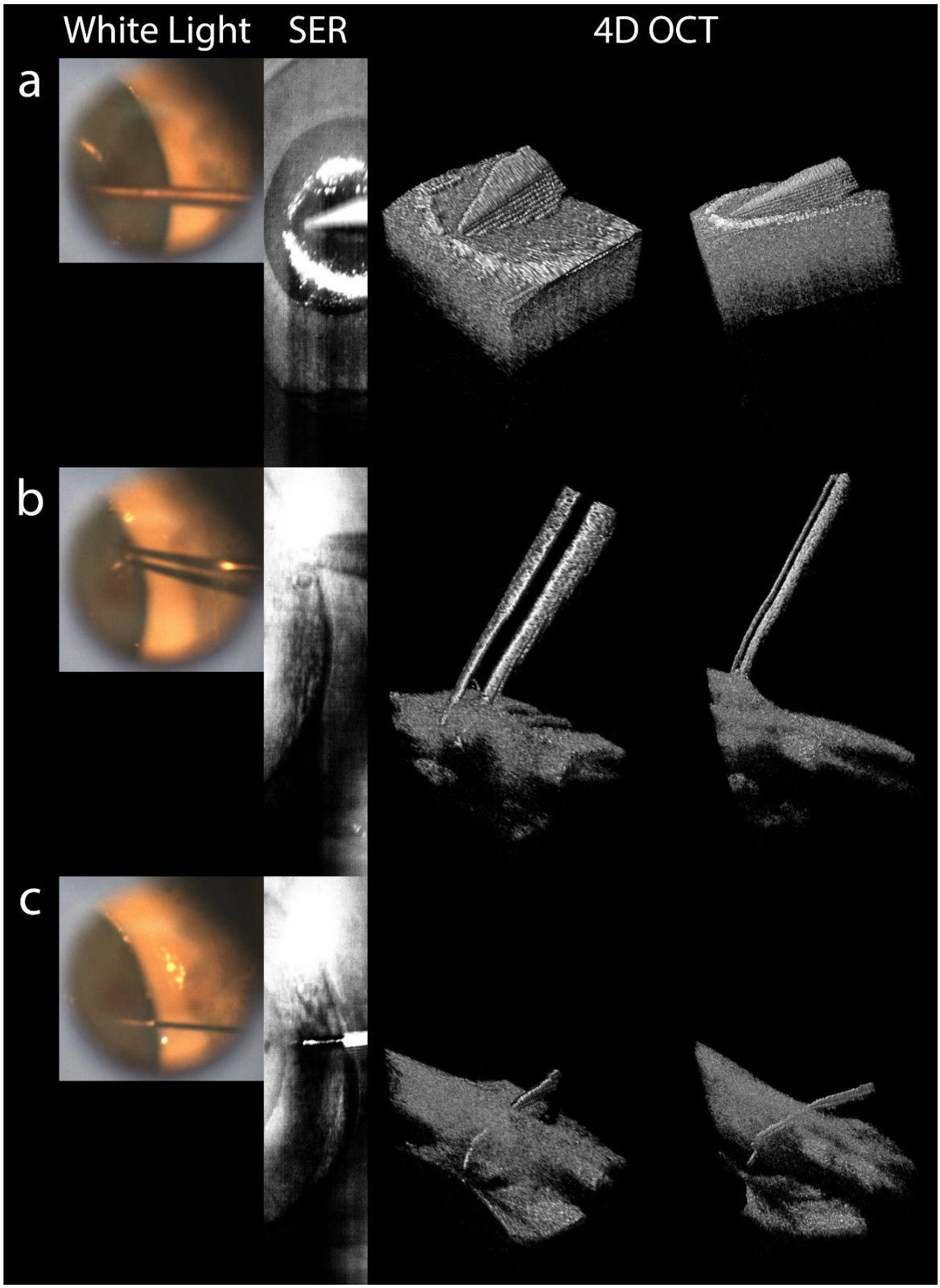

Fig. 6.7. Automated instrument-tracking and video-rate 4D imaging in *ex vivo* porcine eyes. Multi-instrument tracking was demonstrated using (a) V-lance, (b) forceps and (c) a 30G hypodermic needle.

6.4 Discussion

Ophthalmic microsurgery is extremely complex and requires manipulation of fine ocular microstructures. However, these surgeries are conventionally performed under white-light stereomicroscopes, which suffer from nonuniform illumination and reflection artifacts and ultimately lack depth-resolved visualization of ocular tissues. We have previously demonstrated a deep-learning-based tracking method for detection and localization of ophthalmic surgical instruments for 4D video-rate imaging of surgical maneuvers. In particular, a high-speed SECTR system is used to simultaneously generate *en face* SER and cross-sectional OCT images. The co-registration between these two modalities allows for the use of a CNN for rapid detection of surgical instrument position from SER images and subsequent scan waveform modification for localization of the OCT FOV around the instrument. Here, we optimize our tracking framework to improve its applicability for microscope-integrated tracking in *ex vivo* eye models. We integrate our high-speed SECTR system with the objective lens of a surgical microscope in order to evaluate tracking performance through visible-light optimized lenses, which inherently degrade near-infrared imaging. In addition, we incorporate multi-instrument and multi-channel detection that is capable of achieving 99% sensitivity for robust classification of three ophthalmic surgical instruments commonly used in anterior segment operation. Furthermore, we demonstrate multi-instrument tracking and video-rate 4D imaging of ophthalmic surgical maneuvers in *ex vivo* porcine eyes. By leveraging advancements in deep-learning-based object detectors, we show that we are able to track and localize multiple surgical instruments in a single continuous acquisition without the need to reinitialize acquisition or detection parameters.

Additionally, the network can be directly extended for use in visualization and tracking of posterior segment maneuvers. System throughput was originally measured and optimized through a surgical microscope objective lens and BIOM lens for 5.5 mW combined SER and OCT power at the pupil, which is below maximum permissible exposure limits in the near-infrared regime as dictated

by the ANSI safety standards. Furthermore, the system uses extended-source illumination, and SER and OCT beams are spatially offset from one another, thus improving safety for posterior segment imaging. Here, we integrate our SECTR probe with the objective lens of a surgical microscope. Full microscope-integration can be achieved by simply integrating the current system with the reduction and widefield ophthalmic lens of a BIOM. Nevertheless, automated instrument-tracking can be achieved without change to the implemented framework due to the inherent spatio-temporal co-registration between SER and OCT imaging. Beyond surgical applications, multi-instrument tracking and real-time volumetric imaging of surgical maneuvers has potential benefits for ophthalmic training and skill-assessment. Ophthalmic microsurgery requires high precision that results in a steep learning curve. Thus, training can potentially be facilitated by video-rate 4D imaging of instrument-tissue interactions as well as by extraction of quantitative metrics relating to tissue deformation or tissue damage during operation. The proposed automated-instrument tracking method enables video-rate 4D imaging of multiple instruments during ophthalmic surgery and addresses critical barriers to the broad adoption of iOCT technology.

CHAPTER 7

Summary and Future Directions

The following chapter contains content that is adapted from M. J. Ringel, E. M. Tang, and Y. K. Tao, "Advances in multimodal imaging in ophthalmology," Therapeutic Advances in Ophthalmology (2021).

7.1 Summary

Ophthalmic diseases often require surgical intervention to prevent progression and to improve patient visual acuity and quality of life. However, ophthalmic surgery is complex and involves manipulation of sub-millimeter-thick, semi-transparent tissues. As outlined in Chapter 2, current visualization is limited to white-light stereomicroscopes, which provide only an *en face* view of these structures. iOCT systems have been developed for 3D visualization of ophthalmic microtissue, but broad adoption of iOCT technology is inhibited by three major limitations: 1) static cross-sectional imaging due to slow commercial system speeds, 2) the presence of motion artifacts that degrade image quality, 3) lack of automated-instrument tracking that necessitates manual adjustment of static OCT FOVs. The work described in this dissertation addresses these major barriers to the adoption of iOCT technology.

In Chapter 3, we describe the utility of high-speed SECTR imaging for spatio-temporally co-registered *en face* SER and cross-sectional OCT imaging. Co-registration and orthogonality between these two imaging modalities facilitates 3D motion-tracking and 4D imaging. A compact and portable SECTR system was designed and engine throughput was optimized for video-rate 4D clinical imaging. In addition, we assessed and validated the motion tracking performance by utilizing a handheld SECTR probe for OCTA imaging. OCTA projections emphasized bulk motion artifacts,

which arise from both operator and patient motion, and were indicative of intraoperative motion. SER-based motion tracking and correction facilitated precise reconstruction of OCTA volumes despite the presence of extreme motion artifacts. In Chapter 4, we further optimized system performance by performing both hardware and software optimization via galvanometer tuning optimization and scan waveform optimization. We developed optimized scanning protocols for 4D imaging that improved both speed and linearity compared to conventional sampling protocols with default tunings.

In Chapter 5, we leveraged our optimized SECTR system for deep-learning-based tracking and detection of 25G ILM forceps. We demonstrated resolution-limited detection accuracy and high-speed detection at over 120 Hz for video-rate 4D imaging of instrument maneuvers in paper samples and 3D printed phantoms. In Chapter 6, we extended our network for multi-instrument and multi-channel detection of ophthalmic surgical instruments. Additionally, we integrated a surgical microscope objective lens with our SECTR probe for assessment of microscope-integrated tracking performance. We demonstrated high classification accuracy for detection of three different classes of surgical instruments and we validate multi-channel network performance by performing video-rate 4D imaging and automated instrument-tracking in *ex vivo* porcine eyes.

In this chapter, we present future developments that can be used to improve tracking performance and ophthalmic surgical visualization. Additionally, we describe advancements in current methods and potential metrics that can be used to assess the utility of automated instrument-tracking and 4D visualization of ophthalmic surgical maneuvers. Current clinical studies are limited by the use of commercial iOCT systems that provide static cross-sectional OCT visualization. Future studies are crucial to provide quantitative information from 4D OCT that can be used to assess operator performance and surgical success. Quantitative intraoperative assessment of surgical maneuvers can be directly correlated with postoperative patient outcomes and is therefore critical for ophthalmic training and evaluation.

7.2 Tracking Optimization

Our proposed automated instrument-tracking framework achieves high performance and speed that is fundamentally limited by volumetric imaging rates. We have demonstrated detection rates between 23-120 Hz (multi-channel vs. single-channel), while video-rate visualization corresponds to updates rates of 16-20 Hz. Although improving detection speed is not necessary, faster detection facilitates the use of additional pre-processing methods that can potentially improve detection and tracking accuracy. For example, more complex image-processing methods can be used, such as gradient-based edge detection. Gradient images can then be encoded as individual network channels for improved classification performance. Higher detection speed can be achieved by leveraging parallel computational and deep-learning advancements. Our current system utilizes relatively modest computational power and operates on an Intel i9-10900X CPU, an NVIDIA GeForce RTX 2080 Ti GPU and 64 GB RAM. A significant performance increase can be expected by upgrading to high-end GPUs, such as the GeForce RTX 3090 (10496 cores), and by improving memory/memory speed (24 GB, GDDR6X). Furthermore, multiple improvements in CNN-based object detection have been demonstrated since YOLOv4 was released in 2020. The recent introduction of YOLOv5 [325] and YOLOX [326] demonstrate potential advantages for both improved network detection speed as well as improved detection accuracy.

Additionally, recent implementations of CNNs for object detection or classification have leveraged 4D information via RGB-X data encoding [327]–[329]. Additional information, typically RGB-D (depth), is encoded for multi-channel network detection. These systems take advantage of recent advances in camera sensors that are able to encode both RGB and NIR or depth information. Our current CNN implementation leverages 3-channel detection (BGR) but can be extended for 4-channel detection by incorporating additional information, such as image gradients. Along the lines of depth-encoded information, we can also potentially leverage depth-resolved OCT imaging by encoding *en face* OCT projections along with the 3-channel SER data described previously. *En face* OCT intensity projections would provide high instrument contrast due to the high reflectivity of the

surgical instrument relative to ophthalmic tissue. In addition, *en face* OCT images do not suffer from reflection, saturation, or shadowing artifacts compared to SER or surgical microscope images. The spatio-temporal co-registration between SER and OCT imaging also ensures lateral overlap, which facilitates instrument detection and localization.

7.3 Rendering and Display

High-resolution visualization of ocular tissues is a crucial component of ophthalmic microsurgery. Surgeons generally operate through the oculars of a white-light stereomicroscope, which provides an *en face* view of underlying tissue. These stereomicroscopes also provide pseudo-depth visualization through the stereopsis effect, but ultimately lack true depth-resolved visualization of ophthalmic tissues. Although MI-OCT has enabled 3D visualization, integration of cross-sectional and volumetric iOCT data into the surgical view is a challenging task. Traditionally, white-light images captured during surgery are also simultaneously relayed to an external monitor for additional heads-up visualization. These external monitors provide limited visualization of the surgical microenvironment due to low conventional camera resolution (1920 x 1080 pix.), thus limiting the overall utility of heads-up surgery [330]. Recent advancements have focused on the design of 4K high-definition (3840 x 2160 pix.) and 8K ultra-high definition (7680 x 4320 pix.) heads-up systems that provide 2-4x higher resolution compared to current commercial systems [86], [331].

Despite these advancements, seamless integration of iOCT depth information requires real-time visualization and feedback for guidance of ophthalmic surgical maneuvers. Heads-up display (HUD) systems that incorporate iOCT cross-sectional images through the oculars of the surgical microscope have previously been demonstrated [131]. These integrated systems present significant visual advantages over external displays by enabling immediate iOCT feedback without the need to turn away from the surgical field [332]. Systems incorporating rapid volumetric iOCT and HUD integration have also demonstrated simultaneous 4D MI-OCT and operating microscope view visualization [333]. Furthermore, it was found that integrated real-time volumetric visualization did not significantly affect the resolution, FOV, or image quality of the surgical microscope view. Studies

have also demonstrated an ergonomic advantage of HUD systems, which enable surgeons to sit more comfortably and can potentially reduce musculoskeletal pain [334]. In addition to these augmented reality systems, virtual reality iOCT display through the use of immersive systems, such as the Oculus Rift, have also been explored [335], [336]. Virtual reality display through head-mounted systems presents significant advantages by providing a greater FOV compared to surgical microscope oculars (105° vs. 45° FOV), which enables enhanced visualization of iOCT and surgical microscope views, as well as potential to incorporate additional information, such as patient vital signs.

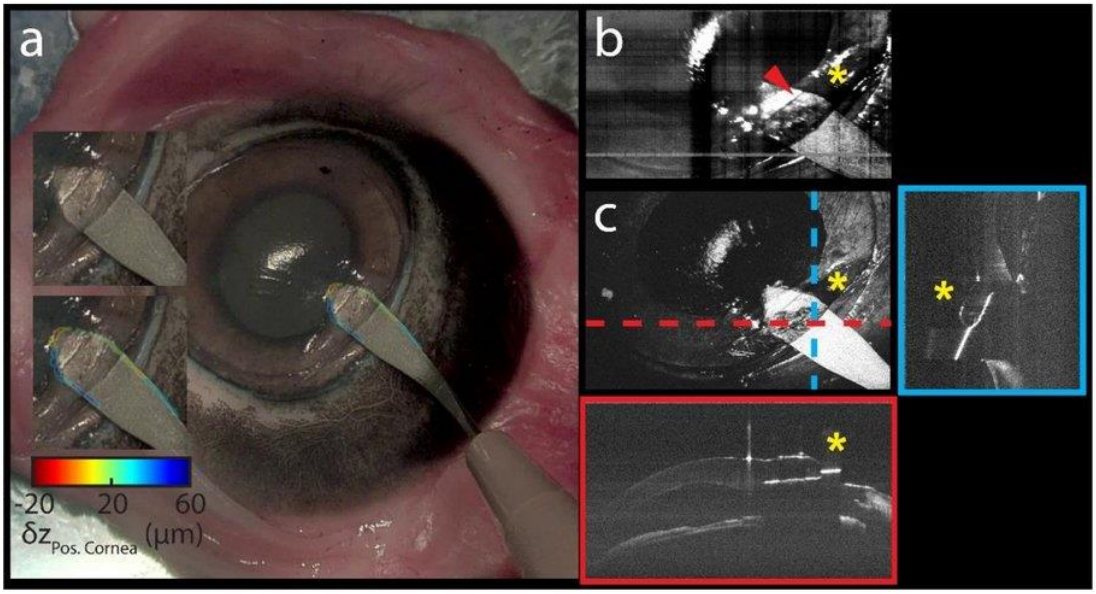

Fig. 7.1. Microscope-integrated SECTR imaging of anterior segment maneuvers acquired in *ex vivo* porcine eyes. (a) Surgical microscope view showing axial position overlay relative to posterior cornea extracted from co-registered (b) *en face* SER and (c) *en face* OCT projection. Reprinted with permission from [337].

Preliminary studies assessing the utility and efficacy of 3D HUD systems for ophthalmic microsurgery have demonstrated similar postoperative outcomes and visual acuity and have shown no significant difference in overall operating times compared to conventional surgical microscope operation [338]–[342]. However, the commercial HUD systems used in these studies (Alcon 3D NGENUITY, TrueVision 3D Visualization, and Zeiss ARTEVO 800) lack iOCT integration that can

improve visualization of ophthalmic surgical maneuvers and therefore patient outcomes. Furthermore, commercial iOCT HUD systems are limited to static cross-sectional imaging due to their slow imaging rates. Thus, there exists a need to combine current-generation commercial 3D HUD technology with research-grade 4D MI-OCT systems. Our group has previously demonstrated high-speed intraoperative SECTR imaging and real-time display of SER and OCT images using a TrueVision camera for heads-up visualization (Fig. 7.1) [337]. Additionally, the automated instrument-tracking and motion-tracking methods described in this dissertation enable video-rate 4D visualization of ophthalmic surgical maneuvers. Display of 4D OCT information using integrated 3D HUD technology will facilitate the visualization of bulk interactions between the surgical instrument and underlying tissue and will enable real-time guidance of ophthalmic surgery.

7.4 Automated Segmentation

Automated extraction of key intraoperative features, such as instrument depth, is crucial for providing real-time feedback that can be used to assess progress and performance during ophthalmic surgery. Several methods have been explored for automated segmentation from OCT images for applications in both anterior segment and posterior segment operations. Automated segmentation of corneal layer thickness and needle position has been demonstrated for real-time tracking of needle depth for guidance of DALK procedures [177]. Similarly, an automated method for assessing graft orientation has recently been demonstrated for guidance of DMEK surgery [343]. Previous studies have also been used for automated segmentation of fluid-interface volume following DSAEK [344], [345]. These studies have shown that automated segmentation can be used to provide crucial quantitative information that can be directly correlated to technique-dependent differences between surgeons and to postoperative graft nonadherence. In addition, iOCT feedback and segmentation facilitated the reduction of interface fluid during operation by providing real-time surgical guidance.

iOCT feedback during posterior segment operation has also benefitted from automated segmentation and quantification of key parameters associated with patient outcomes. Segmentation of macular hole thickness and volume from iOCT images has provided insight into postoperative

macular hole closure, which was found to be negatively correlated with reduction in macular hole width and was postulated to be due to trauma resulting from ILM peeling [346]. Automated segmentation of needle position from MI-OCT images has also been demonstrated for subretinal injection guidance [347], [348]. These studies enable accurate estimation of 3D needle pose and precise guidance of injection procedures has been demonstrated in *ex vivo* porcine eyes [349]. Furthermore, quantification of injection volume can be performed by subretinal bleb segmentation, which facilitates dosing assessment and delivery efficacy for ocular therapeutics [350]. With parallel advancements in deep-learning, more recent studies for segmentation of posterior segment features have leveraged network-based algorithms for rapid and accurate segmentation of retinal layer boundaries, quantification of layer thicknesses, and intraretinal or subretinal fluid volume analysis [351]–[354].

While significant advancements have been made for automated segmentation and quantification of ophthalmic surgical features, 3D visualization of real-time volumetric iOCT data remains challenging due to inherently lower SNR compared to clinical OCT systems. Additionally, optimal volumetric rendering is in inhibited by degradation of imaging performance due to limited FOVs and sampling density, speckle noise, and instrument-shadowing. These limitations ultimately reduce the performance of feature-extraction algorithms for instrument segmentation or ocular tissue segmentation, which can be used to improve intraoperative feedback and visualization. Recent advances for improving visualization of 4D iOCT data have incorporated automated segmentation algorithms for rapid retinal layer and instrument segmentation [147], [355]. These methods rely on static reference volumes and automated instrument segmentation in order to simultaneously encode instrument color and fill in information due to instrument-shadowing. Integration of the proposed SECTR-based automated instrument-tracking method with optimized deep-learning-based instrument/tissue segmentation and color-encoded 4D rendering methods can significantly improve visualization of video-rate 4D iOCT data and potentially reduce technological learning curves for ophthalmic surgeons. Further integration with modern 3D HUD technology described in Section 7.3

can also provide surgeons with improved feedback compared to current iOCT HUD systems, which rely solely on cross-sectional OCT views with limited display resolution.

7.5 Quantitative Surgical Guidance

iOCT provides depth-resolved information that can be used to quantify intraoperative and postoperative structural changes. Several of these features, such as retinal layer thickness, macular hole thickness, and fluid at the corneal graft-host interface, are directly correlated with patient outcomes as described in the previous section. Furthermore, video-rate 4D imaging systems present significant advantages over current commercial MI-OCT by enabling analysis of bulk interactions between the surgical instrument and underlying tissues. Quantitative metrics, such as tissue deformation, have yet to be established with conventional iOCT systems that are limited to static cross-sectional imaging. Preliminary qualitative studies have shown significant deformation of the retina and macular hole during ERM peeling due to interactions between the surgical instrument (e.g. finesse loop or diamond-dusted membrane scraper) and underlying tissue [356]. These surgical interactions generate currently unquantified tractional forces that result in visible striation or dimpling of the retina and can potentially lead to persistent postoperative retinal deformation. One study has utilized a depth-encoded color gradient to better visualize 4D MI-OCT data and tissue deformation in order to assess ophthalmic surgical skills (Fig. 7.2) [357]. The study has found that depth-encoded colorization enabled more accurate differentiation of the membrane from the retinal surface and more accurate identification of instrument contact with the retinal surface and of retinal deformation.

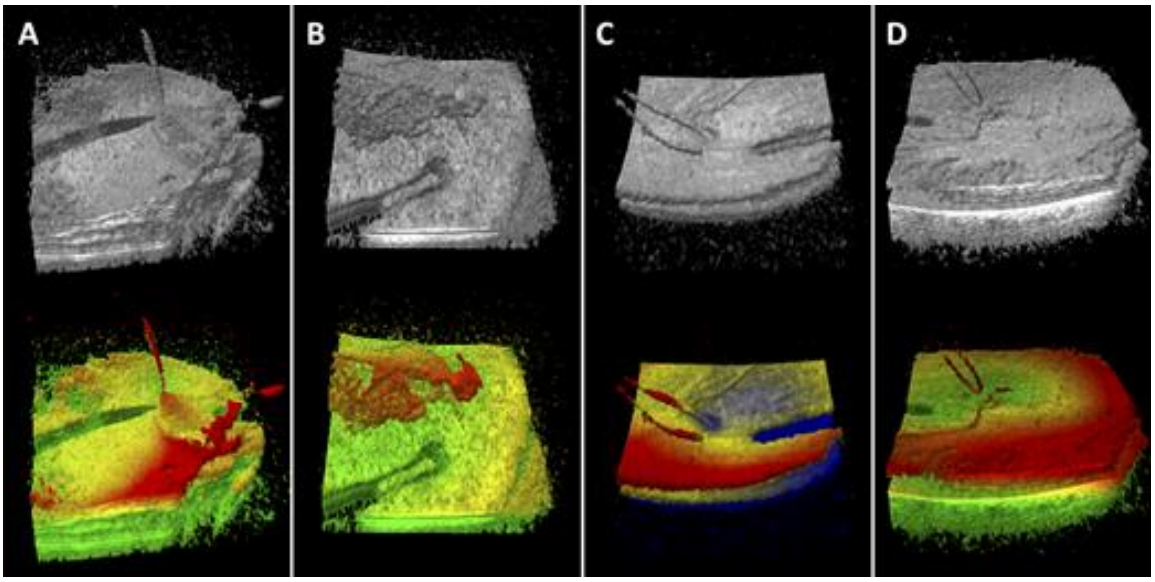

Fig. 7.2. Motion-stabilized colorization of MI-OCT volumes acquired during membrane peeling. Panels show (a) membrane traction, (b) membrane pulling by forceps, (c) retinal deformation by finesse loop, and (d) finesse loop surface approach. Reprinted with permission from [357].

These previous studies show that establishing quantitative deformation metrics is crucial to correlate intraoperative surgical maneuvers with postoperative outcomes. The most common techniques for assessing tissue deformation are optical coherence elastography (OCE) and phase-decorrelation OCT (PhD-OCT). OCE is an analog of OCT that is used to detect micron-scale displacements caused by an external mechanical stimulus to extract biomechanical properties of tissue [358], [359]. PhD-OCT is an alternate method for measuring tissue biomechanics that uses the decorrelation of scattered light from Brownian motion as a surrogate measure of tissue viscosity [360]–[362]. Initial OCE demonstrations used OCT speckle tracking of axial displacements from a static loading force to quantify tissue strain and derived Young's modulus from the linear stress–strain relationship [363], [364]. OCE can also be used to measure Young's and shear moduli by combining dynamic loading forces, such as steady-state harmonic loading and transient excitation *in vivo* measurement of sources, with advanced wave propagation models [365]. These dynamic OCE methods have been used to non-invasively measure biomechanical properties of the human cornea *in vivo*, showing the potential for intraoperative translation and utility [366].

Established applications of OCE include corneal elasticity measurement, which is useful for

diagnosing keratoconus and corneal ectasia and monitoring corneal collagen crosslinking (CXL) treatment [367]–[370]. OCE has shown increased corneal stiffness in in vivo rabbit eyes after CXL treatments with an air puff as the external mechanical stimulus (Fig. 7.3(a),(b)) [371]–[373]. Furthermore, PhD-OCT has successfully identified changes in corneal biomechanics after CXL in vivo without the need for external stimuli [362]. OCE studies have also shown distinct elasticity differences in retinal layers in *in vivo* rabbit and *ex vivo* porcine models (Figure 7.3(c),(d)) [374], [375]. OCE studies have also shown that increased optic nerve head Young's modulus and posterior scleral stiffness are correlated with increasing IOP, which suggests that OCE can also be used to monitor progression of glaucoma [376], [377]. These studies indicate that OCT-derived surrogates, such as OCE and PhD-OCT, have the potential to provide quantitative intraoperative information related to tissue mechanics for the real-time assessment of tissue deformation and damage.

Although quantitative assessment of intraoperative tissue deformation can be used to better understand postoperative outcomes, current MI-OCT systems are limited by static cross-sectional imaging and lack of automated instrument-tracking. As a result, these systems are unable to visualize deformation or bulk interactions between the surgical instrument and underlying tissue. Furthermore, OCE or PhD-OCT assessment of tissue mechanics would also be fundamentally limited to these individual cross-sections. Thus, automated instrument-tracking and video-rate 4D visualization of surgical maneuvers has potential utility for both improving visualization and allowing for quantification of tissue deformation. The proposed method allows for more robust volumetric analysis of tissue mechanics as well as 4D visualization of ophthalmic surgical maneuvers without the need for manual adjustment. These advancements facilitate the integration of accurate and efficient algorithms for quantifying intraoperative deformation mechanics that can be used for ophthalmic surgical guidance and improved patient outcomes.

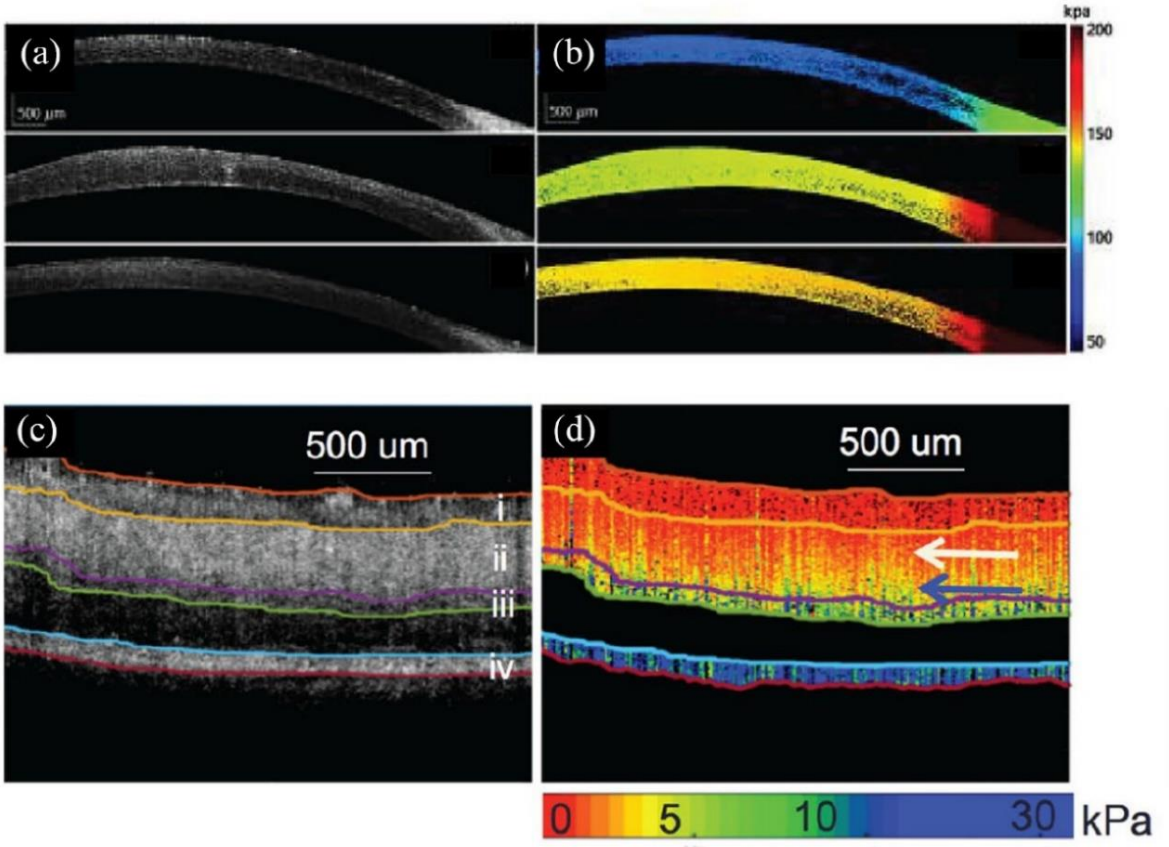

Fig. 7.3. OCE imaging of the (a), (b), cornea and (c), (d) retina. (a) Structural OCT and (b) OCE elastogram cross sections of in vivo rabbit cornea pre-, post-, and 1 week after CXL treatment (top to bottom, respectively) [371]. (c) Structural OCT and (d) OCE elastogram cross sections of ex vivo porcine retina showing differences in retinal layer stiffness [374].

7.6 Surgical Robotics

Image-guided feedback during surgery improves visualization of tissue structures and is particularly useful when manipulating fine features and when haptic feedback is limited as is the case for minimally-invasive surgery and ophthalmic microsurgery. These surgeries require complex maneuvers and precision control of instrument-tissue interactions that is inhibited by natural human physiological tremor and instability [378]. Recently, robotic surgery has been extended for ophthalmic applications for potentially enhanced performance of intricate maneuvers. Robotic surgery in experimental eyes has been performed using the Da Vinci Xi surgical system for phacoemulsification during cataract surgery and penetrating keratoplasty [379], [380]. These studies

demonstrated the feasibility of using these robotic platforms for fine ophthalmic surgical maneuvers, such as corneal suturing. Previous studies have also assessed the feasibility of using robotic systems for posterior segment operation in a virtual environment and *ex vivo* porcine eyes [381], [382]. However, performance for vitreoretinal procedures was significantly diminished due to lack of haptic feedback for accurate control of robotic instruments as well as inferior endoscopic image quality compared to the surgical microscope view. Robot-assisted surgery was also shown to be significantly slower compared to manual surgery, which was attributed to a steep learning curve for robotic operation. However, robotic operation improved movement precision for both novice and trained vitreoretinal surgeons and novice operators also inflicted less tissue damage in virtual-reality simulations compared to manual surgery. These results suggest that improved visualization of robotic maneuvers and enhanced haptic feedback will facilitate translation of robot-assisted ophthalmic surgery.

Image-guided robot-assisted ophthalmic surgery has recently been demonstrated by incorporating iOCT feedback of robotic maneuvers. iOCT provides micron-depth resolution and visualization ocular structures and enables enhanced feedback of precise maneuvers compared to *en face* microscopic or endoscopic views. One study has demonstrated iOCT-based needle tracking and guidance for robot-assisted needle insertion for DALK [383]. Automated segmentation of needle pose from acquired OCT volumes was used to manipulate a robotic arm for precise needle depth insertion. Robot-assisted needle insertion was more precise and accurate compared to those performed by surgical fellows in *ex vivo* porcine eyes. Another study has also demonstrated high precision robotic needle insertion for DALK with small tip errors of 3.6 μm [384]. Furthermore, similar methods have been implemented for robot-assisted subretinal injection and have demonstrated accurate needle detection and localization from OCT volumes with a mean calibration error of 9.2 μm [385].

Volumetric visualization of ocular tissue enhances the precision of robotic ophthalmic surgery, but accurate manipulation of ocular tissues is ultimately inhibited by lack of force control and tactile

feedback. Methods for force-sensing often involve the modification of surgical instruments for the implementation of micromanipulators and sensors [386]–[388]. However, these methods are limited by sterilizability concerns as well as sensor size, which may affect ergonomics of surgical maneuvers. Recently, methods have been developed that rely on more compact optical fibers for OCT-based sensing of needle tip insertion force [389], [390]. Additionally, a deep-learning-based method has been proposed to estimate force directly from OCT volumes [391]. In this study, instrument movement by a robot with varying applied forces is used to deform a tissue sample or phantom. Corresponding OCT volume and force sensor measurements are used to train a CNN for automated force estimation without the need for instrument modification.

Despite advancements in image-guided robotic surgery and improvements in force-sensing capabilities, visualization of complex ophthalmic maneuvers is limited by *en face* surgical microscope views and slow volumetric imaging rates of commercial MI-OCT systems. Furthermore, detection of the surgical instrument via OCT-based segmentation relies on the assumption that the instrument remains localized within the OCT volume. As a result, movement of the instrument outside of the OCT FOV requires manual updates for relocalization and inhibits robotic surgery utility. The proposed automated instrument-tracking and high-speed video-rate 4D imaging platform provides significant benefits that can be used to improve robot-assisted ophthalmic surgery. Automated instrument-tracking enables continuous localization of the surgical instrument within the OCT FOV while providing volumetric information that can be used to accurately and efficiently determine instrument pose for improved robotic feedback. Furthermore, video-rate 4D imaging provides high-speed volumetric OCT data that can be used for real-time visualization and segmentation algorithms.

References

[1] M. J. Ringel, E. M. Tang, and Y. K. Tao, “Advances in multimodal imaging in ophthalmology:,” *https://doi.org/10.1177/25158414211002400*, vol. 13, p. 251584142110024, Mar. 2021, doi: 10.1177/25158414211002400.

[2] World Health Organization, “World report on vision,” *World health Organization*, vol. 214, no. 14, pp. 1–160, 2019.

[3] R. R. A. Bourne *et al.*, “Trends in prevalence of blindness and distance and near vision impairment over 30 years: An analysis for the Global Burden of Disease Study,” *The Lancet Global Health*, vol. 9, no. 2, pp. e130–e143, Feb. 2021, doi: 10.1016/S2214-109X(20)30425-3/ATTACHMENT/CB85E062-C3F0-4883-9CA8-3EF91A0BC419/MMC1.PDF.

[4] A. Gordois *et al.*, “An estimation of the worldwide economic and health burden of visual impairment,” *https://doi.org/10.1080/17441692.2011.634815*, vol. 7, no. 5, pp. 465–481, May 2012, doi: 10.1080/17441692.2011.634815.

[5] W. Schakel, H. P. A. van der Aa, C. Bode, C. T. J. Hulshof, G. H. M. B. van Rens, and R. M. A. van Nispen, “The Economic Burden of Visual Impairment and Comorbid Fatigue: A Cost-of-Illness Study (From a Societal Perspective),” *Investigative Ophthalmology & Visual Science*, vol. 59, no. 5, pp. 1916–1923, Apr. 2018, doi: 10.1167/IOVS.17-23224.

[6] R. R. A. Bourne *et al.*, “Causes of blindness and vision impairment in 2020 and trends over 30 years, and prevalence of avoidable blindness in relation to VISION 2020: the Right to Sight: an analysis for the Global Burden of Disease Study,” *Lancet Glob Health*, vol. 9, no. 2, pp. e144–e160, Feb. 2021, doi: 10.1016/S2214-109X(20)30489-7.

[7] E. Y. Chew *et al.*, “The age-related eye disease study 2 (AREDS2): Study design and baseline characteristics (AREDS2 Report Number 1),” *Ophthalmology*, vol. 119, no. 11, pp. 2282–2289, Nov. 2012, doi: 10.1016/j.ophtha.2012.05.027.

[8] S. Ramachandran, A. M. Ghanem, and S. R. Myers, “Assessment of microsurgery competency-

where are we now?," *Microsurgery*, vol. 33, no. 5, pp. 406–415, Jul. 2013, doi: 10.1002/micr.22111.

[9] B. Usmani, M. Iftikhar, A. Latif, and S. M. A. Shah, "Epidemiology of primary ophthalmic procedures performed in the United States," *Canadian Journal of Ophthalmology*, vol. 54, no. 6, pp. 727–734, Dec. 2019, doi: 10.1016/J.JCJO.2019.03.006.

[10] G. Davis, "The Evolution of Cataract Surgery," *Missouri Medicine*, vol. 113, no. 1, p. 58, Jan. 2016, doi: 10.1097/apo.0b013e31829df4bf.

[11] T. H. Williamson, "Complications of Anterior Segment Surgery," *Vitreoretinal Surgery*, pp. 431–464, 2021, doi: 10.1007/978-3-030-68769-4_17.

[12] E. Chan, O. A. R. Mahroo, and D. J. Spalton, "Complications of cataract surgery," *https://doi.org/10.1111/j.1444-0938.2010.00516.x*, vol. 93, no. 6, pp. 379–389, Nov. 2021, doi: 10.1111/J.1444-0938.2010.00516.X.

[13] S. J. Gedde, L. W. Herndon, J. D. Brandt, D. L. Budenz, W. J. Feuer, and J. C. Schiffman, "Postoperative complications in the Tube Versus Trabeculectomy (TVT) study during five years of follow-up," *Am J Ophthalmol*, vol. 153, no. 5, p. 814.e1, May 2012, doi: 10.1016/J.AJO.2011.10.024.

[14] L. Vijaya, P. Manish, G. Ronnie, and B. Shantha, "Management of complications in glaucoma surgery," *Indian Journal of Ophthalmology*, vol. 59, no. Suppl1, p. S131, Jan. 2011, doi: 10.4103/0301-4738.73689.

[15] D. L. Budenz *et al.*, "Postoperative Complications in the Ahmed Baerveldt Comparison Study During Five Years of Follow-up," *Am J Ophthalmol*, vol. 163, pp. 75-82.e3, Mar. 2016, doi: 10.1016/J.AJO.2015.11.023.

[16] N. K. Sahoo, P. Balijepalli, S. R. Singh, M. Jhingan, S. Senthil, and J. Chhablani, "Retina and glaucoma: Surgical complications," *International Journal of Retina and Vitreous*, vol. 4, no. 1, pp. 1–15, Sep. 2018, doi: 10.1186/S40942-018-0135-X/FIGURES/2.

[17] D. T. H. Tan and A. Anshu, "Anterior lamellar keratoplasty: 'Back to the Future'– a review," *Clinical & Experimental Ophthalmology*, vol. 38, no. 2, pp. 118–127, Mar. 2010, doi:

10.1111/J.1442-9071.2009.02180.X.

[18] M. O. Price and F. W. Price, “Endothelial keratoplasty – a review,” *Clinical & Experimental Ophthalmology*, vol. 38, no. 2, pp. 128–140, Mar. 2010, doi: 10.1111/J.1442-9071.2010.02213.X.

[19] R. J. Olson, M. Pingree, R. Ridges, M. L. Lundergan, C. Alldredge, and T. E. Clinch, “Penetrating keratoplasty for keratoconus: a long-term review of results and complications,” *Journal of Cataract & Refractive Surgery*, vol. 26, no. 7, pp. 987–991, Jul. 2000, doi: 10.1016/S0886-3350(00)00430-2.

[20] I. Rahman, F. Carley, C. Hillarby, A. Brahma, and A. B. Tullo, “Penetrating keratoplasty: indications, outcomes, and complications,” *Eye 2009 23:6*, vol. 23, no. 6, pp. 1288–1294, Oct. 2008, doi: 10.1038/eye.2008.305.

[21] M. A. Terry and P. J. Ousley, “Deep lamellar endothelial keratoplasty: Early complications and their management,” *Cornea*, vol. 25, no. 1, pp. 37–43, Jan. 2006, doi: 10.1097/01.ICO.0000164781.33538.B6.

[22] W. B. Lee, D. S. Jacobs, D. C. Musch, S. C. Kaufman, W. J. Reinhart, and R. M. Shtein, “Descemet’s Stripping Endothelial Keratoplasty: Safety and Outcomes: A Report by the American Academy of Ophthalmology,” *Ophthalmology*, vol. 116, no. 9, pp. 1818–1830, Sep. 2009, doi: 10.1016/J.OPHTHA.2009.06.021.

[23] J. S. Parker, K. van Dijk, and G. R. J. Melles, “Treatment options for advanced keratoconus: A review,” *Survey of Ophthalmology*, vol. 60, no. 5, pp. 459–480, Sep. 2015, doi: 10.1016/J.SURVOPHTHAL.2015.02.004.

[24] S. v. Jeganathan, S. Ghosh, V. Jhanji, E. Lamoureux, H. R. Taylor, and R. B. Vajpayee, “Resuturing following penetrating keratoplasty: a retrospective analysis,” *Br J Ophthalmol*, vol. 92, no. 7, pp. 893–895, Jul. 2008, doi: 10.1136/BJO.2007.133421.

[25] S. Den, S. Shimmura, K. Tsubota, and J. Shimazaki, “Impact of the Descemet Membrane Perforation on Surgical Outcomes After Deep Lamellar Keratoplasty,” *American Journal of Ophthalmology*, vol. 143, no. 5, pp. 750–754, May 2007, doi: 10.1016/J.AJO.2007.01.053.

[26] M. Erdurmus *et al.*, “Steroid-induced intraocular pressure elevation or glaucoma after penetrating keratoplasty in patients with keratoconus or Fuchs dystrophy.,” *Cornea*, vol. 28, no. 7, pp. 759–764, 2009, doi: 10.1097/ICO.0B013E3181967318.

[27] K. K. Huber *et al.*, “Glaucoma in penetrating keratoplasty: Risk factors, management and outcome,” *Graefe’s Archive for Clinical and Experimental Ophthalmology*, vol. 251, no. 1, pp. 105–116, Jan. 2013, doi: 10.1007/S00417-012-2065-X/FIGURES/3.

[28] S. Rumelt, V. Bersudsky, T. Blum-Hareuveni, and U. Rehany, “Preexisting and postoperative glaucoma in repeated corneal transplantation,” *Cornea*, vol. 21, no. 8, pp. 759–765, Nov. 2002, doi: 10.1097/00003226-200211000-00005.

[29] S. S. Tuli, D. WuDunn, T. A. Ciulla, and L. B. Cantor, “Delayed suprachoroidal hemorrhage after glaucoma filtration procedures,” *Ophthalmology*, vol. 108, no. 10, pp. 1808–1811, Oct. 2001, doi: 10.1016/S0161-6420(01)00763-1.

[30] K. Vaziri *et al.*, “Incidence of postoperative suprachoroidal hemorrhage after glaucoma filtration surgeries in the United States,” *Clinical Ophthalmology (Auckland, N.Z.)*, vol. 9, p. 579, Apr. 2015, doi: 10.2147/OPTH.S78359.

[31] W. J. Waterhouse *et al.*, “Rhegmatogenous Retinal Detachment after Molteno Glaucoma Implant Surgery,” *Ophthalmology*, vol. 101, no. 4, pp. 665–671, Apr. 1994, doi: 10.1016/S0161-6420(94)31280-2.

[32] G. D. Gilliland, W. L. Hutton, and D. G. Fuller, “Retained Intravitreal Lens Fragments after Cataract Surgery,” *Ophthalmology*, vol. 99, no. 8, pp. 1263–1269, Aug. 1992, doi: 10.1016/S0161-6420(92)31814-7.

[33] S. Oruc and H. J. Kaplan, “Outcome of vitrectomy for retained lens fragments after phacoemulsification,” *http://dx.doi.org/10.1076/ocii.9.1.41.3979*, vol. 9, no. 1, pp. 41–47, 2009, doi: 10.1076/OCII.9.1.41.3979.

[34] A. M. Thompson, N. Sachdev, T. Wong, A. F. Riley, C. N. Grupcheva, and C. N. McGhee, “The Auckland Cataract Study: 2 year postoperative assessment of aspects of clinical, visual, corneal

topographic and satisfaction outcomes," *British Journal of Ophthalmology*, vol. 88, no. 8, pp. 1042–1048, Aug. 2004, doi: 10.1136/BJO.2003.032581.

[35] P. Barry *et al.*, "Prophylaxis of postoperative endophthalmitis following cataract surgery: Results of the ESCRS multicenter study and identification of risk factors," *Journal of Cataract & Refractive Surgery*, vol. 33, no. 6, pp. 978–988, Jun. 2007, doi: 10.1016/J.JCRS.2007.02.032.

[36] M. D. McLaughlin and J. C. Hwang, "Trends in Vitreoretinal Procedures for Medicare Beneficiaries, 2000 to 2014," *Ophthalmology*, vol. 124, no. 5, pp. 667–673, May 2017, doi: 10.1016/j.ophtha.2017.01.001.

[37] T. A. Albini, S. G. Schwartz, and J. L. Davis, "Vitrectomy," *Intraocular Inflammation*, pp. 493–499, Jul. 2021, doi: 10.1007/978-3-540-75387-2_39.

[38] J. H. Roh, H. J. Sohn, D. Y. Lee, K. H. Shyn, and D. H. Nam, "Comparison of Posterior Capsular Opacification between a Combined Procedure and a Sequential Procedure of Pars Plana Vitrectomy and Cataract Surgery," *Ophthalmologica*, vol. 224, no. 1, pp. 42–46, Jan. 2010, doi: 10.1159/000234907.

[39] S. Schulz-Key, J. O. Carlsson, and S. Crafoord, "Longterm follow-up of pars plana vitrectomy for vitreous floaters: complications, outcomes and patient satisfaction," *Acta Ophthalmologica*, vol. 89, no. 2, pp. 159–165, Mar. 2011, doi: 10.1111/J.1755-3768.2009.01682.X.

[40] J. Y. Lee, K. H. Kim, K. H. Shin, D. H. Han, D. Y. Lee, and D. H. Nam, "Comparison of intraoperative complications of phacoemulsification between sequential and combinedprocedures of pars plana vitrectomy and cataract surgery," *Retina*, vol. 32, no. 10, pp. 2026–2033, Nov. 2012, doi: 10.1097/IAE.0B013E3182561FAB.

[41] O. P. Gupta *et al.*, "Short-term Outcomes of 23-gauge Pars Plana Vitrectomy," *American Journal of Ophthalmology*, vol. 146, no. 2, pp. 193-197.e1, Aug. 2008, doi: 10.1016/J.AJO.2008.04.010.

[42] B. Parolini, G. Prigione, F. Romanelli, M. G. Cereda, M. Sartore, and G. Pertile, "Postoperative complications and intraocular pressure in 943 consecutive cases of 23-gauge transconjunctival pars plana vitrectomy with 1-year follow-up," *Retina*, vol. 30, no. 1, pp. 107–111, Jan. 2010, doi:

10.1097/IAE.0B013E3181B21082.

[43] J. D. Stein, D. N. Zacks, D. Grossman, H. Grabe, M. W. Johnson, and F. A. Sloan, "Adverse Events After Pars Plana Vitrectomy Among Medicare Beneficiaries," *Archives of Ophthalmology*, vol. 127, no. 12, pp. 1656–1663, Dec. 2009, doi: 10.1001/ARCHOPHTHALMOL.2009.300.

[44] J. Sebag, "Vitreoschisis," *Graefe's Archive for Clinical and Experimental Ophthalmology*, vol. 246, no. 3, p. 329, Mar. 2008, doi: 10.1007/S00417-007-0743-X.

[45] J. C. Pastor, J. Rojas, S. Pastor-Idoate, S. di Lauro, L. Gonzalez-Buendia, and S. Delgado-Tirado, "Proliferative vitreoretinopathy: A new concept of disease pathogenesis and practical consequences," *Prog Retin Eye Res*, vol. 51, pp. 125–155, Mar. 2016, doi: 10.1016/J.PRETEYERES.2015.07.005.

[46] I. Chehaibou, M. Pettenkofer, A. Govetto, G. Rabina, S. V. R. Sadda, and J. P. Hubschman, "Identification of epiretinal proliferation in various retinal diseases and vitreoretinal interface disorders," *International Journal of Retina and Vitreous*, vol. 6, no. 1, pp. 1–9, Jul. 2020, doi: 10.1186/S40942-020-00233-0/FIGURES/4.

[47] A. T. Fung, J. Galvin, and T. Tran, "Epiretinal membrane: A review," *Clinical & Experimental Ophthalmology*, vol. 49, no. 3, pp. 289–308, Apr. 2021, doi: 10.1111/CEO.13914.

[48] F. Semeraro, F. Morescalchi, S. Duse, E. Gambicorti, A. Russo, and C. Costagliola, "Current trends about inner limiting membrane peeling in surgery for epiretinal membranes," *Journal of Ophthalmology*, vol. 2015, 2015, doi: 10.1155/2015/671905.

[49] J. G. Wong, N. Sachdev, P. E. Beaumont, and A. A. Chang, "Visual outcomes following vitrectomy and peeling of epiretinal membrane," *Clinical & Experimental Ophthalmology*, vol. 33, no. 4, pp. 373–378, Aug. 2005, doi: 10.1111/J.1442-9071.2005.01025.X.

[50] E. Abdelkader and N. Lois, "Internal Limiting Membrane Peeling in Vitreo-retinal Surgery," *Survey of Ophthalmology*, vol. 53, no. 4, pp. 368–396, Jul. 2008, doi: 10.1016/J.SURVOPHTHAL.2008.04.006.

[51] S. A. Schechet, E. Devience, and J. T. Thompson, "The effect of internal limiting membrane peeling

on idiopathic epiretinal membrane surgery, with a review of the literature," *Retina*, vol. 37, no. 5, pp. 873–880, 2017, doi: 10.1097/IAE.0000000000001263.

[52] G. Donati, A. D. Kapetanios, C. J. Pournaras, G. Donatí, A. D. Kapetanios, and C. J. Pournaras, "Complications of surgery for epiretinal membranes," *Graefe's Archive for Clinical and Experimental Ophthalmology 1998 236:10*, vol. 236, no. 10, pp. 739–746, Oct. 1998, doi: 10.1007/S004170050152.

[53] I. D. Fabian and J. Moisseiev, "Sutureless vitrectomy: evolution and current practices," *British Journal of Ophthalmology*, vol. 95, no. 3, pp. 318–324, Mar. 2011, doi: 10.1136/BJO.2009.176495.

[54] F. Schaub *et al.*, "Preexisting epiretinal membrane is associated with pseudophakic cystoid macular edema," *Graefe's Archive for Clinical and Experimental Ophthalmology*, vol. 256, no. 5, pp. 909–917, May 2018, doi: 10.1007/S00417-018-3954-4/TABLES/2.

[55] R. NARALA, N. NASSIRI, C. KIM, C. MEHREGAN, S. PADIDAM, and G. W. ABRAMS, "Outcomes of repeat pars plana vitrectomy after failed surgery for proliferative vitreoretinopathy," *Retina*, vol. 38, pp. S49–S59, Sep. 2018, doi: 10.1097/IAE.0000000000002000.

[56] E. Chen, "25-Gauge transconjunctival sutureless vitrectomy," *Current Opinion in Ophthalmology*, vol. 18, no. 3, pp. 188–193, May 2007, doi: 10.1097/ICU.0B013E328133889A.

[57] D. Pascolini and S. P. Mariotti, "Global estimates of visual impairment: 2010," *Br J Ophthalmol*, vol. 96, no. 5, pp. 614–618, May 2012, doi: 10.1136/BJOPHTHALMOL-2011-300539.

[58] A. Castro-Balado, C. Mondelo-García, I. Zarra-Ferro, and A. Fernández-Ferreiro, "New ophthalmic drug delivery systems.," *Farmacia Hospitalaria : Organo Oficial de Expresion Cientifica de la Sociedad Espanola de Farmacia Hospitalaria*, vol. 44, no. 4, pp. 149–157, Jul. 2020, doi: 10.7399/FH.11388.

[59] E. M. del Amo and A. Urtti, "Current and future ophthalmic drug delivery systems: A shift to the posterior segment," *Drug Discovery Today*, vol. 13, no. 3–4, pp. 135–143, Feb. 2008, doi: 10.1016/J.DRUDIS.2007.11.002.

[60] M. Dubald, S. Bourgeois, V. Andrieu, and H. Fessi, "Ophthalmic Drug Delivery Systems for

Antibiotherapy—A Review," *Pharmaceutics 2018, Vol. 10, Page 10*, vol. 10, no. 1, p. 10, Jan. 2018, doi: 10.3390/PHARMACEUTICS10010010.

[61] A. Urtti, "Challenges and obstacles of ocular pharmacokinetics and drug delivery," *Advanced Drug Delivery Reviews*, vol. 58, no. 11, pp. 1131–1135, Nov. 2006, doi: 10.1016/J.ADDR.2006.07.027.

[62] F. I. Al-Saikhan, "The gene therapy revolution in ophthalmology," *Saudi Journal of Ophthalmology*, vol. 27, no. 2, pp. 107–111, Apr. 2013, doi: 10.1016/J.SJOPT.2013.02.001.

[63] O. Weijtens *et al.*, "High concentration of dexamethasone in aqueous and vitreous after subconjunctival injection," *American Journal of Ophthalmology*, vol. 128, no. 2, pp. 192–197, Aug. 1999, doi: 10.1016/S0002-9394(99)00129-4.

[64] L. Pitkänen, V. P. Ranta, H. Moilanen, and A. Urtti, "Permeability of Retinal Pigment Epithelium: Effects of Permeant Molecular Weight and Lipophilicity," *Investigative Ophthalmology & Visual Science*, vol. 46, no. 2, pp. 641–646, Feb. 2005, doi: 10.1167/IOVS.04-1051.

[65] A. Urtti, "Challenges and obstacles of ocular pharmacokinetics and drug delivery," *Advanced Drug Delivery Reviews*, vol. 58, no. 11, pp. 1131–1135, Nov. 2006, doi: 10.1016/J.ADDR.2006.07.027.

[66] K. Nayak and M. Misra, "A review on recent drug delivery systems for posterior segment of eye," *Biomedicine & Pharmacotherapy*, vol. 107, pp. 1564–1582, Nov. 2018, doi: 10.1016/J.BIOPHA.2018.08.138.

[67] K. M. Sampat and S. J. Garg, "Complications of intravitreal injections," *Current Opinion in Ophthalmology*, vol. 21, no. 3, pp. 178–183, May 2010, doi: 10.1097/ICU.0B013E328338679A.

[68] C. H. Meyer *et al.*, "Incidence of Damage to the Crystalline Lens During Intravitreal Injections," *https://home.liebertpub.com/jop*, vol. 26, no. 5, pp. 491–495, Oct. 2010, doi: 10.1089/JOP.2010.0045.

[69] R. Gaudana, H. K. Ananthula, A. Parenky, and A. K. Mitra, "Ocular Drug Delivery," *The AAPS Journal*, vol. 12, no. 3, p. 348, Sep. 2010, doi: 10.1208/S12248-010-9183-3.

[70] K. G. Falavarjani and Q. D. Nguyen, "Adverse events and complications associated with intravitreal injection of anti-VEGF agents: a review of literature," *Eye 2013 27:7*, vol. 27, no. 7, pp. 787–794,

May 2013, doi: 10.1038/eye.2013.107.

[71] H. Heimann, “Intravitreal Injections: Techniques and Sequelae,” *Medical Retina*, pp. 67–87, Jun. 2007, doi: 10.1007/978-3-540-33672-3_5.

[72] C. J. Johnson, L. Berglin, M. A. Chrenek, T. M. Redmond, J. H. Boatright, and J. M. Nickerson, “Technical Brief: Subretinal injection and electroporation into adult mouse eyes,” *Molecular Vision*, vol. 14, p. 2211, Dec. 2008, Accessed: Apr. 11, 2022. [Online]. Available: /pmc/articles/PMC2593752/

[73] Y. Peng, L. Tang, and Y. Zhou, “Subretinal Injection: A Review on the Novel Route of Therapeutic Delivery for Vitreoretinal Diseases,” *Ophthalmic Res*, vol. 58, no. 4, pp. 217–226, Oct. 2017, doi: 10.1159/000479157.

[74] J. T. Stout and P. J. Francis, “Surgical Approaches to Gene and Stem Cell Therapy for Retinal Disease,” *Human Gene Therapy*, vol. 22, no. 5, p. 531, May 2011, doi: 10.1089/HUM.2011.060.

[75] M. Ross and R. Ofri, “The future of retinal gene therapy: evolving from subretinal to intravitreal vector delivery,” *Neural Regeneration Research*, vol. 16, no. 9, p. 1751, Sep. 2021, doi: 10.4103/1673-5374.306063.

[76] A. F. Mavrogenis *et al.*, “The history of microsurgery,” *European Journal of Orthopaedic Surgery and Traumatology*, vol. 29, no. 2, pp. 247–254, Feb. 2019, doi: 10.1007/S00590-019-02378-7/FIGURES/4.

[77] L. Ma and B. Fei, “Comprehensive review of surgical microscopes: technology development and medical applications,” *https://doi.org/10.1117/1.JBO.26.1.010901*, vol. 26, no. 1, p. 010901, Jan. 2021, doi: 10.1117/1.JBO.26.1.010901.

[78] K. W. Nam, J. Park, I. Y. Kim, and K. G. Kim, “Application of Stereo-Imaging Technology to Medical Field,” *Healthcare Informatics Research*, vol. 18, no. 3, pp. 158–163, Sep. 2012, doi: 10.4258/HIR.2012.18.3.158.

[79] K.-P. H. Schnitzler, K.-P. Zimmer, and H. Schnitzler, “Advances in stereomicroscopy,” *https://doi.org/10.1117/12.797409*, vol. 7100, pp. 241–252, Sep. 2008, doi: 10.1117/12.797409.

[80] "The History of Stereo Microscopy – Part III | Science Lab | Leica Microsystems." https://www.leica-microsystems.com/science-lab/the-history-of-stereo-microscopy-part-iii (accessed Apr. 22, 2022).

[81] E. E. Wilson, W. Chambers, R. Pelc, P. Nothnagle, and M. W. Davidson, "Stereomicroscopy in Neuroanatomy," *Neuromethods*, vol. 153, pp. 245–274, 2020, doi: 10.1007/978-1-0716-0428-1_9.

[82] "FusionOptics – Combines high resolution and depth of field for ideal 3D optical Images | Science Lab | Leica Microsystems." https://www.leica-microsystems.com/science-lab/fusionoptics-combines-high-resolution-and-depth-of-field-for-ideal-3d-optical-images/ (accessed Apr. 22, 2022).

[83] D. Bouget, M. Allan, D. Stoyanov, and P. Jannin, "Vision-based and marker-less surgical tool detection and tracking: a review of the literature," *Medical Image Analysis*, vol. 35. Elsevier, pp. 633–654, Jan. 01, 2017. doi: 10.1016/j.media.2016.09.003.

[84] I. Laina *et al.*, "Concurrent segmentation and localization for tracking of surgical instruments," in *Lecture Notes in Computer Science (including subseries Lecture Notes in Artificial Intelligence and Lecture Notes in Bioinformatics)*, Sep. 2017, vol. 10434 LNCS, pp. 664–672. doi: 10.1007/978-3-319-66185-8_75.

[85] B. C. Thia, N. J. Wong, and S. J. Sheth, "Video recording in ophthalmic surgery," *Survey of Ophthalmology*, vol. 64, no. 4, pp. 570–578, Jul. 2019, doi: 10.1016/J.SURVOPHTHAL.2019.01.005.

[86] H. Yamashita *et al.*, "8K ultra-high-definition microscopic camera for ophthalmic surgery," *Clinical Ophthalmology (Auckland, N.Z.)*, vol. 12, p. 1823, 2018, doi: 10.2147/OPTH.S171233.

[87] D. Huang *et al.*, "Optical Coherence Tomography," *Science (1979)*, vol. 254, no. 5035, pp. 1178–1181, 1991, Accessed: Apr. 09, 2019. [Online]. Available: https://www.ncbi.nlm.nih.gov/pmc/articles/PMC4638169/pdf/nihms692532.pdf

[88] W. Wieser, B. R. Biedermann, T. Klein, C. M. Eigenwillig, and R. Huber, "Multi-Megahertz OCT: High quality 3D imaging at 20 million A-scans and 45 GVoxels per second," *Optics Express*, vol.

18, no. 14, p. 14685, Jul. 2010, doi: 10.1364/oe.18.014685.

[89] T. Klein, W. Wieser, C. M. Eigenwillig, B. R. Biedermann, and R. Huber, "Megahertz OCT for ultrawide-field retinal imaging with a 1050nm Fourier domain mode-locked laser," *Optics Express*, vol. 19, no. 4, p. 3044, Feb. 2011, doi: 10.1364/oe.19.003044.

[90] T. Klein, W. Wieser, L. Reznicek, A. Neubauer, A. Kampik, and R. Huber, "Multi-MHz retinal OCT," *Biomedical Optics Express*, vol. 4, no. 10, p. 1890, Oct. 2013, doi: 10.1364/boe.4.001890.

[91] Y. Jian, K. Wong, and M. V. Sarunic, "Graphics processing unit accelerated optical coherence tomography processing at megahertz axial scan rate and high resolution video rate volumetric rendering," *Journal of Biomedical Optics*, vol. 18, no. 02, p. 1, Feb. 2013, doi: 10.1117/1.jbo.18.2.026002.

[92] L. Reznicek *et al.*, "Wide-field megahertz OCT imaging of patients with diabetic retinopathy," *Journal of Diabetes Research*, vol. 2015, 2015, doi: 10.1155/2015/305084.

[93] C. Torti *et al.*, "Adaptive optics optical coherence tomography at 120,000 depth scans/s for non-invasive cellular phenotyping of the living human retina," *Optics Express*, vol. 17, no. 22, p. 19382, Oct. 2009, doi: 10.1364/oe.17.019382.

[94] I. Hartl *et al.*, "Ultrahigh-resolution optical coherence tomography using continuum generation in an air–silica microstructure optical fiber," *Optics Letters*, vol. 26, no. 9, p. 608, May 2001, doi: 10.1364/ol.26.000608.

[95] W. Drexler *et al.*, "Enhanced visualization of macular pathology with the use of ultrahigh-resolution optical coherence tomography," *Archives of Ophthalmology*, vol. 121, no. 5, pp. 695–706, May 2003, doi: 10.1001/archopht.121.5.695.

[96] B. Hermann *et al.*, "Adaptive-optics ultrahigh-resolution optical coherence tomography," *Optics Letters*, vol. 29, no. 18, p. 2142, Sep. 2004, doi: 10.1364/ol.29.002142.

[97] A. Unterhuber *et al.*, "Advances in broad bandwidth light sources for ultrahigh resolution optical coherence tomography," *Physics in Medicine and Biology*, vol. 49, no. 7, pp. 1235–1246, Apr. 2004, doi: 10.1088/0031-9155/49/7/011.

[98] W. Drexler, “Ultrahigh-resolution optical coherence tomography,” *Journal of Biomedical Optics*, vol. 9, no. 1, p. 47, 2004, doi: 10.1117/1.1629679.

[99] M. Wojtkowski *et al.*, “Three-dimensional retinal imaging with high-speed ultrahigh-resolution optical coherence tomography,” *Ophthalmology*, vol. 112, no. 10, pp. 1734–1746, Oct. 2005, doi: 10.1016/j.ophtha.2005.05.023.

[100] W. Goebel and T. Kretzchmar-Gross, “Retinal thickness in diabetic retinopathy: A study using optical coherence tomography (OCT),” *Retina*, vol. 22, no. 6, pp. 759–767, Dec. 2002, doi: 10.1097/00006982-200212000-00012.

[101] R. Lattanzio *et al.*, “Macular thickness measured by optical coherence tomography (OCT) in diabetic patients,” *European Journal of Ophthalmology*, vol. 12, no. 6, pp. 482–487, Jan. 2002, doi: 10.1177/112067210201200606.

[102] T. Oshitari, K. Hanawa, and E. Adachi-Usami, “Changes of macular and RNFL thicknesses measured by Stratus OCT in patients with early stage diabetes,” *Eye*, vol. 23, no. 4, pp. 884–889, Apr. 2009, doi: 10.1038/eye.2008.119.

[103] A. Pachiyappan, U. N. Das, T. V. Murthy, and T. Rao, “Automated diagnosis of diabetic retinopathy and glaucoma using fundus and OCT images,” *Lipids in Health and Disease*, vol. 11, no. 1, pp. 1–10, Jun. 2012, doi: 10.1186/1476-511X-11-73.

[104] G. Virgili *et al.*, “Optical coherence tomography (OCT) for detection of macular oedema in patients with diabetic retinopathy,” *Cochrane Database of Systematic Reviews*, vol. 2015, no. 1, 2015, doi: 10.1002/14651858.CD008081.pub3.

[105] R. Schwartz *et al.*, “Objective Evaluation of Proliferative Diabetic Retinopathy Using OCT,” in *Ophthalmology Retina*, Feb. 2020, vol. 4, no. 2, pp. 164–174. doi: 10.1016/j.oret.2019.09.004.

[106] M. R. Hee *et al.*, “Optical coherence tomography of age-related macular degeneration and choroidal neovascularization,” *Ophthalmology*, vol. 103, no. 8, pp. 1260–1270, Aug. 1996, doi: 10.1016/S0161-6420(96)30512-5.

[107] C. V. Regatieri, L. Branchini, and J. S. Duker, “The role of spectral-domain OCT in the diagnosis

and management of neovascular age-related macular degeneration.," *Ophthalmic surgery, lasers & imaging : the official journal of the International Society for Imaging in the Eye*, vol. 42 Suppl. 2011. doi: 10.3928/15428877-20110627-05.

[108] B. Wolff, A. Matet, V. Vasseur, J. A. Sahel, and M. Mauget-Faÿsse, "En face OCT imaging for the diagnosis of outer retinal tubulations in age-related macular degeneration," *Journal of Ophthalmology*, vol. 2012, 2012, doi: 10.1155/2012/542417.

[109] L. de Sisternes, N. Simon, R. Tibshirani, T. Leng, and D. L. Rubin, "Quantitative SD-OCT imaging biomarkers as indicators of age-related macular degeneration progression," *Investigative Ophthalmology and Visual Science*, vol. 55, no. 11, pp. 7093–7103, Sep. 2014, doi: 10.1167/iovs.14-14918.

[110] S. R. Sadda *et al.*, "Consensus Definition for Atrophy Associated with Age-Related Macular Degeneration on OCT: Classification of Atrophy Report 3," *Ophthalmology*, vol. 125, no. 4, pp. 537–548, Apr. 2018, doi: 10.1016/j.ophtha.2017.09.028.

[111] J. S. Schuman *et al.*, "Optical coherence tomography: A new tool for glaucoma diagnosis," *Current Opinion in Ophthalmology*, vol. 6, no. 2, pp. 89–95, Apr. 1995, doi: 10.1097/00055735-199504000-00014.

[112] A. Giovannini, G. Amato, and C. Mariotti, "The macular thickness and volume in glaucoma: An analysis in normal and glaucomatous eyes using OCT," *Acta Ophthalmologica Scandinavica, Supplement*, vol. 80, no. 236, pp. 34–36, 2002, doi: 10.1034/j.1600-0420.80.s236.44.x.

[113] J. S. Schuman, "Spectral domain optical coherence tomography for glaucoma (an AOS thesis)," *Trans Am Ophthalmol Soc*, vol. 106, pp. 426–458, 2008.

[114] F. A. Medeiros *et al.*, "Detection of glaucoma progression with stratus OCT retinal nerve fiber layer, optic nerve head, and macular thickness measurements," *Investigative Ophthalmology and Visual Science*, vol. 50, no. 12, pp. 5741–5748, Dec. 2009, doi: 10.1167/iovs.09-3715.

[115] N. R. Kim, E. S. Lee, G. J. Seong, J. H. Kim, H. G. An, and C. Y. Kim, "Structure-function relationship and diagnostic value of macular ganglion cell complex measurement using fourier-

domain OCT in glaucoma," *Investigative Ophthalmology and Visual Science*, vol. 51, no. 9, pp. 4646–4651, Sep. 2010, doi: 10.1167/iovs.09-5053.

[116] I. I. Bussel, G. Wollstein, and J. S. Schuman, "OCT for glaucoma diagnosis, screening and detection of glaucoma progression," *British Journal of Ophthalmology*, vol. 98, no. SUPPL. 2, pp. ii15–ii19, Jul. 2014, doi: 10.1136/bjophthalmol-2013-304326.

[117] W. Jung, J. Kim, M. Jeon, E. J. Chaney, C. N. Stewart, and S. A. Boppart, "Handheld optical coherence tomography scanner for primary care diagnostics," *IEEE Transactions on Biomedical Engineering*, vol. 58, no. 3 PART 2, pp. 741–744, Mar. 2011, doi: 10.1109/TBME.2010.2096816.

[118] C. D. Lu *et al.*, "Handheld ultrahigh speed swept source optical coherence tomography instrument using a MEMS scanning mirror," *Biomedical Optics Express*, vol. 5, no. 1, p. 293, Jan. 2014, doi: 10.1364/boe.5.000293.

[119] F. Larocca, D. Nankivil, T. Dubose, C. A. Toth, S. Farsiu, and J. A. Izatt, "In vivo cellular-resolution retinal imaging in infants and children using an ultracompact handheld probe," *Nature Photonics*, vol. 10, no. 9, pp. 580–584, Aug. 2016, doi: 10.1038/nphoton.2016.141.

[120] J. Yang, L. Liu, J. P. Campbell, D. Huang, and G. Liu, "Handheld optical coherence tomography angiography," *Biomedical Optics Express*, vol. 8, no. 4, p. 2287, Apr. 2017, doi: 10.1364/boe.8.002287.

[121] J. P. Campbell *et al.*, "Handheld optical coherence tomography angiography and ultra-wide-field optical coherence tomography in retinopathy of prematurity," *JAMA Ophthalmology*, vol. 135, no. 9, pp. 977–981, Sep. 2017, doi: 10.1001/jamaophthalmol.2017.2481.

[122] J. D. Malone, M. T. El-Haddad, S. S. Yerramreddy, I. Oguz, and Y. K. Tao, "Handheld spectrally encoded coherence tomography and reflectometry for motion-corrected ophthalmic optical coherence tomography and optical coherence tomography angiography," *Neurophotonics*, vol. 6, no. 04, p. 1, Jul. 2019, doi: 10.1117/1.NPh.6.4.041102.

[123] C. Viehland *et al.*, "Ergonomic handheld OCT angiography probe optimized for pediatric and supine imaging," *Biomedical Optics Express*, vol. 10, no. 5, p. 2623, May 2019, doi:

10.1364/boe.10.002623.

[124] S. Song, K. Zhou, J. J. Xu, Q. Zhang, S. Lyu, and R. Wang, “Development of a clinical prototype of a miniature hand-held optical coherence tomography probe for prematurity and pediatric ophthalmic imaging,” 2019, doi: 10.1364/BOE.10.002383.

[125] S. A. Boppart, B. E. Bouma, C. Pitris, G. J. Tearney, J. G. Fujimoto, and M. E. Brezinski, “Forward-imaging instruments for optical coherence tomography,” *Optics Letters*, vol. 22, no. 21, p. 1618, 1997, doi: 10.1364/ol.22.001618.

[126] S. Radhakrishnan *et al.*, “Real-time optical coherence tomography of the anterior segment at 1310 nm,” *Archives of Ophthalmology*, vol. 119, no. 8, pp. 1179–1185, 2001, doi: 10.1001/archopht.119.8.1179.

[127] P. N. Dayani, R. Maldonado, S. Farsiu, and C. A. Toth, “Intraoperative use of handheld spectral domain optical coherence tomography imaging in macular surgery,” *Retina*, vol. 29, no. 10, pp. 1457–1468, Nov. 2009, doi: 10.1097/IAE.0b013e3181b266bc.

[128] Y. K. Tao, J. P. Ehlers, C. A. Toth, and J. A. Izatt, “Intraoperative spectral domain optical coherence tomography for vitreoretinal surgery,” *Optics Letters*, vol. 35, no. 20, p. 3315, Oct. 2010, doi: 10.1364/ol.35.003315.

[129] P. Hahn *et al.*, “Preclinical evaluation and intraoperative human retinal imaging with a high-resolution microscope-integrated spectral domain optical coherence tomography device,” *Retina*, vol. 33, no. 7, pp. 1328–1337, Jul. 2013, doi: 10.1097/IAE.0b013e3182831293.

[130] J. P. Ehlers, P. K. Kaiser, and S. K. Srivastava, “Intraoperative optical coherence tomography using the RESCAN 700: Preliminary results from the DISCOVER study,” *British Journal of Ophthalmology*, vol. 98, no. 10, pp. 1329–1332, Oct. 2014, doi: 10.1136/bjophthalmol-2014-305294.

[131] Y. K. Tao, S. K. Srivastava, and J. P. Ehlers, “Microscope-integrated intraoperative OCT with electrically tunable focus and heads-up display for imaging of ophthalmic surgical maneuvers,” *Biomedical Optics Express*, vol. 5, no. 6, p. 1877, Jun. 2014, doi: 10.1364/BOE.5.001877.

[132] B. Todorich *et al.*, "Impact of microscope-integrated OCT on ophthalmology resident performance of anterior segment surgical maneuvers in model eyes," *Investigative Ophthalmology and Visual Science*, vol. 57, no. 9, pp. OCT146–OCT153, Jul. 2016, doi: 10.1167/iovs.15-18818.

[133] O. M. Carrasco-Zevallos *et al.*, "Live volumetric (4D) visualization and guidance of in vivo human ophthalmic surgery with intraoperative optical coherence tomography," *Scientific Reports*, vol. 6, Aug. 2016, doi: 10.1038/srep31689.

[134] "PIONEER: Intraoperative and Perioperative OCT Study," *ClinicalTrials.gov*, 2018.

[135] "DISCOVER Study: Microscope-integrated Intraoperative OCT Study," *ClinicalTrials.gov*, 2014.

[136] R. Ray *et al.*, "Intraoperative microscope-mounted spectral domain optical coherence tomography for evaluation of retinal anatomy during macular surgery," *Ophthalmology*, vol. 118, no. 11, pp. 2212–2217, Nov. 2011, doi: 10.1016/j.ophtha.2011.04.012.

[137] J. P. Ehlers *et al.*, "The prospective intraoperative and perioperative ophthalmic imaging with optical CoherEncE TomogRaphy (PIONEER) study: 2-year results," *American Journal of Ophthalmology*, vol. 158, no. 5, pp. 999-1007.e1, Nov. 2014, doi: 10.1016/j.ajo.2014.07.034.

[138] "OPMI LUMERA 700 and RESCAN 700 | Beye." https://www.beye.com/product/opmi-lumera-700-and-rescan-700 (accessed May 05, 2021).

[139] J. P. Ehlers *et al.*, "The DISCOVER Study 3-Year Results: Feasibility and Usefulness of Microscope-Integrated Intraoperative OCT during Ophthalmic Surgery," *Ophthalmology*, vol. 125, no. 7, pp. 1014–1027, Jul. 2018, doi: 10.1016/j.ophtha.2017.12.037.

[140] J. P. Ehlers, M. P. Ohr, P. K. Kaiser, and S. K. Srivastava, "Novel microarchitectural dynamics in rhegmatogenous retinal detachments identified with intraoperative optical coherence tomography," *Retina*, vol. 33, no. 7, pp. 1428–1434, Jul. 2013, doi: 10.1097/IAE.0B013E31828396B7.

[141] J. Au, J. Goshe, W. J. Dupps, S. K. Srivastava, and J. P. Ehlers, "Intraoperative Optical Coherence Tomography for Enhanced Depth Visualization in Deep Anterior Lamellar Keratoplasty from the PIONEER Study," *Cornea*, vol. 34, no. 9, p. 1039, May 2015, doi: 10.1097/ICO.0000000000000508.

[142] V. v. Juthani, J. M. Goshe, S. K. Srivastava, and J. P. Ehlers, "The Association Between Transient Interface Fluid on Intraoperative OCT and Textural Interface Opacity Following DSAEK Surgery in the PIONEER Study," *Cornea*, vol. 33, no. 9, p. 887, 2014, doi: 10.1097/ICO.0000000000000209.

[143] P. Hahn, J. Migacz, R. O'Connell, J. A. Izatt, and C. A. Toth, "Unprocessed real-time imaging of vitreoretinal surgical maneuvers using a microscope-integrated spectral-domain optical coherence tomography system," *Graefe's Archive for Clinical and Experimental Ophthalmology*, vol. 251, no. 1, pp. 213–220, Jan. 2013, doi: 10.1007/S00417-012-2052-2/FIGURES/6.

[144] S. Binder, C. I. Falkner-Radler, C. Hauger, H. Matz, and C. Glittenberg, "Feasibility of intrasurgical spectral-domain optical coherence tomography," *Retina*, vol. 31, no. 7, pp. 1332–1336, 2011, doi: 10.1097/IAE.0b013e3182019c18.

[145] C. I. Falkner-Radler, C. Glittenberg, M. Gabriel, and S. Binder, "Intrasurgical microscopeintegrated spectral domain optical coherence Tomography-Assisted membrane peeling," *Retina*, vol. 35, no. 10, pp. 2100–2106, Oct. 2015, doi: 10.1097/IAE.0000000000000596.

[146] J. S. Titiyal, M. Kaur, S. Nair, and N. Sharma, "Intraoperative optical coherence tomography in anterior segment surgery," *Survey of Ophthalmology*, vol. 66, no. 2. Elsevier Inc., pp. 308–326, Mar. 01, 2021. doi: 10.1016/j.survophthal.2020.07.001.

[147] J. Weiss, M. Sommersperger, A. Nasseri, A. Eslami, U. Eck, and N. Navab, "Processing-Aware Real-Time Rendering for Optimized Tissue Visualization in Intraoperative 4D OCT," in *Medical Image Computing and Computer Assisted Intervention – MICCAI 2020*, Oct. 2020, vol. 12265 LNCS, pp. 267–276. doi: 10.1007/978-3-030-59722-1_26.

[148] J. G. Fujimoto, M. Wojtkowski, and R. Huber, "Fourier Domain Mode Locking (FDML): A new laser operating regime and applications for optical coherence tomography," *Optics Express, Vol. 14, Issue 8, pp. 3225-3237*, vol. 14, no. 8, pp. 3225–3237, Apr. 2006, doi: 10.1364/OE.14.003225.

[149] W. Wieser *et al.*, "Multi-Megahertz OCT: High quality 3D imaging at 20 million A-scans and 4.5 GVoxels per second," *Optics Express, Vol. 18, Issue 14, pp. 14685-14704*, vol. 18, no. 14, pp.

14685–14704, Jul. 2010, doi: 10.1364/OE.18.014685.

[150] J. P. Kolb *et al.*, "Live video rate volumetric OCT imaging of the retina with multi-MHz A-scan rates," *PLoS ONE*, vol. 14, no. 3, p. e0213144, Mar. 2019, doi: 10.1371/journal.pone.0213144.

[151] M. Göb *et al.*, "Continuous spectral zooming for in vivo live 4D-OCT with MHz A-scan rates and long coherence," *Biomedical Optics Express, Vol. 13, Issue 2, pp. 713-727*, vol. 13, no. 2, pp. 713–727, Feb. 2022, doi: 10.1364/BOE.448353.

[152] H.-C. Park *et al.*, "Lissajous fiber scanning for forward viewing optical endomicroscopy using asymmetric stiffness modulation," *Optics Express, Vol. 22, Issue 5, pp. 5818-5825*, vol. 22, no. 5, pp. 5818–5825, Mar. 2014, doi: 10.1364/OE.22.005818.

[153] L. Huo *et al.*, "Forward-viewing resonant fiber-optic scanning endoscope of appropriate scanning speed for 3D OCT imaging," *Optics Express, Vol. 18, Issue 14, pp. 14375-14384*, vol. 18, no. 14, pp. 14375–14384, Jul. 2010, doi: 10.1364/OE.18.014375.

[154] O. M. Carrasco-Zevallos, C. Viehland, B. Keller, R. P. McNabb, A. N. Kuo, and J. A. Izatt, "Constant linear velocity spiral scanning for near video rate 4D OCT ophthalmic and surgical imaging with isotropic transverse sampling," *Biomedical Optics Express*, vol. 9, no. 10, p. 5052, Oct. 2018, doi: 10.1364/boe.9.005052.

[155] S. Ricco, M. Chen, H. Ishikawa, G. Wollstein, and J. Schuman, "Correcting Motion Artifacts in Retinal Spectral Domain Optical Coherence Tomography via Image Registration," *Med Image Comput Comput Assist Interv*, vol. 12, no. Pt 1, p. 100, 2009, doi: 10.1007/978-3-642-04268-3_13.

[156] S. Martinez-Conde, S. L. Macknik, and D. H. Hubel, "The role of fixational eye movements in visual perception," *Nat Rev Neurosci*, vol. 5, no. 3, pp. 229–240, 2004, doi: 10.1038/NRN1348.

[157] S. H. Yun, G. J. Tearney, J. F. de Boer, and B. E. Bouma, "Motion artifacts in optical coherence tomography with frequency-domain ranging," *Opt Express*, vol. 12, no. 13, p. 2977, 2004, doi: 10.1364/OPEX.12.002977.

[158] M. Gora *et al.*, "Ultra high-speed swept source OCT imaging of the anterior segment of human eye at 200 kHz with adjustable imaging range," *Optics Express, Vol. 17, Issue 17, pp. 14880-14894*, vol.

17, no. 17, pp. 14880–14894, Aug. 2009, doi: 10.1364/OE.17.014880.

[159] Y. Chen, Y.-J. Hong, S. Makita, and Y. Yasuno, "Three-dimensional eye motion correction by Lissajous scan optical coherence tomography," *Biomedical Optics Express*, vol. 8, no. 3, p. 1783, Mar. 2017, doi: 10.1364/boe.8.001783.

[160] Y. Chen, Y.-J. Hong, S. Makita, and Y. Yasuno, "Eye-motion-corrected optical coherence tomography angiography using Lissajous scanning," *Biomedical Optics Express*, vol. 9, no. 3, p. 1111, Mar. 2018, doi: 10.1364/boe.9.001111.

[161] S. Makita, M. Miura, S. Azuma, T. Mino, T. Yamaguchi, and Y. Yasuno, "Accurately motion-corrected Lissajous OCT with multi-type image registration," *Biomedical Optics Express*, vol. 12, no. 1, p. 637, Jan. 2021, doi: 10.1364/boe.409004.

[162] M. F. Kraus *et al.*, "Motion correction in optical coherence tomography volumes on a per A-scan basis using orthogonal scan patterns," *Biomedical Optics Express*, vol. 3, no. 6, pp. 1182–1199, Jun. 2012, doi: 10.1364/BOE.3.001182.

[163] M. Pircher, B. Baumann, E. Götzinger, H. Sattmann, and C. K. Hitzenberger, "Simultaneous SLO/OCT imaging of the human retina with axial eye motion correction," *Optics Express*, vol. 15, no. 25, p. 16922, Dec. 2007, doi: 10.1364/oe.15.016922.

[164] M. Pircher, E. Götzinger, H. Sattmann, R. A. Leitgeb, and C. K. Hitzenberger, "In vivo investigation of human cone photoreceptors with SLO/OCT in combination with 3D motion correction on a cellular level," *Optics Express*, vol. 18, no. 13, p. 13935, Jun. 2010, doi: 10.1364/oe.18.013935.

[165] K. V. Vienola *et al.*, "Real-time eye motion compensation for OCT imaging with tracking SLO," *Biomedical Optics Express*, vol. 3, no. 11, p. 2950, Nov. 2012, doi: 10.1364/boe.3.002950.

[166] F. Schwarzhans *et al.*, "Generating large field of view en-face projection images from intra-acquisition motion compensated volumetric optical coherence tomography data," *Biomedical Optics Express*, vol. 11, no. 12, pp. 6881–6904, Oct. 2020, doi: 10.1364/boe.404738.

[167] A. G. Podoleanu and D. A. Jackson, "Combined optical coherence tomograph and scanning laser ophthalmoscope," *Electronics Letters*, vol. 34, no. 11, pp. 1088–1090, May 1998, doi:

10.1049/el:19980793.

[168] A. Gh. Podoleanu, G. M. Dobre, R. G. Cucu, and R. B. Rosen, “Sequential optical coherence tomography and confocal imaging,” *Optics Letters*, vol. 29, no. 4, p. 364, Feb. 2004, doi: 10.1364/ol.29.000364.

[169] D. X. Hammer, N. v. Iftimia, T. E. Ustun, J. C. Magill, and R. D. Ferguson, “Dual OCT/SLO imager with three-dimensional tracker,” in *Ophthalmic Technologies XV*, Apr. 2005, vol. 5688, no. 18, p. 33. doi: 10.1117/12.592762.

[170] N. v. Iftimia, D. X. Hammer, C. E. Bigelow, T. Ustun, J. F. de Boer, and R. D. Ferguson, “Hybrid retinal imager using line-scanning laser ophthalmoscopy and spectral domain optical coherence tomography,” *Optics Express*, vol. 14, no. 26, p. 12909, Dec. 2006, doi: 10.1364/oe.14.012909.

[171] D. X. Hammer, R. D. Ferguson, T. E. Ustun, C. E. Bigelow, N. v. Iftimia, and R. H. Webb, “Line-scanning laser ophthalmoscope,” *Journal of Biomedical Optics*, vol. 11, no. 4, p. 041126, 2006, doi: 10.1117/1.2335470.

[172] J. D. Malone *et al.*, “Simultaneous multimodal ophthalmic imaging using swept-source spectrally encoded scanning laser ophthalmoscopy and optical coherence tomography,” *Biomedical Optics Express*, vol. 8, no. 1, p. 193, Jan. 2017, doi: 10.1364/BOE.8.000193.

[173] M. T. El-Haddad, I. Bozic, and Y. K. Tao, “Spectrally encoded coherence tomography and reflectometry: Simultaneous en face and cross-sectional imaging at 2 gigapixels per second,” *Journal of Biophotonics*, vol. 11, no. 4, 2018, doi: 10.1002/jbio.201700268.

[174] Y. K. Tao and J. A. Izatt, “Spectrally encoded confocal scanning laser ophthalmoscopy,” *Optics Letters*, vol. 35, no. 4, p. 574, Feb. 2010, doi: 10.1364/ol.35.000574.

[175] Y. K. Tao, S. Farsiu, and J. A. Izatt, “Interlaced spectrally encoded confocal scanning laser ophthalmoscopy and spectral domain optical coherence tomography,” *Biomedical Optics Express*, vol. 1, no. 2, p. 431, Sep. 2010, doi: 10.1364/BOE.1.000431.

[176] P. Hahn *et al.*, “Intrasurgical human retinal imaging with manual instrument tracking using a microscope-integrated spectral-domain optical coherence tomography device,” *Translational Vision*

Science and Technology, vol. 4, no. 4, pp. 1–9, Jul. 2015, doi: 10.1167/tvst.4.4.1.

[177] B. Keller *et al.*, "Real-time corneal segmentation and 3D needle tracking in intrasurgical OCT," *Biomedical Optics Express*, vol. 9, no. 6, p. 2716, Jun. 2018, doi: 10.1364/boe.9.002716.

[178] N. Gessert, M. Schlüter, and A. Schlaefer, "A deep learning approach for pose estimation from volumetric OCT data," *Medical Image Analysis*, vol. 46, pp. 162–179, Mar. 2018, doi: 10.1016/j.media.2018.03.002.

[179] J. Weiss, N. Rieke, M. A. Nasseri, M. Maier, A. Eslami, and N. Navab, "Fast 5DOF needle tracking in iOCT," *International Journal of Computer Assisted Radiology and Surgery*, vol. 13, no. 6, pp. 787–796, Mar. 2018, doi: 10.1007/s11548-018-1751-5.

[180] M. Zhou *et al.*, "6DOF Needle Pose Estimation for Robot-Assisted Vitreoretinal Surgery," *IEEE Access*, vol. 7, pp. 63113–63122, 2019, doi: 10.1109/ACCESS.2019.2912327.

[181] D. Stoyanov, "Surgical vision," *Annals of Biomedical Engineering*, vol. 40, no. 2, pp. 332–345, Feb. 2012, doi: 10.1007/s10439-011-0441-z.

[182] W. Liu, H. Ren, W. Zhang, and S. Song, "Cognitive tracking of surgical instruments based on stereo vision and depth sensing," in *2013 IEEE International Conference on Robotics and Biomimetics, ROBIO 2013*, 2013, pp. 316–321. doi: 10.1109/ROBIO.2013.6739478.

[183] Z. Zhou, B. Wu, J. Duan, X. Zhang, N. Zhang, and Z. Liang, "Optical surgical instrument tracking system based on the principle of stereo vision," *Journal of Biomedical Optics*, vol. 22, no. 6, p. 065005, Jun. 2017, doi: 10.1117/1.jbo.22.6.065005.

[184] M. T. El-Haddad and Y. K. Tao, "Automated stereo vision instrument tracking for intraoperative OCT guided anterior segment ophthalmic surgical maneuvers," *Biomedical Optics Express*, vol. 6, no. 8, p. 3014, 2015, doi: 10.1364/boe.6.003014.

[185] Z. Zhao, S. Voros, Y. Weng, F. Chang, and R. Li, "Tracking-by-detection of surgical instruments in minimally invasive surgery via the convolutional neural network deep learning-based method," *Computer Assisted Surgery*, vol. 22, pp. 26–35, Oct. 2017, doi: 10.1080/24699322.2017.1378777.

[186] L. Qiu, C. Li, and H. Ren, "Real-time surgical instrument tracking in robot-assisted surgery using

multi-domain convolutional neural network," in *Healthcare Technology Letters*, 2019, vol. 6, no. 6, pp. 159–164. doi: 10.1049/htl.2019.0068.

[187] Z. Zhao, Z. Chen, S. Voros, and X. Cheng, "Real-time tracking of surgical instruments based on spatio-temporal context and deep learning," *Computer Assisted Surgery*, vol. 24, no. sup1, pp. 20–29, Oct. 2019, doi: 10.1080/24699322.2018.1560097.

[188] R. Sznitman, R. Richa, R. H. Taylor, B. Jedynak, and G. D. Hager, "Unified detection and tracking of instruments during retinal microsurgery," *IEEE Transactions on Pattern Analysis and Machine Intelligence*, vol. 35, no. 5, pp. 1263–1273, 2013, doi: 10.1109/TPAMI.2012.209.

[189] Y. Li, C. Chen, X. Huang, and J. Huang, "Instrument tracking via online learning in retinal microsurgery," in *Medical Image Computing and Computer-Assisted Intervention – MICCAI 2014*, 2014, vol. 8673 LNCS, no. PART 1, pp. 464–471. doi: 10.1007/978-3-319-10404-1_58.

[190] R. Richa, M. Balicki, E. Meisner, R. Sznitman, R. Taylor, and G. Hager, "Visual tracking of surgical tools for proximity detection in retinal surgery," in *Information Processing in Computer-Assisted Interventions*, 2011, vol. 6689 LNCS, pp. 55–66. doi: 10.1007/978-3-642-21504-9_6.

[191] J. B. West and C. R. Maurer, "Designing optically tracked instruments for image-guided surgery," *IEEE Transactions on Medical Imaging*, vol. 23, no. 5, pp. 533–545, 2004, doi: 10.1109/TMI.2004.825614.

[192] Z. Zhou, B. Wu, J. Duan, X. Zhang, N. Zhang, and Z. Liang, "Optical surgical instrument tracking system based on the principle of stereo vision," *Journal of Biomedical Optics*, vol. 22, no. 6, p. 065005, Jun. 2017, doi: 10.1117/1.jbo.22.6.065005.

[193] J. D. Malone *et al.*, "Simultaneous multimodal ophthalmic imaging using swept-source spectrally encoded scanning laser ophthalmoscopy and optical coherence tomography," *Biomedical Optics Express*, vol. 8, no. 1, p. 193, Jan. 2017, doi: 10.1364/boe.8.000193.

[194] M. Guizar-Sicairos, S. T. Thurman, and J. R. Fienup, "Efficient subpixel image registration algorithms," *Optics Letters*, vol. 33, no. 2, p. 156, Jan. 2008, doi: 10.1364/ol.33.000156.

[195] M. R. Munk *et al.*, "OCT-angiography: A qualitative and quantitative comparison of 4 OCT-A

devices," *PLOS ONE*, vol. 12, no. 5, p. e0177059, May 2017, doi: 10.1371/journal.pone.0177059.

[196] I. Oguz, J. Malone, Y. Atay, and Y. K. Tao, "Self-fusion for OCT noise reduction," in *Proceedings of the SPIE*, Mar. 2020, vol. 11313, p. 11. doi: 10.1117/12.2549472.

[197] "GitHub - pyushkevich/greedy: Very fast greedy diffeomorphic registration code." https://github.com/pyushkevich/greedy (accessed May 06, 2021).

[198] E. Tang and Y. Tao, "Modeling and optimization of galvanometric point-scanning temporal dynamics," *Biomedical Optics Express*, vol. 12, no. 11, pp. 6701–6716, Nov. 2021, doi: 10.1364/boe.430586.

[199] M. Minsky, "Memoir on inventing the confocal scanning microscope," *Scanning*, vol. 10, no. 4, pp. 128–138, Jan. 1988, doi: 10.1002/sca.4950100403.

[200] W. Denk, J. H. Strickler, and W. W. Webb, "Two-photon laser scanning fluorescence microscopy," *Science (1979)*, vol. 248, no. 4951, pp. 73–76, Apr. 1990, doi: 10.1126/science.2321027.

[201] A. H. Voie, D. H. Burns, and F. A. Spelman, "Orthogonal-plane fluorescence optical sectioning: Three-dimensional imaging of macroscopic biological specimens," *Journal of Microscopy*, vol. 170, no. 3, pp. 229–236, Jun. 1993, doi: 10.1111/j.1365-2818.1993.tb03346.x.

[202] J. Huisken, J. Swoger, F. Del Bene, J. Wittbrodt, and E. H. K. Stelzer, "Optical sectioning deep inside live embryos by selective plane illumination microscopy," *Science (1979)*, vol. 305, no. 5686, pp. 1007–1009, Aug. 2004, doi: 10.1126/science.1100035.

[203] J. Liang, D. R. Williams, and D. T. Miller, "Supernormal vision and high-resolution retinal imaging through adaptive optics," *Journal of the Optical Society of America A*, vol. 14, no. 11, p. 2884, Nov. 1997, doi: 10.1364/josaa.14.002884.

[204] A. Roorda, F. Romero-Borja, W. J. Donnelly III, H. Queener, T. J. Hebert, and M. C. W. Campbell, "Adaptive optics scanning laser ophthalmoscopy," *Optics Express*, vol. 10, no. 9, p. 405, May 2002, doi: 10.1364/OE.10.000405.

[205] R. H. Webb, G. W. Hughes, and F. C. Delori, "Confocal scanning laser ophthalmoscope," *Applied Optics*, vol. 26, no. 8, p. 1492, Apr. 1987, doi: 10.1364/ao.26.001492.

[206] M. W. Seeliger *et al.*, “In vivo confocal imaging of the retina in animal models using scanning laser ophthalmoscopy,” in *Vision Research*, Dec. 2005, vol. 45, no. 28, pp. 3512–3519. doi: 10.1016/j.visres.2005.08.014.

[207] M. L. Stitch, E. J. Woodbury, and J. H. Morse, “Optical ranging system uses laser transmitter,” *Electronics (Basel)*, vol. 34, pp. 51–53, 1961.

[208] N. J. Mankovich, A. M. Cheeseman, and N. G. Stoker, “The display of three-dimensional anatomy with stereolithographic models,” *Journal of Digital Imaging*, vol. 3, no. 3, pp. 200–203, 1990, doi: 10.1007/BF03167610.

[209] R. Leyden, T. Almouist, M. Lewis, and H. Nguyen, “Stereolithography method and apparatus,” Jun. 12, 1992

[210] Y. Bae, D. Soane, and C. Charles, “Rapid prototype three dimensional stereolithography,” May 27, 1993

[211] J. Allison, C. Childers, and C. Hull, “Method of making a three-dimensional object by stereolithography,” Jun. 25, 1993

[212] G. Y. Fan, H. Fujisaki, A. Miyawaki, R. K. Tsay, R. Y. Tsien, and M. H. Ellisman, “Video-rate scanning two-photon excitation fluorescence microscopy and ratio imaging with cameleons,” *Biophysical Journal*, vol. 76, no. 5, pp. 2412–2420, May 1999, doi: 10.1016/S0006-3495(99)77396-0.

[213] H. Miyajima *et al.*, “A mems electromagnetic optical scanner for a commercial confocal laser scanning microscope,” *Journal of Microelectromechanical Systems*, vol. 12, no. 3, pp. 243–251, 2003, doi: 10.1109/JMEMS.2003.809961.

[214] A. D. L. Humphris, M. J. Miles, and J. K. Hobbs, “A mechanical microscope: High-speed atomic force microscopy,” *Applied Physics Letters*, vol. 86, no. 3, pp. 1–3, Jan. 2005, doi: 10.1063/1.1855407.

[215] W. Wieser, W. Draxinger, T. Klein, S. Karpf, T. Pfeiffer, and R. Huber, “High definition live 3D-OCT in vivo: design and evaluation of a 4D OCT engine with 1 GVoxel/s,” *Biomedical Optics*

Express, vol. 5, no. 9, p. 2963, Sep. 2014, doi: 10.1364/boe.5.002963.

[216] J. Huisken and D. Y. R. Stainier, "Even fluorescence excitation by multidirectional selective plane illumination microscopy (mSPIM)," *Optics Letters*, vol. 32, no. 17, p. 2608, Sep. 2007, doi: 10.1364/ol.32.002608.

[217] D. X. Hammer, R. D. Ferguson, C. E. Bigelow, N. V. Iftimia, T. E. Ustun, and S. A. Burns, "Adaptive optics scanning laser ophthalmoscope for stabilized retinal imaging," *Optics Express*, vol. 14, no. 8, p. 3354, Apr. 2006, doi: 10.1364/oe.14.003354.

[218] A. Dubra and Y. Sulai, "Reflective afocal broadband adaptive optics scanning ophthalmoscope," *Biomedical Optics Express*, vol. 2, no. 6, p. 1757, Jun. 2011, doi: 10.1364/boe.2.001757.

[219] Y. Geng *et al.*, "Adaptive optics retinal imaging in the living mouse eye," *Biomedical Optics Express*, vol. 3, no. 4, p. 715, Apr. 2012, doi: 10.1364/boe.3.000715.

[220] S. T. S. Holmström, U. Baran, and H. Urey, "MEMS laser scanners: A review," *Journal of Microelectromechanical Systems*, vol. 23, no. 2. Institute of Electrical and Electronics Engineers Inc., pp. 259–275, 2014. doi: 10.1109/JMEMS.2013.2295470.

[221] H. Urey, "Torsional MEMS scanner design for high-resolution scanning display systems," in *Optical Scanning 2002*, Jun. 2002, vol. 4773, no. 4, p. 27. doi: 10.1117/12.469198.

[222] D. G. Tweed, "Resonant Scanner Linearization Techniques," *Optical Engineering*, vol. 24, no. 6, p. 241018, Dec. 1985, doi: 10.1117/12.7973621.

[223] J. Khoury, "Mapping approach for image correction and processing for bidirectional resonant scanners," *Optical Engineering*, vol. 46, no. 2, p. 027007, Feb. 2007, doi: 10.1117/1.2434767.

[224] L. Xu, X. Tian, X. Li, G. Shang, and J. Yao, "Geometric distortion correction for sinusoidally scanned images," *Measurement Science and Technology*, vol. 22, no. 11, p. 114023, Oct. 2011, doi: 10.1088/0957-0233/22/11/114023.

[225] Q. Yang *et al.*, "Calibration-free sinusoidal rectification and uniform retinal irradiance in scanning light ophthalmoscopy," *Optics Letters*, vol. 40, no. 1, p. 85, Jan. 2015, doi: 10.1364/ol.40.000085.

[226] M. Rajadhyaksha, R. R. Anderson, and R. H. Webb, "Video-rate confocal scanning laser microscope

for imaging human tissues in vivo," *Applied Optics*, vol. 38, no. 10, p. 2105, Apr. 1999, doi: 10.1364/ao.38.002105.

[227] K. H. Kim, C. Buehler, and P. T. C. So, "High-speed, two-photon scanning microscope," *Applied Optics*, vol. 38, no. 28, p. 6004, Oct. 1999, doi: 10.1364/ao.38.006004.

[228] Y. X. Li *et al.*, "Flexible polygon-mirror based laser scanning microscope platform for multiphoton in-vivo imaging," *Journal of Biophotonics*, vol. 10, no. 11, pp. 1526–1537, Nov. 2017, doi: 10.1002/jbio.201600289.

[229] V.-F. Duma and A. G. Podoleanu, "Polygon mirror scanners in biomedical imaging: a review," in *Optical Components and Materials X*, Mar. 2013, vol. 8621, no. 11, p. 86210V. doi: 10.1117/12.2005065.

[230] M. B. Bouchard *et al.*, "Swept confocally-aligned planar excitation (SCAPE) microscopy for high-speed volumetric imaging of behaving organisms," *Nature Photonics*, vol. 9, no. 2, pp. 113–119, Feb. 2015, doi: 10.1038/nphoton.2014.323.

[231] D. P. Biss *et al.*, "In vivo fluorescent imaging of the mouse retina using adaptive optics," *Optics Letters*, vol. 32, no. 6, p. 659, Mar. 2007, doi: 10.1364/ol.32.000659.

[232] G. F. Marshall and G. E. Stutz, *Handbook of Optical and Laser Scanning*. CRC Press, 2018. doi: 10.1201/9781315218243.

[233] R. Salomé *et al.*, "Ultrafast random-access scanning in two-photon microscopy using acousto-optic deflectors," *Journal of Neuroscience Methods*, vol. 154, no. 1–2, pp. 161–174, Jun. 2006, doi: 10.1016/j.jneumeth.2005.12.010.

[234] T. Vettenburg *et al.*, "Light-sheet microscopy using an Airy beam," *Nature Methods*, vol. 11, no. 5, pp. 541–544, Apr. 2014, doi: 10.1038/nmeth.2922.

[235] M. Duocastella, G. Sancataldo, P. Saggau, P. Ramoino, P. Bianchini, and A. Diaspro, "Fast Inertia-Free Volumetric Light-Sheet Microscope," *ACS Photonics*, vol. 4, no. 7, pp. 1797–1804, Jul. 2017, doi: 10.1021/acsphotonics.7b00382.

[236] G. R. B. E. Römer and P. Bechtold, "Electro-optic and acousto-optic laser beam scanners," in

Physics Procedia, 2014, vol. 56, no. C, pp. 29–39. doi: 10.1016/j.phpro.2014.08.092.

[237] V. Iyer, B. E. Losavio, and P. Saggau, "Compensation of spatial and temporal dispersion for acousto-optic multiphoton laser-scanning microscopy," *Journal of Biomedical Optics*, vol. 8, no. 3, p. 460, 2003, doi: 10.1117/1.1580827.

[238] T. Takamatsu and S. Fujita, "Microscopic tomography by laser scanning microscopy and its three-dimensional reconstruction," *Journal of Microscopy*, vol. 149, no. 3, pp. 167–174, Mar. 1988, doi: 10.1111/j.1365-2818.1988.tb04574.x.

[239] R. H. Webb, "Confocal optical microscopy," *Reports on Progress in Physics*, vol. 59, no. 3, pp. 427–471, Mar. 1996, doi: 10.1088/0034-4885/59/3/003.

[240] J. Mertz, "Nonlinear microscopy: New techniques and applications," *Current Opinion in Neurobiology*, vol. 14, no. 5. Elsevier Current Trends, pp. 610–616, Oct. 01, 2004. doi: 10.1016/j.conb.2004.08.013.

[241] W. Choi *et al.*, "Tomographic phase microscopy," *Nature Methods*, vol. 4, no. 9, pp. 717–719, Sep. 2007, doi: 10.1038/nmeth1078.

[242] R. P. Aylward, "Advanced galvanometer-based optical scanner design," *Sensor Review*, vol. 23, no. 3. MCB UP Ltd, pp. 216–222, 2003. doi: 10.1108/02602280310481968.

[243] H. W. Yoo, S. Ito, and G. Schitter, "High speed laser scanning microscopy by iterative learning control of a galvanometer scanner," *Control Engineering Practice*, vol. 50, pp. 12–21, May 2016, doi: 10.1016/j.conengprac.2016.02.007.

[244] A. Kasturi, V. Milanović, F. Hu, and H. J. Kim, "Iterative learning control (ILC) algorithm for greatly increased bandwidth and linearity of MEMS mirrors in LiDAR and related imaging applications," in *MOEMS and Miniaturized Systems XVII*, Feb. 2018, vol. 10545, p. 37. doi: 10.1117/12.2291428.

[245] J. P. Giannini, A. G. York, and H. Shroff, "Anticipating, measuring, and minimizing MEMS mirror scan error to improve laser scanning microscopy's speed and accuracy," *PLoS ONE*, vol. 12, no. 10, 2017, doi: 10.1371/journal.pone.0185849.

[246] V.-F. Duma, “Optimal scanning function of a galvanometer scanner for an increased duty cycle,” *Optical Engineering*, vol. 49, no. 10, p. 103001, Oct. 2010, doi: 10.1117/1.3497570.

[247] V. F. Duma, K. S. Lee, P. Meemon, and J. P. Rolland, “Experimental investigations of the scanning functions of galvanometer-based scanners with applications in OCT,” *Applied Optics*, vol. 50, no. 29, pp. 5735–5749, Oct. 2011, doi: 10.1364/AO.50.005735.

[248] V.-F. Duma, P. Tankam, J. Huang, J. Won, and J. P. Rolland, “Optimization of galvanometer scanning for optical coherence tomography,” *Applied Optics*, vol. 54, no. 17, p. 5495, Jun. 2015, doi: 10.1364/ao.54.005495.

[249] J. G. Ziegler, N. B. Nichols, and others, “Optimum settings for automatic controllers,” *trans. ASME*, vol. 64, no. 11, 1942.

[250] C. Knospe, “PID control,” *IEEE Control Systems Magazine*, vol. 26, no. 1, pp. 30–31, 2006, doi: 10.1109/MCS.2006.1580151.

[251] Y. Li, K. H. Ang, and G. C. Y. Chong, “PID Control System Analysis and Design: Problems, Remedies, and Future Directions,” *IEEE Control Systems Magazine*, vol. 26, no. 1, pp. 32–41, 2006, doi: 10.1109/MCS.2006.1580152.

[252] R. F. Spaide, J. G. Fujimoto, N. K. Waheed, S. R. Sadda, and G. Staurenghi, “Optical coherence tomography angiography,” *Progress in Retinal and Eye Research*, vol. 64. Elsevier Ltd, pp. 1–55, May 01, 2018. doi: 10.1016/j.preteyeres.2017.11.003.

[253] J. Jantzen and C. Jakobsen, “Turning PID controller tuning into a simple consideration of settling time,” in *2016 European Control Conference, ECC 2016*, Jan. 2017, pp. 370–375. doi: 10.1109/ECC.2016.7810313.

[254] C. E. Rasmussen and C. K. I. Williams, “Gaussian Processes for Machine Learning.”

[255] E. Schulz, M. Speekenbrink, and A. Krause, “A tutorial on Gaussian process regression: Modelling, exploring, and exploiting functions,” *Journal of Mathematical Psychology*, vol. 85, pp. 1–16, Aug. 2018, doi: 10.1016/j.jmp.2018.03.001.

[256] N. Cressie and H. C. Huang, “Classes of Nonseparable, Spatio-Temporal Stationary Covariance

Functions," *J Am Stat Assoc*, vol. 94, no. 448, pp. 1330–1339, Dec. 1999, doi: 10.1080/01621459.1999.10473885.

[257] E. M. Tang, M. T. El-Haddad, S. N. Patel, and Y. K. Tao, "Automated instrument-tracking for 4D video-rate imaging of ophthalmic surgical maneuvers," *Biomedical Optics Express, Vol. 13, Issue 3, pp. 1471-1484*, vol. 13, no. 3, pp. 1471–1484, Mar. 2022, doi: 10.1364/BOE.450814.

[258] T. Peters, B. Davey, P. Munger, R. Comeau, A. Evans, and A. Olivier, "Three-dimensional multimodal image-guidance for neurosurgery," *IEEE Transactions on Medical Imaging*, vol. 15, no. 2, pp. 121–128, 1996, doi: 10.1109/42.491414.

[259] R. B. Schwartz *et al.*, "Intraoperative MR imaging guidance for intracranial neurosurgery: Experience with the first 200 cases," *Radiology*, vol. 211, no. 2, pp. 477–488, May 1999, doi: 10.1148/radiology.211.2.r99ma26477.

[260] R. M. Comeau, A. F. Sadikot, A. Fenster, and T. M. Peters, "Intraoperative ultrasound for guidance and tissue shift correction in image-guided neurosurgery," *Medical Physics*, vol. 27, no. 4, pp. 787–800, Apr. 2000, doi: 10.1118/1.598942.

[261] E. Martin, D. Jeanmonod, A. Morel, E. Zadicario, and B. Werner, "High-intensity focused ultrasound for noninvasive functional neurosurgery," *Annals of Neurology*, vol. 66, no. 6, pp. 858–861, Dec. 2009, doi: 10.1002/ana.21801.

[262] P. N. Dayani, R. Maldonado, S. Farsiu, and C. A. Toth, "Intraoperative use of handheld spectral domain optical coherence tomography imaging in macular surgery," *Retina*, vol. 29, no. 10, pp. 1457–1468, Nov. 2009, doi: 10.1097/IAE.0b013e3181b266bc.

[263] Y. K. Tao, J. P. Ehlers, C. A. Toth, and J. A. Izatt, "Intraoperative spectral domain optical coherence tomography for vitreoretinal surgery," *Optics Letters*, vol. 35, no. 20, p. 3315, Oct. 2010, doi: 10.1364/ol.35.003315.

[264] J. P. Ehlers, Y. K. Tao, and S. K. Srivastava, "The value of intraoperative optical coherence tomography imaging in vitreoretinal surgery," *Current Opinion in Ophthalmology*, vol. 25, no. 3. NIH Public Access, pp. 221–227, 2014. doi: 10.1097/ICU.0000000000000044.

[265] D. M. Cash *et al.*, "Concepts and preliminary data toward the realization of image-guided liver surgery," *Journal of Gastrointestinal Surgery*, vol. 11, no. 7, pp. 844–859, Jul. 2007, doi: 10.1007/s11605-007-0090-6.

[266] T. Aoki *et al.*, "Image-guided liver mapping using fluorescence navigation system with indocyanine green for anatomical hepatic resection," *World Journal of Surgery*, vol. 32, no. 8, pp. 1763–1767, Aug. 2008, doi: 10.1007/s00268-008-9620-y.

[267] M. Peterhans *et al.*, "A navigation system for open liver surgery: Design, workflow and first clinical applications," *International Journal of Medical Robotics and Computer Assisted Surgery*, vol. 7, no. 1, pp. 7–16, Mar. 2011, doi: 10.1002/rcs.360.

[268] L. A. Dawson and D. A. Jaffray, "Advances in image-guided radiation therapy," *Journal of Clinical Oncology*, vol. 25, no. 8. American Society of Clinical Oncology, pp. 938–946, Mar. 10, 2007. doi: 10.1200/JCO.2006.09.9515.

[269] O. A. J. van der Meijden and M. P. Schijven, "The value of haptic feedback in conventional and robot-assisted minimal invasive surgery and virtual reality training: A current review," *Surgical Endoscopy*, vol. 23, no. 6. Springer, pp. 1180–1190, 2009. doi: 10.1007/s00464-008-0298-x.

[270] M. T. El-Haddad and Y. K. Tao, "Advances in intraoperative optical coherence tomography for surgical guidance," *Current Opinion in Biomedical Engineering*, vol. 3. Elsevier B.V., pp. 37–48, Sep. 01, 2017. doi: 10.1016/j.cobme.2017.09.007.

[271] P. Yee *et al.*, "iOCT-assisted macular hole surgery: Outcomes and utility from the DISCOVER study," *British Journal of Ophthalmology*, vol. 105, no. 3, pp. 403–409, Mar. 2021, doi: 10.1136/bjophthalmol-2020-316045.

[272] O. M. Carrasco-Zevallos *et al.*, "Review of intraoperative optical coherence tomography: technology and applications [Invited]," *Biomedical Optics Express*, vol. 8, no. 3, p. 1607, 2017, doi: 10.1364/BOE.8.001607.

[273] J. P. Ehlers, P. K. Kaiser, and S. K. Srivastava, "Intraoperative optical coherence tomography using the RESCAN 700: Preliminary results from the DISCOVER study," *British Journal of*

Ophthalmology, vol. 98, no. 10, pp. 1329–1332, Oct. 2014, doi: 10.1136/bjophthalmol-2014-305294.

[274] A. Runkle, S. K. Srivastava, and J. P. Ehlers, "Microscope-integrated OCT feasibility and utility with the enfocus system in the discover study," *Ophthalmic Surgery Lasers and Imaging Retina*, vol. 48, no. 3, pp. 216–222, Mar. 2017, doi: 10.3928/23258160-20170301-04.

[275] O. M. Carrasco-Zevallos *et al.*, "Optical coherence tomography for retinal surgery: Perioperative analysis to real-time four-dimensional image-guided surgery," *Investigative Ophthalmology and Visual Science*, vol. 57, no. 9, pp. OCT37–OCT50, Jul. 2016, doi: 10.1167/iovs.16-19277.

[276] O. M. Carrasco-Zevallos *et al.*, "Live volumetric (4D) visualization and guidance of in vivo human ophthalmic surgery with intraoperative optical coherence tomography," *Scientific Reports*, vol. 6, no. 1, pp. 1–16, Aug. 2016, doi: 10.1038/srep31689.

[277] C. Viehland *et al.*, "Enhanced volumetric visualization for real time 4D intraoperative ophthalmic swept-source OCT," *Biomedical Optics Express*, vol. 7, no. 5, p. 1815, May 2016, doi: 10.1364/boe.7.001815.

[278] O. M. Carrasco-Zevallos, C. Viehland, B. Keller, R. P. McNabb, A. N. Kuo, and J. A. Izatt, "Constant linear velocity spiral scanning for near video rate 4D OCT ophthalmic and surgical imaging with isotropic transverse sampling," *Biomedical Optics Express*, vol. 9, no. 10, p. 5052, Oct. 2018, doi: 10.1364/boe.9.005052.

[279] J. P. Kolb *et al.*, "Live video rate volumetric OCT imaging of the retina with multi-MHz A-scan rates," *PLoS ONE*, vol. 14, no. 3, p. e0213144, Mar. 2019, doi: 10.1371/journal.pone.0213144.

[280] J. P. Ehlers *et al.*, "The prospective intraoperative and perioperative ophthalmic imaging with optical CoherEncE TomogRaphy (PIONEER) study: 2-year results," *American Journal of Ophthalmology*, vol. 158, no. 5, pp. 999-1007.e1, Nov. 2014, doi: 10.1016/j.ajo.2014.07.034.

[281] M. T. El-Haddad and Y. K. Tao, "Automated stereo vision instrument tracking for intraoperative OCT guided anterior segment ophthalmic surgical maneuvers," *Biomedical Optics Express*, vol. 6, no. 8, p. 3014, Aug. 2015, doi: 10.1364/boe.6.003014.

[282] S. Voros, J. A. Long, and P. Cinquin, “Automatic detection of instruments in laparoscopic images: A first step towards high-level command of robotic endoscopic holders,” in *International Journal of Robotics Research*, Nov. 2007, vol. 26, no. 11–12, pp. 1173–1190. doi: 10.1177/0278364907083395.

[283] S. Speidel *et al.*, “Automatic classification of minimally invasive instruments based on endoscopic image sequences,” in *Medical Imaging 2009: Visualization, Image-Guided Procedures, and Modeling*, Feb. 2009, vol. 7261, no. 13, p. 72610A. doi: 10.1117/12.811112.

[284] Y. M. Baek *et al.*, “Full state visual forceps tracking under a microscope using projective contour models,” in *Proceedings - IEEE International Conference on Robotics and Automation*, 2012, pp. 2919–2925. doi: 10.1109/ICRA.2012.6224848.

[285] R. Sznitman, K. Ali, R. Richa, R. H. Taylor, G. D. Hager, and P. Fua, “Data-driven visual tracking in retinal microsurgery,” in *Medical Image Computing and Computer-Assisted Intervention – MICCAI 2012*, 2012, vol. 7511 LNCS, pp. 568–575. doi: 10.1007/978-3-642-33418-4_70.

[286] J. Ryu, J. Choi, and H. C. Kim, “Endoscopic Vision-Based Tracking of Multiple Surgical Instruments During Robot-Assisted Surgery,” *Artificial Organs*, vol. 37, no. 1, pp. 107–112, Jan. 2013, doi: 10.1111/j.1525-1594.2012.01543.x.

[287] M. T. El-Haddad, J. D. Malone, N. T. Hoang, and Y. K. Tao, “Deep-learning based automated instrument tracking and adaptive-sampling of intraoperative OCT for video-rate volumetric imaging of ophthalmic surgical maneuvers,” in *https://doi.org/10.1117/12.2511827*, Feb. 2019, vol. 10867, p. 57. doi: 10.1117/12.2511827.

[288] M. T. El-Haddad, I. Bozic, and Y. K. Tao, “Spectrally encoded coherence tomography and reflectometry: Simultaneous en face and cross-sectional imaging at 2 gigapixels per second,” *Journal of Biophotonics*, vol. 11, no. 4, p. e201700268, Apr. 2018, doi: 10.1002/jbio.201700268.

[289] A. Bochkovskiy, C. Y. Wang, and H. Y. M. Liao, “YOLOv4: Optimal Speed and Accuracy of Object Detection,” *arXiv*. arXiv, Apr. 22, 2020. Accessed: May 07, 2021. [Online]. Available: http://arxiv.org/abs/2004.10934

[290] Z. Zheng, P. Wang, W. Liu, J. Li, R. Ye, and D. Ren, “Distance-IoU loss: Faster and better learning for bounding box regression,” in *AAAI 2020 - 34th AAAI Conference on Artificial Intelligence*, Nov. 2020, pp. 12993–13000. doi: 10.1609/aaai.v34i07.6999.

[291] B. Gonenc, P. Gehlbach, J. Handa, R. H. Taylor, and I. Iordachita, “Motorized force-sensing micro-forceps with tremor cancelling and controlled micro-vibrations for easier membrane peeling,” in *Proceedings of the IEEE RAS and EMBS International Conference on Biomedical Robotics and Biomechatronics*, Sep. 2014, pp. 244–251. doi: 10.1109/biorob.2014.6913784.

[292] B. Gonenc, R. H. Taylor, I. Iordachita, P. Gehlbach, and J. Handa, “Force-sensing microneedle for assisted retinal vein cannulation,” in *Proceedings of IEEE Sensors*, Dec. 2014, vol. 2014-Decem, no. December, pp. 698–701. doi: 10.1109/ICSENS.2014.6985095.

[293] D. Borroni *et al.*, “The Influence of Speed During Stripping in Descemet Membrane Endothelial Keratoplasty Tissue Preparation,” *Cornea*, vol. 39, no. 9, pp. 1086–1090, Sep. 2020, doi: 10.1097/ICO.0000000000002338.

[294] A. Fedorov *et al.*, “3D Slicer as an image computing platform for the Quantitative Imaging Network,” *Magnetic Resonance Imaging*, vol. 30, no. 9, pp. 1323–1341, Nov. 2012, doi: 10.1016/j.mri.2012.05.001.

[295] S. J. Pan and Q. Yang, “A survey on transfer learning,” *IEEE Transactions on Knowledge and Data Engineering*, vol. 22, no. 10. pp. 1345–1359, 2010. doi: 10.1109/TKDE.2009.191.

[296] H. C. Shin *et al.*, “Deep Convolutional Neural Networks for Computer-Aided Detection: CNN Architectures, Dataset Characteristics and Transfer Learning,” *IEEE Transactions on Medical Imaging*, vol. 35, no. 5, pp. 1285–1298, May 2016, doi: 10.1109/TMI.2016.2528162.

[297] J. D. Li *et al.*, “Image-guided feedback for ophthalmic microsurgery using multimodal intraoperative swept-source spectrally encoded scanning laser ophthalmoscopy and optical coherence tomography,” in *Optical Coherence Tomography and Coherence Domain Optical Methods in Biomedicine XXI*, Feb. 2017, vol. 10053, p. 100530I. doi: 10.1117/12.2254847.

[298] M. J. Ringel, E. M. Tang, D. Hu, I. Oguz, and Y. K. Tao, “Intraoperative spectrally encoded

coherence tomography and reflectometry (iSECTR) for ophthalmic surgical guidance," in *Optical Coherence Tomography and Coherence Domain Optical Methods in Biomedicine XXV*, Mar. 2021, vol. 11630, p. 116300J. doi: 10.1117/12.2583849.

[299] K. Zhang and J. U. Kang, "Real-time intraoperative 4D full-range FD-OCT based on the dual graphics processing units architecture for microsurgery guidance," *Biomedical Optics Express*, vol. 2, no. 4, p. 764, Apr. 2011, doi: 10.1364/boe.2.000764.

[300] W. Wieser *et al.*, "Multi-Megahertz OCT: High quality 3D imaging at 20 million A-scans and 4.5 GVoxels per second," *Optics Express, Vol. 18, Issue 14, pp. 14685-14704*, vol. 18, no. 14, pp. 14685–14704, Jul. 2010, doi: 10.1364/OE.18.014685.

[301] D. R. Uecker, Y. F. Wang, C. Lee, and Y. Wang, "Laboratory investigation: Automated instrument tracking in robotically assisted laparoscopic surgery," *Computer Aided Surgery*, vol. 1, no. 6, pp. 308–325, 1995, doi: 10.3109/10929089509106338.

[302] P. M. Novotny *et al.*, "GPU based real-time instrument tracking with three-dimensional ultrasound," *Medical Image Analysis*, vol. 11, no. 5, pp. 458–464, Oct. 2007, doi: 10.1016/J.MEDIA.2007.06.009.

[303] Y. Li, C. Chen, X. Huang, and J. Huang, "Instrument Tracking via Online Learning in Retinal Microsurgery," *Lecture Notes in Computer Science (including subseries Lecture Notes in Artificial Intelligence and Lecture Notes in Bioinformatics)*, vol. 8673 LNCS, no. PART 1, pp. 464–471, 2014, doi: 10.1007/978-3-319-10404-1_58.

[304] S. J. Mckenna, H. Nait Charif, and T. Frank, "Towards Video Understanding of Laparoscopic Surgery: Instrument Tracking".

[305] J. B. West and C. R. Maurer, "Designing optically tracked instruments for image-guided surgery," *IEEE Transactions on Medical Imaging*, vol. 23, no. 5, pp. 533–545, May 2004, doi: 10.1109/TMI.2004.825614.

[306] I. Oropesa *et al.*, "EVA: Laparoscopic instrument tracking based on endoscopic video analysis for psychomotor skills assessment," *Surgical Endoscopy*, vol. 27, no. 3, pp. 1029–1039, Oct. 2013, doi:

10.1007/S00464-012-2513-Z/FIGURES/6.

[307] A. Roorda, “Adaptive optics for studying visual function: A comprehensive review,” *Journal of Vision*, vol. 11, no. 5, pp. 6–6, May 2011, doi: 10.1167/11.5.6.

[308] M. Wojtkowski, B. Kaluzny, and R. J. Zawadzki, “New directions in ophthalmic optical coherence tomography,” *Optometry and Vision Science*, vol. 89, no. 5, pp. 524–542, May 2012, doi: 10.1097/OPX.0B013E31824EECB2.

[309] G. Klauss, “Ophthalmic Surgical Instruments,” *Topics in Companion Animal Medicine*, vol. 23, no. 1, pp. 3–9, Feb. 2008, doi: 10.1053/J.CTSAP.2007.12.002.

[310] M. Robu, A. Kadkhodamohammadi, I. Luengo, and D. Stoyanov, “Towards real-time multiple surgical tool tracking,” *Computer Methods in Biomechanics and Biomedical Engineering: Imaging and Visualization*, vol. 9, no. 3, pp. 279–285, 2021, doi: 10.1080/21681163.2020.1835553/SUPPL_FILE/TCIV_A_1835553_SM9242.MP4.

[311] J. Ryu, J. Choi, H. Chan Kim, I. Program, and B. Major, “Endoscopic Vision-Based Tracking of Multiple Surgical Instruments During Robot-Assisted Surgery,” *Artificial Organs*, vol. 37, no. 1, pp. 107–112, Jan. 2013, doi: 10.1111/J.1525-1594.2012.01543.X.

[312] C. I. Nwoye, D. Mutter, J. Marescaux, and N. Padoy, “Weakly supervised convolutional LSTM approach for tool tracking in laparoscopic videos,” *International Journal of Computer Assisted Radiology and Surgery*, vol. 14, no. 6, pp. 1059–1067, Jun. 2019, doi: 10.1007/S11548-019-01958-6/FIGURES/3.

[313] L. Li, X. Li, B. Ouyang, S. Ding, S. Yang, and Y. Qu, “Autonomous Multiple Instruments Tracking for Robot-Assisted Laparoscopic Surgery with Visual Tracking Space Vector Method,” *IEEE/ASME Transactions on Mechatronics*, 2021, doi: 10.1109/TMECH.2021.3070553.

[314] M. T. El-Haddad and Y. K. Tao, “Non-contact characterization of compound optical lenses using confocal microscopy and low-coherence interferometry,” *Scientific Reports*, vol. 9, no. 1, p. 22, Dec. 2019, doi: 10.1117/12.2510811.

[315] L. Alzubaidi *et al.*, “Review of deep learning: concepts, CNN architectures, challenges, applications,

future directions," *Journal of Big Data 2021 8:1*, vol. 8, no. 1, pp. 1–74, Mar. 2021, doi: 10.1186/S40537-021-00444-8.

[316] Y. Wang, Q. Sun, G. Sun, L. Gu, and Z. Liu, "Object detection of surgical instruments based on Yolov4," *2021 6th IEEE International Conference on Advanced Robotics and Mechatronics, ICARM 2021*, pp. 578–581, Jul. 2021, doi: 10.1109/ICARM52023.2021.9536075.

[317] N. Kirthika and B. Sargunam, "YOLOv4 for multi-class artefact detection in endoscopic images," *2021 3rd International Conference on Signal Processing and Communication, ICPSC 2021*, pp. 73–77, May 2021, doi: 10.1109/ICSPC51351.2021.9451761.

[318] L. Howell, V. Anagnostidis, and F. Gielen, "Multi-Object Detector YOLOv4-Tiny Enables High-Throughput Combinatorial and Spatially-Resolved Sorting of Cells in Microdroplets," *Advanced Materials Technologies*, p. 2101053, 2021, doi: 10.1002/ADMT.202101053.

[319] L. Taylor and G. Nitschke, "Improving Deep Learning with Generic Data Augmentation," *Proceedings of the 2018 IEEE Symposium Series on Computational Intelligence, SSCI 2018*, pp. 1542–1547, Jan. 2019, doi: 10.1109/SSCI.2018.8628742.

[320] C. Shorten and T. M. Khoshgoftaar, "A survey on Image Data Augmentation for Deep Learning," *Journal of Big Data*, vol. 6, no. 1, pp. 1–48, Dec. 2019, doi: 10.1186/S40537-019-0197-0/FIGURES/33.

[321] K. Chatfield, K. Simonyan, A. Vedaldi, and A. Zisserman, "Return of the Devil in the Details: Delving Deep into Convolutional Nets," *BMVC 2014 - Proceedings of the British Machine Vision Conference 2014*, May 2014, doi: 10.48550/arxiv.1405.3531.

[322] J. Deng, W. Dong, R. Socher, L.-J. Li, K. Li, and L. Fei-Fei, "ImageNet: A Large-Scale Hierarchical Image Database", Accessed: Apr. 25, 2022. [Online]. Available: http://www.image-net.org.

[323] A. Skouta, A. Elmoufidi, S. Jai-Andaloussi, and O. Ouchetto, "Semantic Segmentation of Retinal Blood Vessels from Fundus Images by using CNN and the Random Forest Algorithm", doi: 10.5220/0010911800003118.

[324] S. Liu and Z. Liu, "Multi-Channel CNN-based Object Detection for Enhanced Situation

Awareness".

[325] "GitHub - ultralytics/yolov5: YOLOv5 🚀 in PyTorch > ONNX > CoreML > TFLite." https://github.com/ultralytics/yolov5 (accessed Apr. 30, 2022).

[326] Z. Ge, S. Liu, F. Wang, Z. Li, and J. Sun, "YOLOX: Exceeding YOLO Series in 2021," vol. 5, p. 12, Jul. 2021, doi: 10.48550/arxiv.2107.08430.

[327] A. Eitel, J. T. Springenberg, L. Spinello, M. Riedmiller, and W. Burgard, "Multimodal deep learning for robust RGB-D object recognition," *IEEE International Conference on Intelligent Robots and Systems*, vol. 2015-December, pp. 681–687, Dec. 2015, doi: 10.1109/IROS.2015.7353446.

[328] J. Jiang, X. Feng, F. Liu, Y. Xu, and H. Huang, "Multi-Spectral RGB-NIR Image Classification Using Double-Channel CNN," *IEEE Access*, vol. 7, pp. 20607–20613, 2019, doi: 10.1109/ACCESS.2019.2896128.

[329] Y. Wang, X. Wei, H. Shen, L. Ding, and J. Wan, "Robust fusion for RGB-D tracking using CNN features," *Applied Soft Computing*, vol. 92, p. 106302, Jul. 2020, doi: 10.1016/J.ASOC.2020.106302.

[330] C. Eckardt and E. B. Paulo, "Heads-up surgery for vitreoretinal procedures : An Experimental and Clinical Study," *Retina*, vol. 36, no. 1, pp. 137–147, 2016, doi: 10.1097/IAE.0000000000000689.

[331] H. Yamashita and E. Kobayashi, "Mechanism and design of a novel 8K ultra-high-definition video microscope for microsurgery," *Heliyon*, vol. 7, no. 2, p. e06244, Feb. 2021, doi: 10.1016/J.HELIYON.2021.E06244.

[332] J. P. Ehlers, S. K. Srivastava, D. Feiler, A. I. Noonan, A. M. Rollins, and Y. K. Tao, "Integrative Advances for OCT-Guided Ophthalmic Surgery and Intraoperative OCT: Microscope Integration, Surgical Instrumentation, and Heads-Up Display Surgeon Feedback," *PLoS ONE*, vol. 9, no. 8, p. e105224, Aug. 2014, doi: 10.1371/journal.pone.0105224.

[333] M. Zhao *et al.*, "Novel microscope-integrated stereoscopic heads-up display for intrasurgical optical coherence tomography," *Biomedical Optics Express, Vol. 7, Issue 5, pp. 1711-1726*, vol. 7, no. 5,

pp. 1711–1726, May 2016, doi: 10.1364/BOE.7.001711.

[334] H. bin Helayel, S. Al-Mazidi, and A. Alakeely, “Can the Three-Dimensional Heads-Up Display Improve Ergonomics, Surgical Performance, and Ophthalmology Training Compared to Conventional Microscopy?,” *Clinical Ophthalmology (Auckland, N.Z.)*, vol. 15, p. 679, 2021, doi: 10.2147/OPTH.S290396.

[335] M. Draelos, B. Keller, C. Viehland, O. M. Carrasco-Zevallos, A. Kuo, and J. Izatt, “Real-time visualization and interaction with static and live optical coherence tomography volumes in immersive virtual reality,” *Biomedical Optics Express*, vol. 9, no. 6, p. 2825, Jun. 2018, doi: 10.1364/BOE.9.002825.

[336] L. Shen *et al.*, “Oculus Rift® as a head tracking, stereoscopic head mounted display for intra-operative OCT in ophthalmic surgery,” *iovs.arvojournals.org*, vol. 57, no. 12, pp. 1701–1701, 2016, Accessed: Apr. 30, 2022. [Online]. Available: https://iovs.arvojournals.org/article.aspx?articleid=2558212

[337] J. D. Li *et al.*, “Image-guided feedback for ophthalmic microsurgery using multimodal intraoperative swept-source spectrally encoded scanning laser ophthalmoscopy and optical coherence tomography,” *https://doi.org/10.1117/12.2254847*, vol. 10053, pp. 38–43, Feb. 2017, doi: 10.1117/12.2254847.

[338] K. E. Talcott *et al.*, “Comparison of a Three-Dimensional Heads-Up Display Surgical Platform with a Standard Operating Microscope for Macular Surgery,” *Ophthalmology Retina*, vol. 3, no. 3, pp. 244–251, Mar. 2019, doi: 10.1016/J.ORET.2018.10.016.

[339] Z. Zhang, L. Wang, Y. Wei, D. Fang, S. Fan, and S. Zhang, “The Preliminary Experiences with Three-Dimensional Heads-Up Display Viewing System for Vitreoretinal Surgery under Various Status,” *Current Eye Research*, vol. 44, no. 1, pp. 102–109, Jan. 2019, doi: 10.1080/02713683.2018.1526305/SUPPL_FILE/ICEY_A_1526305_SM7482.PDF.

[340] B. Asani *et al.*, “3D Heads-Up Display vs. Standard Operating Microscope Vitrectomy for Rhegmatogenous Retinal Detachment,” *Front Med (Lausanne)*, vol. 7, Dec. 2020, doi:

10.3389/FMED.2020.615515.

[341] E. Korot *et al.*, “Purpose-built, head-mounted 3D display for ophthalmic microsurgery: surgical skill performance and evaluation: a pilot study,” *BMJ Innovations*, vol. 7, no. 2, pp. 463–469, Apr. 2021, doi: 10.1136/BMJINNOV-2020-000507.

[342] K. Nowomiejska *et al.*, “Vitrectomy Combined with Cataract Surgery for Retinal Detachment Using a Three-Dimensional Viewing System,” *Journal of Clinical Medicine 2022, Vol. 11, Page 1788*, vol. 11, no. 7, p. 1788, Mar. 2022, doi: 10.3390/JCM11071788.

[343] M. B. Muijzer *et al.*, “Automatic evaluation of graft orientation during Descemet membrane endothelial keratoplasty using intraoperative OCT,” *Biomedical Optics Express, Vol. 13, Issue 5, pp. 2683-2694*, vol. 13, no. 5, pp. 2683–2694, May 2022, doi: 10.1364/BOE.446519.

[344] D. Xu, W. J. Dupps, S. K. Srivastava, and J. P. Ehlers, “Automated Volumetric Analysis of Interface Fluid in Descemet Stripping Automated Endothelial Keratoplasty Using Intraoperative Optical Coherence Tomography,” *Investigative Ophthalmology & Visual Science*, vol. 55, no. 9, pp. 5610–5615, Sep. 2014, doi: 10.1167/IOVS.14-14346.

[345] K. M. Hallahan, B. Cost, J. M. Goshe, W. J. Dupps, S. K. Srivastava, and J. P. Ehlers, “Intraoperative Interface Fluid Dynamics and Clinical Outcomes for Intraoperative Optical Coherence Tomography–Assisted Descemet Stripping Automated Endothelial Keratoplasty From the PIONEER Study,” *American Journal of Ophthalmology*, vol. 173, pp. 16–22, Jan. 2017, doi: 10.1016/J.AJO.2016.09.028.

[346] J. P. Ehlers, A. Uchida, S. K. Srivastava, and M. Hu, “Predictive Model for Macular Hole Closure Speed: Insights From Intraoperative Optical Coherence Tomography,” *Translational Vision Science & Technology*, vol. 8, no. 1, pp. 18–18, Jan. 2019, doi: 10.1167/TVST.8.1.18.

[347] M. Zhou *et al.*, “Beveled needle position and pose estimation based on optical coherence tomography in ophthalmic microsurgery,” *2017 IEEE International Conference on Robotics and Biomimetics, ROBIO 2017*, vol. 2018-January, pp. 308–313, Mar. 2018, doi: 10.1109/ROBIO.2017.8324435.

[348] M. Zhou *et al.*, “Precision Needle Tip Localization Using Optical Coherence Tomography Images for Subretinal Injection,” *Proceedings - IEEE International Conference on Robotics and Automation*, pp. 4033–4040, Sep. 2018, doi: 10.1109/ICRA.2018.8460745.

[349] M. Zhou *et al.*, “Needle localization for robot-assisted subretinal injection based on deep learning,” *Proceedings - IEEE International Conference on Robotics and Automation*, vol. 2019-May, pp. 8727–8732, May 2019, doi: 10.1109/ICRA.2019.8793756.

[350] Z. Song *et al.*, “Lightweight Learning-Based Automatic Segmentation of Subretinal Blebs on Microscope-Integrated Optical Coherence Tomography Images,” *American Journal of Ophthalmology*, vol. 221, pp. 154–168, Jan. 2021, doi: 10.1016/J.AJO.2020.07.020.

[351] M. Pekala, N. Joshi, T. Y. A. Liu, N. M. Bressler, D. C. DeBuc, and P. Burlina, “Deep learning based retinal OCT segmentation,” *Computers in Biology and Medicine*, vol. 114, p. 103445, Nov. 2019, doi: 10.1016/J.COMPBIOMED.2019.103445.

[352] J. Kugelman *et al.*, “Automatic choroidal segmentation in OCT images using supervised deep learning methods,” *Scientific Reports 2019 9:1*, vol. 9, no. 1, pp. 1–13, Sep. 2019, doi: 10.1038/s41598-019-49816-4.

[353] D. Lu *et al.*, “Deep-learning based multiclass retinal fluid segmentation and detection in optical coherence tomography images using a fully convolutional neural network,” *Medical Image Analysis*, vol. 54, pp. 100–110, May 2019, doi: 10.1016/J.MEDIA.2019.02.011.

[354] N. Mehta *et al.*, “Model-to-Data Approach for Deep Learning in Optical Coherence Tomography Intraretinal Fluid Segmentation,” *JAMA Ophthalmology*, vol. 138, no. 10, pp. 1017–1024, Oct. 2020, doi: 10.1001/JAMAOPHTHALMOL.2020.2769.

[355] J. Weiss, U. Eck, M. A. Nasseri, M. Maier, A. Eslami, and N. Navab, “Layer-Aware iOCT Volume Rendering for Retinal Surgery,” *Eurographics Workshop on Visual Computing for Biology and Medicine*, 2019, doi: 10.2312/vcbm.20191239.

[356] M. I. Seider *et al.*, “Real-Time Volumetric Imaging of Vitreoretinal Surgery with a Prototype Microscope-Integrated Swept-Source OCT Device,” *Ophthalmology Retina*, vol. 2, no. 5, pp. 401–

410, May 2018, doi: 10.1016/J.ORET.2017.08.023.

[357] I. D. Bleicher, M. Jackson-Atogi, C. Viehland, H. Gabr, J. A. Izatt, and C. A. Toth, "Depth-Based, Motion-Stabilized Colorization of Microscope-Integrated Optical Coherence Tomography Volumes for Microscope-Independent Microsurgery," *Translational Vision Science & Technology*, vol. 7, no. 6, pp. 1–1, Nov. 2018, doi: 10.1167/TVST.7.6.1.

[358] R. M. Lerner, K. J. Parker, J. Holen, R. Gramiak, and R. C. Waag, "Sono-Elasticity: Medical Elasticity Images Derived from Ultrasound Signals in Mechanically Vibrated Targets," Springer, Boston, MA, 1988, pp. 317–327. doi: 10.1007/978-1-4613-0725-9_31.

[359] B. F. Kennedy, K. M. Kennedy, and D. D. Sampson, "A review of optical coherence elastography: Fundamentals, techniques and prospects," *IEEE Journal on Selected Topics in Quantum Electronics*, vol. 20, no. 2. Mar. 2014. doi: 10.1109/JSTQE.2013.2291445.

[360] R. K. Chhetri, K. A. Kozek, A. C. Johnston-Peck, J. B. Tracy, and A. L. Oldenburg, "Imaging three-dimensional rotational diffusion of plasmon resonant gold nanorods using polarization-sensitive optical coherence tomography," *Physical Review E - Statistical, Nonlinear, and Soft Matter Physics*, vol. 83, no. 4, Apr. 2011, doi: 10.1103/PhysRevE.83.040903.

[361] R. L. Blackmon *et al.*, "Imaging Extracellular Matrix Remodeling in Vitro by Diffusion-Sensitive Optical Coherence Tomography," *Biophysical Journal*, vol. 110, no. 8, pp. 1858–1868, Apr. 2016, doi: 10.1016/j.bpj.2016.03.014.

[362] B. J. Blackburn *et al.*, "Noninvasive assessment of corneal crosslinking with phase-decorrelation optical coherence tomography," *Investigative Ophthalmology and Visual Science*, vol. 60, no. 1, pp. 41–51, Jan. 2019, doi: 10.1167/iovs.18-25535.

[363] J. M. Schmitt, "OCT elastography: imaging microscopic deformation and strain of tissue," *Optics Express*, vol. 3, no. 6, p. 199, Sep. 1998, doi: 10.1364/oe.3.000199.

[364] E. J. Chen, J. Novakofski, W. Kenneth Jenkins, and W. D. O'Brien, "Young's modulus measurements of soft tissues with application to elasticity imaging," *IEEE Transactions on Ultrasonics, Ferroelectrics, and Frequency Control*, vol. 43, no. 1, pp. 191–194, 1996, doi:

10.1109/58.484478.

[365] X. Liang, V. Crecea, and S. A. Boppart, “Dynamic optical coherence elastography: A review,” *Journal of Innovative Optical Health Sciences*, vol. 3, no. 4. NIH Public Access, pp. 221–233, Oct. 2010. doi: 10.1142/S1793545810001180.

[366] A. Ramier *et al.*, “In vivo measurement of shear modulus of the human cornea using optical coherence elastography,” *Scientific Reports*, vol. 10, no. 1, Dec. 2020, doi: 10.1038/s41598-020-74383-4.

[367] M. S. Sridhar, “Anatomy of cornea and ocular surface,” *Indian Journal of Ophthalmology*, vol. 66, no. 2. Medknow Publications, pp. 190–194, Feb. 2018. doi: 10.4103/ijo.IJO_646_17.

[368] C. J. Roberts and W. J. Dupps, “Biomechanics of corneal ectasia and biomechanical treatments,” *Journal of Cataract and Refractive Surgery*, vol. 40, no. 6. Elsevier Inc., pp. 991–998, 2014. doi: 10.1016/j.jcrs.2014.04.013.

[369] C. W. Hong, A. Sinha-Roy, L. Schoenfield, J. T. Mcmahon, and W. J. Dupps, “Collagenase-mediated tissue modeling of corneal ectasia and collagen cross-linking treatments,” *Investigative Ophthalmology and Visual Science*, vol. 53, no. 4, pp. 2321–2327, Apr. 2012, doi: 10.1167/iovs.11-9327.

[370] G. Wollensak, E. Spoerl, and T. Seiler, “Riboflavin/ultraviolet-A-induced collagen crosslinking for the treatment of keratoconus,” *American Journal of Ophthalmology*, vol. 135, no. 5, pp. 620–627, May 2003, doi: 10.1016/S0002-9394(02)02220-1.

[371] Y. Zhou *et al.*, “In vivo evaluation of corneal biomechanical properties by optical coherence elastography at different cross-linking irradiances,” *Journal of Biomedical Optics*, vol. 24, no. 10, p. 1, Oct. 2019, doi: 10.1117/1.jbo.24.10.105001.

[372] M. Singh *et al.*, “Noncontact Elastic Wave Imaging Optical Coherence Elastography for Evaluating Changes in Corneal Elasticity Due to Crosslinking,” *IEEE Journal of Selected Topics in Quantum Electronics*, vol. 22, no. 3, pp. 266–276, May 2016, doi: 10.1109/JSTQE.2015.2510293.

[373] Z. Han *et al.*, “Analysis of the effect of the fluid-structure interface on elastic wave velocity in

cornea-like structures by OCE and FEM," *Laser Physics Letters*, vol. 13, no. 3, p. 035602, Mar. 2016, doi: 10.1088/1612-2011/13/3/035602.

[374] Y. Qu *et al.*, "Quantified elasticity mapping of retinal layers using synchronized acoustic radiation force optical coherence elastography," *Biomedical Optics Express*, vol. 9, no. 9, p. 4054, Sep. 2018, doi: 10.1364/boe.9.004054.

[375] Y. Qu *et al.*, "In vivo elasticity mapping of posterior ocular layers using acoustic radiation force optical coherence elastography," *Investigative Ophthalmology and Visual Science*, vol. 59, no. 1, pp. 455–461, Jan. 2018, doi: 10.1167/iovs.17-22971.

[376] Z. Du *et al.*, "Quantitative confocal optical coherence elastography for evaluating biomechanics of optic nerve head using Lamb wave model," *Neurophotonics*, vol. 6, no. 04, p. 1, Nov. 2019, doi: 10.1117/1.nph.6.4.041112.

[377] M. Singh *et al.*, "Noncontact optical coherence elastography of the posterior porcine sclera *in situ* as a function of IOP," in *Ophthalmic Technologies XXVII*, Feb. 2017, vol. 10045, p. 1004524. doi: 10.1117/12.2253445.

[378] S. P. N. Singh and C. N. Riviere, "Physiological tremor amplitude during retinal microsurgery," *Bioengineering, Proceedings of the Northeast Conference*, pp. 171–172, 2002, doi: 10.1109/NEBC.2002.999520.

[379] T. Bourcier *et al.*, "Robot-assisted simulated cataract surgery," *Journal of Cataract & Refractive Surgery*, vol. 43, no. 4, pp. 552–557, Apr. 2017, doi: 10.1016/J.JCRS.2017.02.020.

[380] J. Chammas *et al.*, "Da Vinci Xi Robot–Assisted Penetrating Keratoplasty," *Translational Vision Science & Technology*, vol. 6, no. 3, pp. 21–21, May 2017, doi: 10.1167/TVST.6.3.21.

[381] D. H. Bourla, J. P. Hubschman, M. Culjat, A. Tsirbas, A. Gupta, and S. D. Schwartz, "Feasibility study of intraocular robotic surgery with the da Vinci surgical system," *Retina*, vol. 28, no. 1, pp. 154–158, Jan. 2008, doi: 10.1097/IAE.0B013E318068DE46.

[382] M. Forslund Jacobsen, L. Konge, M. Alberti, M. la Cour, Y. S. Park, and A. S. S. Thomsen, "ROBOT-ASSISTED VITREORETINAL SURGERY IMPROVES SURGICAL ACCURACY

COMPARED WITH MANUAL SURGERY: A Randomized Trial in a Simulated Setting," *Retina*, vol. 40, no. 11, p. 2091, Nov. 2020, doi: 10.1097/IAE.0000000000002720.

[383] B. Keller *et al.*, "Optical Coherence Tomography-Guided Robotic Ophthalmic Microsurgery via Reinforcement Learning from Demonstration," *IEEE Transactions on Robotics*, vol. 36, no. 4, pp. 1207–1218, Aug. 2020, doi: 10.1109/TRO.2020.2980158.

[384] I. Park, H. K. Kim, W. K. Chung, and K. Kim, "Deep Learning Based Real-Time OCT Image Segmentation and Correction for Robotic Needle Insertion Systems," *IEEE Robotics and Automation Letters*, vol. 5, no. 3, pp. 4517–4524, Jul. 2020, doi: 10.1109/LRA.2020.3001474.

[385] M. Zhou *et al.*, "Towards Robotic Eye Surgery: Marker-Free, Online Hand-Eye Calibration Using Optical Coherence Tomography Images," *IEEE Robotics and Automation Letters*, vol. 3, no. 4, pp. 3944–3951, Oct. 2018, doi: 10.1109/LRA.2018.2858744.

[386] B. Gonenc, A. Chamani, J. Handa, P. Gehlbach, R. H. Taylor, and I. Iordachita, "3-DOF Force-Sensing Motorized Micro-Forceps for Robot-Assisted Vitreoretinal Surgery," *IEEE Sens J*, vol. 17, no. 11, p. 3526, Jun. 2017, doi: 10.1109/JSEN.2017.2694965.

[387] B. Gonenc, J. Chae, P. Gehlbach, R. H. Taylor, and I. Iordachita, "Towards Robot-Assisted Retinal Vein Cannulation: A Motorized Force-Sensing Microneedle Integrated with a Handheld Micromanipulator †," *Sensors 2017, Vol. 17, Page 2195*, vol. 17, no. 10, p. 2195, Sep. 2017, doi: 10.3390/S17102195.

[388] M. J. Gerber, M. Pettenkofer, and J. P. Hubschman, "Advanced robotic surgical systems in ophthalmology," *Eye 2020 34:9*, vol. 34, no. 9, pp. 1554–1562, Mar. 2020, doi: 10.1038/s41433-020-0837-9.

[389] N. Gessert *et al.*, "Spatio-temporal deep learning models for tip force estimation during needle insertion," *International Journal of Computer Assisted Radiology and Surgery*, vol. 14, no. 9, pp. 1485–1493, Sep. 2019, doi: 10.1007/S11548-019-02006-Z/FIGURES/6.

[390] M. Gromniak, N. Gessert, T. Saathoff, and A. Schlaefer, "Needle tip force estimation by deep learning from raw spectral OCT data," *International Journal of Computer Assisted Radiology and*

Surgery, vol. 15, no. 10, pp. 1699–1702, Oct. 2020, doi: 10.1007/S11548-020-02224-W/FIGURES/3.

[391] N. Gessert, J. Beringhoff, C. Otte, and A. Schlaefer, "Force estimation from OCT volumes using 3D CNNs," *International Journal of Computer Assisted Radiology and Surgery*, vol. 13, no. 7, pp. 1073–1082, Jul. 2018, doi: 10.1007/S11548-018-1777-8/TABLES/1.